

## ABSTRACT

Title of dissertation:      PARAMETRIC LIMITATIONS ON DISCHARGE  
                                  PERFORMANCE IN THE MARYLAND  
                                  CENTRIFUGAL EXPERIMENT

Robert Lunsford, Doctor of Philosophy, 2007

Dissertation directed by:  Professor Richard F Ellis  
                                  Department of Physics

Inherent in any experiment is a set of bounding limitations. In the Maryland Centrifugal eXperiment (MCX) these limitations are manifest as restrictions upon discharge performance as defined by program goals. We therefore examine the multidimensional parameter space in which MCX operates so as to ascertain the performance boundaries along each of the variable axes. In as much as is possible, the variables are expressly decoupled in order to determine their unique effect upon discharge performance. This study has led to the following conclusions. First, the nascent cause of transitions within the MCX discharge from a higher voltage mode (H-mode) into a lower voltage mode (O-mode) appears to be consistent with the formation of a secondary breakdown within the vacuum vessel. These transitions have been shown to be mitigated by auspicious choice of insulator position and geometry. Second, the effect of variations to the radial extent of the discharge has been studied and a set of parametric dependencies determined. These show the MCX discharge to be diffusive in nature, and highly dependant upon radial extent.

Thus leading to the conclusion that a minor increase to the midplane vessel extent should result in substantial performance enhancement. Finally, a global limitation to the MCX discharge has been discovered. It is manifest as an abrupt maximum attainable voltage across the plasma. This has been interpreted as a velocity limitation due to the direct relationship between plasma voltage and rotation velocity ( $v_\phi = V_p/aB$ ). An examination of a discharge struck in a background helium environment, as opposed to the standard hydrogen backfill, has shown that this limit is consistent with Alfvén's theory of a critical ionization velocity ( $v_\phi = \sqrt{2e\Phi_i/m_i}$ ). While this limitation has been observed on the historic predecessors to MCX, there have also been cases where supercritical velocities have been achieved. Suggestions for facilitating access to this regime as well as projections for an enhanced iteration of the MCX device are listed.

PARAMETRIC LIMITATIONS ON DISCHARGE  
PERFORMANCE IN THE  
MARYLAND CENTRIFUGAL EXPERIMENT

by

Robert Lunsford

Dissertation submitted to the Faculty of the Graduate School of the  
University of Maryland, College Park in partial fulfillment  
of the requirements for the degree of  
Doctor of Philosophy  
2007

Advisory Committee:

Professor Richard Ellis, Chair  
Professor Adil Hassam  
Professor Alan W. Desilva  
Associate Professor William Dorland  
Professor Wendell T. Hill

© Copyright by  
Robert Lunsford  
2007

# Table of Contents

List of Tables	v
List of Figures	vi
1 Introduction	1
1.1 Summary of Underlying Theory . . . . .	3
1.2 Summary of Results . . . . .	8
2 Mechanical Setup	13
2.1 Introduction . . . . .	13
2.2 Discharge Circuit and Constituent Parts . . . . .	14
2.2.1 Bank Setup . . . . .	15
2.2.2 Ignitrons . . . . .	15
2.2.3 Series Resistance . . . . .	16
2.3 Plasma Crowbar and Current Reversal . . . . .	17
2.3.1 Calculation of the momentum confinement time and interpretation of the stored charge . . . . .	19
2.3.2 Necessity of a modified crowbar . . . . .	20
2.3.3 Modified Crowbar Calculation and Errors . . . . .	22
2.4 Controlled Plasma Load . . . . .	25
2.4.1 Supporting Theory . . . . .	27
2.4.2 Practical Implementation and Plasma Comparison . . . . .	29
2.5 The Freewheeling Crowbar . . . . .	29
2.5.1 Test Setup . . . . .	32
2.5.2 Freewheeling Experiments . . . . .	37
2.5.3 Freewheeling Limitations . . . . .	37
2.6 The MCX Diagnostic Suite . . . . .	38
2.6.1 Voltage Measurements and Calibrations . . . . .	40
2.6.2 Current Measurements and Calibrations . . . . .	41
2.6.3 Photodiode Diagnostic . . . . .	44
2.6.4 Spectroscopic measurement of rotation velocity . . . . .	45
2.6.5 Magnetic Probes . . . . .	47
3 The MCX Discharge	49
3.1 Introduction . . . . .	50
3.2 Voltage Holdoff and Initial Plasma Breakdown . . . . .	51
3.2.1 Ionization Model . . . . .	51
3.3 H Type Modes . . . . .	54
3.3.1 The High Rotation mode . . . . .	54
3.3.2 The High Voltage Mode . . . . .	56
3.3.3 Modal Causality . . . . .	57
3.4 Discharge Transitions . . . . .	62
3.4.1 Prevailing cause of MCX discharge transitions . . . . .	62

3.4.2	Photodiode recordings of transition induced optical bursting . . . . .	63
3.4.3	Circuit Modeling of Discharge Transitions and Consequences . . . . .	63
3.4.4	Additional Supporting Evidence . . . . .	68
3.4.5	Transition induced discharge limitations . . . . .	73
3.5	Low Voltage Mode (O-mode) . . . . .	73
3.6	Alternate Discharge Modes . . . . .	74
3.6.1	Low Density Plasma Breakdown . . . . .	75
3.6.2	High Current Plasma Breakdown . . . . .	78
3.7	Rubric for Classification of Discharge Performance . . . . .	78
4	Variational Discharge Parameters and their performance effect . . . . .	82
4.1	Insulators . . . . .	82
4.1.1	Disk Position and Results of position scan . . . . .	85
4.1.2	Ceramic Plasma Facing Components (MACOR) . . . . .	89
4.1.3	Polymer based Plasma Facing Components (HDPE) . . . . .	92
4.1.4	MYLAR end wrap . . . . .	94
4.2	Effects of variational Fill Pressure . . . . .	95
4.2.1	Discharge Performance . . . . .	95
4.2.2	Effects of insulator composition on the ability to operate at reduced fill pressures . . . . .	102
4.2.3	Static Pressure Fill Tests . . . . .	102
4.2.4	Effect of fill pressure on discharge diagnostics and parameter range . . . . .	106
4.3	Magnetic Field Variance . . . . .	107
4.3.1	Field Strength . . . . .	108
4.3.2	Mirror Ratio . . . . .	109
4.4	Input Power Circuit Variables . . . . .	111
4.4.1	Capacitor Bank Size . . . . .	112
4.4.2	Capacitor Bank Voltage . . . . .	113
4.4.3	Series Resistance . . . . .	118
4.4.4	Coupling between bank voltage and series resistance . . . . .	120
4.5	Forced limitations on radial discharge extent . . . . .	122
4.5.1	Aluminum Limiter Schematic . . . . .	122
4.5.2	Results of radial scan . . . . .	125
4.6	Parsing the Multi Dimensional Space for Peak Performance . . . . .	133
5	The Critical Ionization Velocity Effect . . . . .	137
5.1	Manifestation of the CIV . . . . .	139
5.1.1	Location of the discharge limiting surface . . . . .	139
5.1.2	CIV limitations on Discharge Voltage . . . . .	141
5.1.3	CIV model for mirror ratio scalings . . . . .	143
5.2	Causes of the CIV in MCX . . . . .	145
5.2.1	Physical underlying mechanism for the CIV effect . . . . .	145
5.2.2	Plasma/Neutral interactions during ionization phase . . . . .	148
5.2.3	Boundary interactions at the insulating surfaces . . . . .	149

5.3	CIV check with alternate fill gas . . . . .	151
5.4	Supercritical Velocities . . . . .	153
6	Future MCX directions . . . . .	156
6.1	Possible solutions to the present MCX limitations . . . . .	156
6.1.1	Consequences of the CIV on machine design . . . . .	157
6.1.2	Construction of a no cost plasma injection gun . . . . .	159
6.2	Scalings of MCX given present limitations . . . . .	161
6.3	Possible future physical limitations . . . . .	163
7	Conclusion . . . . .	167
A	Centrifugally Confined Plasmas . . . . .	169
A.1	Definition of Rotation Velocity . . . . .	169
A.2	Mirror Geometry . . . . .	170
A.2.1	Rotational closing of the loss cone . . . . .	172
A.3	Magnetohydrodynamics (MHD) . . . . .	175
A.3.1	Applicability of Magnetohydrodynamics . . . . .	175
A.3.2	Centrifugal Confinement . . . . .	177
A.3.3	Plasma Resistance Model . . . . .	180
A.3.4	Neutral Penetration . . . . .	183
A.4	Energy Confinement . . . . .	184
A.4.1	Energy Loss Mechanisms . . . . .	185
A.4.2	Field Parallel Electron Transport . . . . .	187
A.5	Presence and importance of Velocity Shear . . . . .	189
A.5.1	Velocity Shear suppression of Magnetohydrodynamic instabilities . . . . .	190
A.5.2	Multi chord spectroscopic confirmation of velocity shear . . . . .	192
B	Experimental Vessel and main power supplies . . . . .	194
B.1	Vessel Dimensions and Description . . . . .	194
B.2	Capacitor charging power supply . . . . .	196
B.3	The Vacuum Magnetic Field . . . . .	198
B.3.1	Midplane and Mirror Coil Description . . . . .	199
B.3.2	Implementation of an additional midplane resistor . . . . .	200
B.3.3	Magnetic Field Tables for varied Midplane Resistors . . . . .	202
B.3.4	Representative Magnetic Field Plots and Discussion of limiting flux surfaces . . . . .	205
B.4	Chamber fill gas and pressure . . . . .	207
C	Alternate calculation of the modified crowbar correction factor . . . . .	208
	Bibliography . . . . .	211

## List of Tables

1.1	The variational parameter ranges available to MCX . . . . .	9
4.1	Average values for critical plasma performance parameters observed during a scan of insulator position . . . . .	87
4.2	Comparison of grooved and flat MACOR cuffs . . . . .	91
4.3	Critical discharge parameters at altered fill pressures . . . . .	99
4.4	Empirical fit to the variation of discharge resistance with radial extent.	129
6.1	Projected performance parameters of MCX-II . . . . .	162
B.1	Completely Eratron driven magnetic field with an additional resistance of $0 \Omega$ . . . . .	203
B.2	Completely Eratron driven magnetic field with an additional resistance of $0.25 \Omega$ . . . . .	203
B.3	Completely Eratron driven magnetic field with an additional resistance of $0.5 \Omega$ . . . . .	204
B.4	Completely Eratron driven magnetic field with an additional resistance of $0.75 \Omega$ . . . . .	204
B.5	Completely Eratron driven magnetic field with an additional resistance of $1 \Omega$ . . . . .	205

## List of Figures

1.1	Geometry of MCX . . . . .	2
2.1	Multi-stage 20 kV capacitor bank which powers the MCX discharge .	13
2.2	The load current through the MCX discharge . . . . .	18
2.3	A 0-D model of the MCX discharge . . . . .	26
2.4	Comparison of recorded current reversals . . . . .	30
2.5	Typical freewheeling current trace for a plasma load . . . . .	33
2.6	Comparison of decay timescales for standard and freewheeling control load shots . . . . .	34
2.7	Logarithmic decay of various control loads . . . . .	36
2.8	Tau comparison for the benchmark H-mode freewheeling crowbar test	39
2.9	Calibration of the plasma current diagnostic with a known control load	43
2.10	MCX spectroscopic arrangement . . . . .	46
2.11	The MS magnetic probes in MCX . . . . .	48
3.1	Plasma Voltage and Current traces for a standard MCX discharge . .	49
3.2	Voltage and photodiode traces for a discharge in which there is no transition event . . . . .	64
3.3	MCX discharge with a transition at the Near End(NE) . . . . .	65
3.4	MCX discharge with a transition at the High Voltage(HV)end . . . .	66
3.5	Unfiltered photodiode recording of the MCX discharge at the High Voltage(HV)end . . . . .	67
3.6	MCX circuit model, modified to include transitions . . . . .	69
3.7	Results of the P-SPICE transitional discharge simulation . . . . .	70
3.8	Comparison of the spectral emission recorded at the insulator face for transitional and non-transitional discharges . . . . .	72

3.9	Location of the minimum input power necessary for operation of the MCX system . . . . .	76
3.10	Comparison of nominal and low density discharge modes . . . . .	77
4.1	Schematic of the MCX insulating assembly . . . . .	84
4.2	Placement of the insulating assembly during the position scan . . . . .	86
4.3	Momentum confinement time as a function of insulator position . . . . .	88
4.4	Qualitative comparison of discharge behaviors . . . . .	97
4.5	Density dependence on fill pressure . . . . .	100
4.6	Increased neutral signal evident at elevated fill pressures . . . . .	101
4.7	Results of MCX conditioning run . . . . .	105
4.8	Dependence of plasma voltage on midplane magnetic field for a fixed mirror ratio . . . . .	110
4.9	Comparison of plasma voltage traces with alternate source bank sizes . . . . .	114
4.10	Effect of increased initial capacitor bank voltage upon maximum discharge voltage . . . . .	115
4.11	Effect of increased bank voltage on discharge resistance . . . . .	117
4.12	Functional dependence of the initial plasma resistance upon external series resistance . . . . .	119
4.13	Operational parameter space for the MCX discharge . . . . .	120
4.14	Diagram of the discharge limiting clamp . . . . .	123
4.15	Magnetic field map for radially limited discharges . . . . .	124
4.16	Radial scaling of maximum discharge voltage . . . . .	127
4.17	Rotational velocity for varying discharge extent and initial bank voltage . . . . .	128
4.18	Discharge resistance with varying radial extent . . . . .	130
4.19	Scaling of momentum confinement time with radial discharge extent . . . . .	132
4.20	Radial dependence of momentum confinement time subdivided by initial bank voltage . . . . .	134

5.1	Evidence of a velocity limitation on MCX . . . . .	138
5.2	Geometric scaling factor for a mirror ratio of 7.2 . . . . .	140
5.3	Velocity limited magnetic field scaling for mirror ratio 4.4. . . . .	142
5.4	Effect of mirror ratio upon magnetic field scaling . . . . .	144
5.5	Predicted maximum plasma voltages for a helium discharge based upon velocity limited hydrogen data . . . . .	152
6.1	MCX with modified terminal field . . . . .	158
6.2	Assembly drawing for the voltage feedthrough . . . . .	160
6.3	Scaling of the Alfvén Mach number with midplane magnetic field . .	166
A.1	Schematic depiction of a magnetic mirror. . . . .	172
A.2	Resultant closing of the mirror loss cone. . . . .	174
A.3	Definition of coordinate axis. . . . .	178
B.1	The MCX Experimental Vessel and attendant electromagnetic coils .	195
B.2	Present circuit configuration of the magnetic coils . . . . .	200
B.3	Representative magnetic field line plot . . . . .	206
C.1	Simplified diagram of the MCX discharge circuit. . . . .	208

# Chapter 1

## Introduction

The Maryland Centrifugal eXperiment (MCX) is a confinement device designed to create a stable, long lived plasma volume for fusion research purposes [21, 29]. The centrifugal forces created by the supersonic rotation of a strongly magnetized discharge in conjunction with the geometric field shaping of a standard magnetic mirror should be sufficient to offset the strong axial pressure gradient necessary for containment of the discharge.

The central solenoidal portion of the magnetic field in a cylindrical geometry is augmented by axisymmetric mirror end fields. The plasma volume is induced into rotation by application of a radial electrical field supplied through a central electrode, as is shown in Fig. 1.1. Upon reaching thermally supersonic speeds, the centrifugal forces created by the bulk rotation will direct the plasma towards the center of the confinement region, effectively closing the loss cone long associated with nonrotational mirror configurations. In addition, stratification of the plasma due to radial variations within the electric field will create a velocity shearing effect between the plasma layers leading to the quenching of Magnetohydrodynamic macroinstabilities [28, 33] as well as the creation of substantial viscous heating. If centrifugal confinement is successful, this geometry can then be scaled into an

energetically favorable fusion reactor.

Having already demonstrated that MCX creates steady supersonically rotating plasmas [20], we now attempt to determine the limitations present within the system. The enumeration and classification of these limitations and their resultant effect upon the ability to scale the MCX discharge into future iterations is the subject addressed herein.

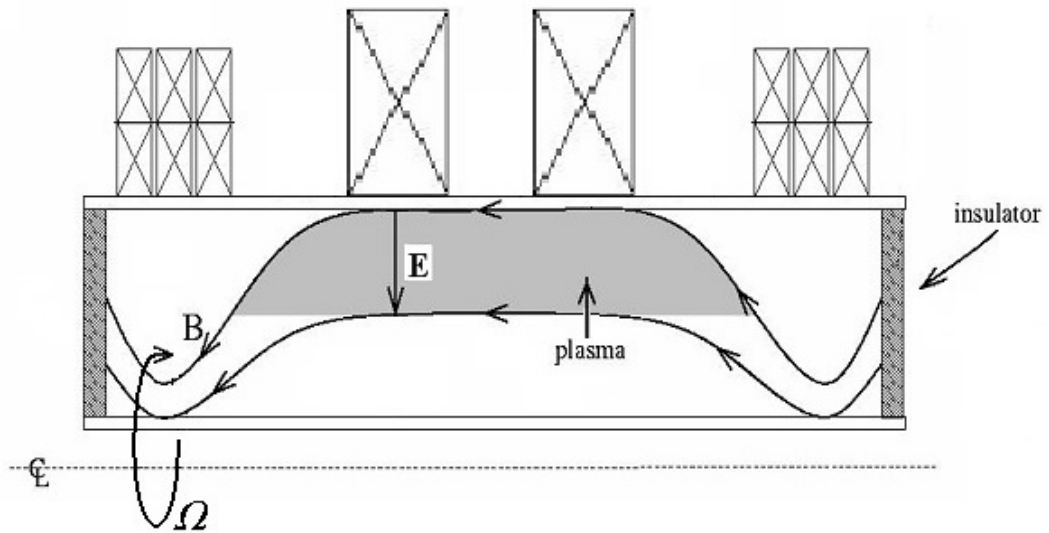


Figure 1.1: Geometry of MCX. A pair of magnetic coils creates a solenoidal field ranging in strength from 1 - 4 kGauss while high field coils at the longitudinal extents are responsible for the mirror field configuration. The transverse electric field is provided by a capacitively coupled stainless steel core at the radial center of the vacuum vessel. The assembly shown in the figure is reflected across the dotted centerline resulting in a cylindrical configuration.

## 1.1 Summary of Underlying Theory

(This section is intended as the briefest of introductions into centrifugal confinement theory. Those wishing a more thorough explanation of the theoretical underpinnings of MCX are referred to appendix A.)

The application of a radial electric field to an axisymmetric poloidal magnetic field will induce an ionized discharge into rotation through the standard  $E \times B$  drift and result in an toroidal velocity

$$v_\phi = \frac{E \times B}{B^2} \quad (1.1)$$

The Maryland Centrifugal eXperiment utilizes the centrifugal forces created by this rotating mirror field discharge to create an effective gravitational confinement region at the center of the open field line system. The governing Hamiltonian for the system is therefore [40]

$$H = \frac{1}{2}M_i v_\parallel^2 + \mu B - \frac{1}{2}MR^2\Omega^2 \quad (1.2)$$

where  $\Omega$  is the angular velocity of the particle about the centerline, and  $\mu = mv_\perp^2/2B$  is the standard invariant magnetic moment of the ion. For  $\Omega R \geq v_{\text{th}}$  the mirror potential can be neglected and the effective gravitational force on the central region becomes

$$g_{\text{centrifugal}} \propto R\Omega^2 \quad (1.3)$$

As MCX produces a highly collisional magnetized discharge with a nominal ion larmor radius much smaller than the relevant scale sizes of the system, we can utilize

the magnetohydrodynamic formalism to describe the resultant behavior. The single fluid MHD equation governing MCX [37] is

$$nM \left( \frac{\partial \mathbf{u}}{\partial t} + \mathbf{u} \cdot \nabla \mathbf{u} \right) = -\nabla p + \mathbf{j} \times \mathbf{B} - nMv_{\text{in}} \mathbf{u} \quad (1.4)$$

Where  $\mathbf{u}$  is the fluid velocity,  $p$  is the pressure,  $j$  is a volume current and  $v_{\text{in}}$  is the ion-neutral collision frequency.

Examining the equilibrium ( $\frac{\partial \mathbf{u}}{\partial t} = 0$ ) state of the system in field normalized cylindrical coordinates with a set of axes parallel to the field ( $\mathbf{B}$ ), radially perpendicular to the field ( $\hat{\psi}$ ), and a poloidal rotational direction ( $\hat{\phi}$ ) we reach the following field-perpendicular conclusions. First, the radial current balances the viscous losses of the discharge.

$$(\mathbf{j} \times \mathbf{B})_{\phi} = j_{\psi} B = nMv_{\text{in}} u_{\phi} \quad (1.5)$$

Second, the azimuthal current balances the centrifugal force and radial pressure profile.

$$(\mathbf{j} \times \mathbf{B})_{\psi} = j_{\phi} B = \nabla p_{\psi} = nM \mathbf{u} \cdot \nabla \mathbf{u} \quad (1.6)$$

Now examining the field-parallel direction, we find that

$$\mathbf{B} \cdot \nabla p = \mathbf{B} \cdot (nM \mathbf{u} \cdot \nabla \mathbf{u}) \quad (1.7)$$

If we let  $\mathbf{u} = R\Omega \hat{\phi}$  then  $\mathbf{u} \cdot \nabla \mathbf{u} = \nabla (R^2\Omega^2/2)$  so that

$$\mathbf{B} \cdot \nabla p = nMB \cdot \left( \frac{R^2\Omega^2}{2} \right) \quad (1.8)$$

Assuming an isothermal discharge, with the sound speed  $c_s = \sqrt{kT/M}$  the density gradient can be shown to be

$$\frac{\mathbf{B} \cdot \nabla n}{n} = \mathbf{B} \cdot \nabla \left( \frac{R^2 \Omega^2}{2c_s^2} \right) \quad (1.9)$$

Which results in a density given by

$$n(\psi, R) = n_0(\psi) e^{\frac{R^2 \Omega^2}{2c_s^2}} \quad (1.10)$$

Such that the ratio of midplane density over throat density is

$$\frac{n_{\text{Mid}}}{n_{\text{End}}} = \exp \left[ \frac{(R_{\text{Mid}}^2 - R_{\text{End}}^2) \Omega^2}{2c_s^2} \right] \quad (1.11)$$

If we define the sonic Mach number as  $M_s = v_\phi/c_s$  then for our isothermal system, the resultant pressure profile along the isorotational curved magnetic field line is

$$\frac{p_{\text{Mid}}}{p_{\text{End}}} = \exp \left[ \frac{M_s}{2} \left( 1 - \frac{1}{R_A^2} \right) \right] \quad (1.12)$$

Where  $R_A$  is the system aspect ratio. Thus we note that the centrifugal confinement mechanism is most effective for a system with high sonic mach number as well as large aspect ratio.

While we have demonstrated that the electrodynamic forces acting upon the system will tend it toward an axially contained state, it remains to be shown that this configuration is stable to the various interchange modes which plague the standard mirror geometry. The suppression of magnetohydrodynamic instabilities is due to the concomitant velocity shear which exists within the system.

In a non-rotational mirror system the flute-type mode has been shown to possess an instability growth rate [23]

$$\gamma_{\text{int}} \propto \frac{c_s}{\sqrt{L_p L}} \quad (1.13)$$

Where  $L$  and  $L_p$  are the axial length and pressure scale size respectively.

As the magnetic field lines in contact with conducting surfaces will not rotate we find that the radial velocity profile of the rotational discharge will be highly sheared. Thus a stabilizing shear criterion acting on the radial scale length  $L_R$  can be expressed in terms of the previously enumerated sonic Mach number and the magnetic Reynolds number  $R_\mu$ . For a system such as MCX, if supersonic flows on the order of

$$M_s > \left[ \frac{L_R}{L} \ln(R_\mu) \right]^{1/2} \quad (1.14)$$

can be reached, then the effect of these instabilities can be suppressed.

Given this conclusion, a reactor point for an MCX type system has been calculated [21]. To reach a toroidal sonic mach number sufficient for confinement ( $M_s = 6$ ) at ion temperatures favorable for fusion ( $T_i = 13 \text{ keV}$ ) while maintaining a rotational velocity below the Alfvén speed ( $v_A = B^2/\mu_o\rho$ ), the discharge would need to be able to support an electric field of 10 MV/m across a midplane radial extent of 1.1 meters with a midplane magnetic field of 2.6 Tesla. However, if those parameters can be achieved the return ratio of output power to input power should be  $\approx 100$ .

While this is far outside our present parameter set, it is the ability to physically

realize a well confined discharge, and its behavior congruent with the underlying theory, which stands as the focus at this juncture. To that end, this dissertation deals primarily with the explanation and classification of the various features of the MCX discharge, as well as present performance limitations found therein. To aid in this objective, these limitations have been divided into two general classes, namely engineering limits, and physical limits.

The first class are those restrictions which are due to externally induced constraints. For example, evidence suggests that a higher central magnetic field coupled with a strong mirror ratio will increase the available discharge voltage as well as reducing the Alfvén mach number, possibly leading to enhanced confinement. However increasing the field at this time is not possible given the power supplies and electromagnets presently available.

This first class of limits also includes discharge restrictions resultant from physical vessel geometry. To cite another example, extrapolations upon present data suggest that a marginal increase in the radial plasma extent, from 20 cm to 30 cm, could possibly increase the holding voltage of the discharge by nearly a factor of 2. However accomplishing this would require a complete redesign of the vacuum vessel and as such is also not possible on a short term scale.

Finally, limits surmounted through small scale design modifications, such as the ability to eliminate large scale discharge transitions by careful consideration of insulator geometry, close out the initial limitation class.

The second classification is comprised of fundamental discharge limitations which have been shown to be manifest throughout the entire parametric space. Primary among these is the rediscovery of a ceiling on the accessible rotational velocity ( $v_\phi$ ) in MCX, consistent with the Critical Ionization Velocity Phenomenon ( $v_\phi \leq \sqrt{2e\Phi_i/M_i}$  for the ionization potential  $\Phi_i$ ) which has been historically shown [8] to have limited similar classes of rotating discharge experiments.

The ability to surpass or circumvent these myriad limitations concludes the discussion, along with a rough modeling of the scalability of MCX into future iterations given the present limiting factors.

## 1.2 Summary of Results

This dissertation deals primarily with the explanation and classification of the various features of the MCX discharge, as well as present performance limitations found therein. Chapter 2 describes the mechanical setup of the MCX system, while Chapter 3 enumerates the primary features of the discharge itself.

Limits within the discharge have been uncovered through independent perturbation of the available variational parameters as listed in table 1-1. The results of these experiments are covered in Chapters 4 and 5 and have been summarized below.

Variable	Range
Capacitor Bank Voltage	5 - 18 kV
Series Resistance	1/2 - 16 $\Omega$
Midplane Magnetic Field	1 - 3.8 kGauss
Mirror Ratio	4 - 8
Capacitor Bank Size	30 - 60 caps @ 176 $\mu$ F
Radial Extent	10, 13, 16, 20 cm
Background Fill Pressure	50 $\mu$ Torr - 50 mTorr
Disk Insulator Position	Mirror throat - MT + 13"
Insulator Composition	HDPE, Macor
Insulator Geometry	Flat, Grooved

Table 1.1: The variational parameter ranges available to MCX. This table lists the parameters which have been explored during the course of this research, and denotes the range over which these parameters have been scaled.

The initial rows described in table 1-1 (bank voltage and series resistance) denote the parameters whose variation requires the most minor of external adjustments to accomplish. We have therefore, by design, been able to determine the effect of a variation in these initial parameters within a great many of the MCX performance subspaces. Experiments conducted at alternate magnetic fields, alternate fill pressures, and alternate radial extents have all been accomplished by an initial adjustment of the primary parameter ( $B(\text{kGauss})$ ,  $p(\text{mTorr})$ ,  $a(\text{m})$ ) followed by a secondary scan of the bank voltage so as to better determine the requisite performance effect congruent with the subspace. Such a comparison is possible due to the robust behavior of the discharge under variations of the bank voltage and series resistance. This allows any deviations to be attributed to the primary parametric adjustment.

Variations of the midplane magnetic field (row 3 of table 1.1) have been shown to have a substantial effect upon the holding voltage of the discharge. A factor of two increase to the value of the midplane field will result in a commensurate increase in the holding voltage of the discharge. However it has been noted that, as the bulk rotational velocity of the discharge is inversely proportional to the magnetic field, this increase in holding voltage does not result in an increased rotation velocity.

Scaling the magnetic mirror ratio, as outlined in row 4 of table 1.1, does not have as significant an effect upon the discharge. There is a mild positive scaling of plasma performance with enhanced mirror ratio, however this effect has been shown to level off above a mirror ratio of 7.

Augmentation of the supply capacitor bank (row 5 of table 1.1) has led to an increase in the duration of the discharge, consistent with an increase in the available stored energy in the bank. Thus the duration of an experimental run has been extended to 50 msec without the onset of catastrophic instabilities. However, the additional initial energy does not appear to boost the discharge performance beyond this temporal extension.

Alterations to the midplane radial extent of the discharge (row 6 of table 1.1) have been accomplished by short-circuiting the innermost plasma carrying magnetic flux surfaces. This has been accomplished by utilizing sets of aluminum clamps attached to the high voltage core. All discharge performance indicators have been found to scale strongly with radial extent and extrapolations on present data suggest that a marginal increase in the present maximal radial plasma extent, from 20 cm to 30 cm, could possibly increase the holding voltage of the discharge by nearly a factor of 2. However accomplishing this would require a complete redesign of the experimental vacuum chamber.

Adjustments have been made to the background Hydrogen gas fill pressure in which the MCX discharge is struck. As shown in row 7 of table 1.1, discharges have been created in background fill pressures ranging from 50  $\mu$ Torr to 50 mTorr. Variations in discharge behavior and diagnostic performance have been noted and we conclude that under the current auspice of a self initiated discharge created by the externally applied electromagnetic fields, operations at the present nominal fill pressure of 5 mTorr appear to be ideal.

The insulator dependant variables, as noted in the rows 8 - 10 of table 1.1 (Insulator position, composition, and geometry) have been observed to effect the probability that the MCX discharge will transition from a high confinement state (H-mode) into an ordinary confinement state (O-mode). Through careful choice of values for these parameters we have discovered the ability to eliminate these transitions completely. This allows the discharge to remain in an H-mode state for the full duration of the experiment. However, beyond this bifurcation further adjustments to these parameters do not appear to result in notable performance gains.

Examining the full scope of the parametric variations, as discussed in Chapter 5, has shown that the MCX discharge appears to be velocity limited. Through experimentation with an alternate dominant fill gas (Helium) we have determined that this limitation appears to be consistent with Alfvén's theory of a Critical Ionization Velocity. Consequences of this limitation upon the MCX system are discussed in Chapter 6.

## Chapter 2

### Mechanical Setup

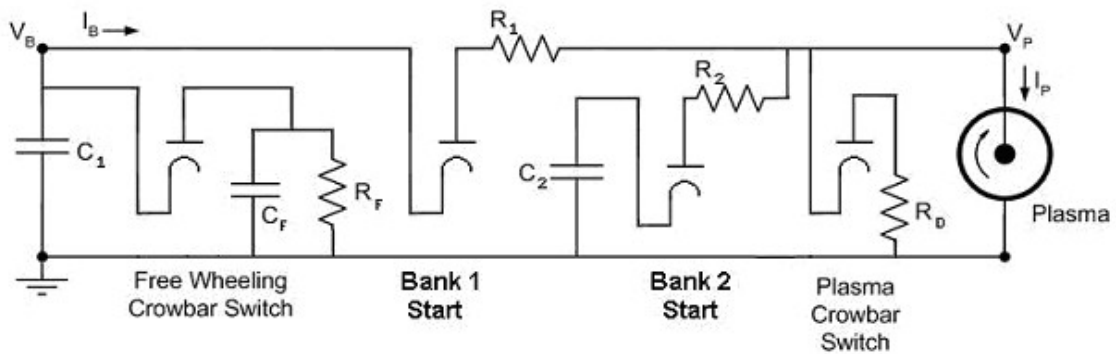


Figure 2.1: This circuit diagram depicts the multi-stage 20 kV capacitor bank which powers the MCX discharge.  $C_1$  and  $C_2$  are the independently operated source capacitor banks while  $C_F$  is the freewheeling capacitor bank.  $R_1$  and  $R_2$  are referred to as the series resistances while  $R_F$  and  $R_D$  are the freewheeling dump resistor and the modified crowbar dump resistor respectively

### 2.1 Introduction

The discharge performance of the MCX rotating plasma is highly dependent upon the initial parameters. Discharge mode, plasma voltage, and overall plasma resistance can all be affected by a fortuitous choice of input settings. Thus a brief summarization of these components will form an underpinning upon which to base the discussion of their effect upon the discharge.

In this Chapter we outline the major components of the discharge circuit and their uses. We will also discuss the ability to physically model the MCX discharge through a series of simple circuit elements [5] as this capability has proven extremely valuable from a diagnostic standpoint. In addition the ability to decouple the discharge through a process termed freewheeling [11] has provided a direct measurement of the momentum confinement time of the discharge. Comparisons between this method and the more robust crowbar technique, whereby the momentum confinement time is inferred from the current reversal at the termination of the discharge, shows a solid agreement between these independent measures. Finally, we conclude this discussion of the external components of MCX with a brief overview of the major diagnostic systems which have been utilized to analyze the discharge.

## 2.2 Discharge Circuit and Constituent Parts

The input power required to create and sustain the MCX discharge is created by a set of high voltage dielectric capacitor banks. Once this primary bank has been fully charged and the external power supply removed from the circuit, a system trigger activates the start ignitron and couples the capacitor bank to the high voltage core through a current limiting series resistance. The substantial negative voltage applied to the core accelerates the surplus electrons along the externally applied magnetic field lines causing an Penning type cascade which results in a near complete ionization of the discharge region. Upon reaching a fully ionized state, the remaining

voltage on the core will then induce the plasma into rotation. At the desired end of the discharge a crowbar ignitron is triggered, electrically grounding the core of the vessel. This removes the electric field and driving current, terminating the plasma. By adjusting the timing of the crowbar ignitron, the duration of the discharge can be varied between 2 and 50 milliseconds

### 2.2.1 Bank Setup

The full capacitor bank is subdivided into two identical sections, each consisting of 30 capacitors which have been electrically connected in parallel. These will be heretofore referred to as Bank 1 and Bank 2. Within these larger banks, each individual capacitor is rated to 20 kV and has a capacitance of approximately  $60 \mu\text{F}$  for a total stored energy of 12 Kilojoules per cap. Thus the full capacitance of the system is 3.6 mF with a maximum stored energy of 760 kJ. Presently, when both are active, the two banks are charged concurrently and then disconnected from each other as well as the single charging supply, thus allowing for independent operation.

### 2.2.2 Ignitrons

To satisfy the switching requirements of the MCX circuitry we employ several ignitron type mercury vapor switches. The ignitron is able to hold off the kilovolt level charging voltages until triggered, and is also capable of handling the full kiloamp current during discharge. Physically, the anode and cathode of the switch

are both enclosed within a glass tube. The cathode is surrounded by pool of mercury while the corresponding anode is positioned directly above it. To ‘close’ the switch an igniter pin initiates a small arc discharge which vaporizes a portion of the mercury pool. Once vaporized the mercury facilitates excellent electrical contact between the anode and the cathode while the primary current through the switch sustains the ignitron discharge. The switch is able to reset into its non-conductive ”open” state when the current within the ignitron drops below a level necessary to maintain the mercury vaporization.

Note that it is entirely possible for the current to drop quickly enough such that there is an inductively driven overshoot resulting in the ignitron conducting in the reverse direction. Thus, to shut off the ignitron effectively the current must be dropped below the sustainment current value ( $< 100$  Amps) and maintained at that level for a duration longer than the quenching time of the mercury plasma.

### 2.2.3 Series Resistance

The current limiting resistors on each branch of the circuit are non-inductive bulk ceramic resistors manufactured by Kanthal Globalbar (formerly Ceswid) and range in value from 1 to 4 ohms. A gantry has been assembled which will accept 8 of these resistors per discharge bank. By implementing various series and parallel combinations we are able to vary the external resistance from a fraction of an ohm up to 16 ohms thus limiting the current flow into the plasma.

It is important to note that when firing both banks, the effective series resistance as seen by the plasma is the parallel combination of the Bank 1 and Bank 2 series resistor arrays due to the superposition of the two resultant currents. Thus if one wished to determine the effect of a dual bank discharge (60 caps) as compared to a single bank discharge (30 caps) the series resistance for the latter case would need to be  $1/2$  the former in order to maintain an equivalent parameter set.

### 2.3 Plasma Crowbar and Current Reversal

After the external high voltage power supply has deposited the requisite amount of charge upon the bank, it is disconnected from the circuit and the start ignitrons are fired. Termination of the resultant plasma discharge is initiated by the application of a secondary ‘crowbar’ ignitron which connects the high voltage core to an electrical ground. This serves to both dump the excess charge remaining on the capacitor bank as well as short circuit the voltage present on the core. While a true crowbar would connect the core directly to a solid electrical ground, this union is presently made through a  $1/2 - 1/4$  Ohm dump resistance, the reason for which will be explained presently. We note first that irrespective of the dump resistor, the purpose of this crowbar type connection is to facilitate a recovery of the angular momentum stored within the discharge through a current reversal within the plasma.

This reversal is due to the behavior of the rotational discharge as a hydro-magnetic capacitor with an associated leakage resistance, a model whose physical underpinnings will be outlined in section 2.4.1 . This behavior allows the calculation of the momentum confinement time of the plasma from the recorded current trace in the following manner

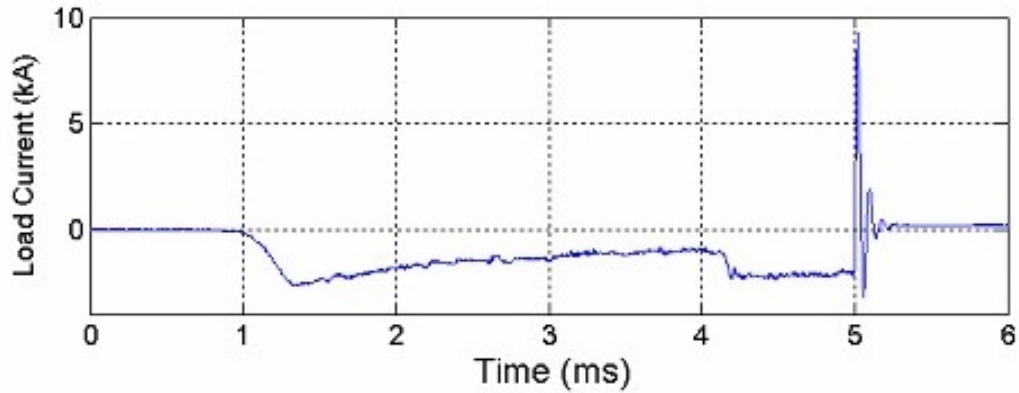


Figure 2.2: The load current through the MCX discharge. Note the reversal of the plasma current at  $t = 5$  ms corresponding to the firing of an unmodified crowbar ignitron ( $R_D = 0$  Ohms). An integration of this signal for the  $500 \mu\text{sec}$  after the application of the crowbar leads to a measure of the effective stored charge within the "plasma capacitor" allowing for a calculation of the momentum confinement time of the discharge.

### 2.3.1 Calculation of the momentum confinement time and interpretation of the stored charge

From the circuit model of the discharge, as shown in figure 2-3, the characteristic RC decay time, which we interpret as the plasma's momentum confinement time ( $\tau_M$ ), is computed from an integration of the plasma reversal current  $I_P$  at the crowbar divided by the value of the current immediately preceding the crowbar.

$$\frac{\int_{\text{crowbar}} I_P dt}{I_P} = \frac{Q_P}{I_P} = \frac{C_P V_P}{V_P/R_P} = C_P R_P = \tau_M \quad (2.1)$$

Where the subscript P has been utilized to denote the plasma quantities : resistance( $R_P$ ), capacitance( $C_P$ ), charge( $Q_P$ ), voltage( $V_P$ ) and current( $I_P$ ).

This decay time is interpreted as the momentum confinement time by noting that for a radial current

$$j_r = \frac{mn}{B_z} \cdot \frac{du_\phi}{dt} \quad (2.2)$$

we have

$$Q = \int I dt = \int \int_{\text{vol}} \frac{mn\dot{u}_\phi}{B_z} d^3x dt = \frac{\pi l(r - r_0)^2}{B_z} mn\dot{u}_\phi \quad (2.3)$$

Which results in

$$\tau_M = \frac{p_\phi}{\dot{p}_\phi} = \frac{mn\dot{u}_\phi}{mn\ddot{u}_\phi} = \frac{\left[ \frac{QB_z}{\pi l(r - r_0)^2} \right]}{\left[ \frac{\dot{Q}B_z}{\pi l(r - r_0)^2} \right]} = \frac{Q}{\dot{Q}} = \frac{Q}{I} \quad (2.4)$$

Just as in the circuit decay.

Before proceeding it is necessary to address the question of the physical meaning behind the quantity  $Q$ , which has been referred to as the 'stored charge'. For a non-dissipative system, this quantity has been shown [38, pg 504] to be equivalent to the charge added into the system. For MCX however, this quantity is a measure of the angular momentum stored within the discharge. The application of a strong transverse current leads to an acceleration of the plasma and thus an increase in the angular momentum. The quantity resultant from an integration of the current reversal pulse which occurs upon a crowbarring of the discharge is a recovery of this transverse current. Therefore the 'stored charge'  $Q$  is not a measure of any sort of real charge stored within the system, but a quantification of the angular momentum resident within the discharge.

### 2.3.2 Necessity of a modified crowbar

Historically on MCX, the plasma crowbar switch directly connected the core of the vessel to a solid electrical ground. The stored charge, and thus the momentum confinement time of the discharge was then calculated by means of a direct integration of the undamped ringing current reversal (see Fig. 2.2). We were forced to abandon this method due to severe mechanical complications within the ignitron firing chassis.

The ignitron firing chassis would spontaneously activate, thus triggering the requisite ignitron irrespective of the receipt a triggering pulse. This fault mode would

trigger all the ignitrons simultaneously causing the full charge from the capacitor bank to be immediately dumped through the crowbar portion of the circuitry prior to plasma generation. The exact source of this difficulty within the old ignitron firing chassis is still unknown, however the problem has been rectified by means of a change in hardware to a new set of fiber coupled ignitron triggering devices.

These new fiber coupled solid state devices are much more reliable than the previous hardware and have yet to demonstrate the triggering problems which the previous firing chassis were subject to. However, there does exist a detriment to their implementation. These new devices have been found to be a great deal more sensitive to a reversal of the current through the ignitron than were the older firing chassis, a condition which is known to exist during the ringing portion of the plasma crowbar process.

This sensitivity is due to the possibility that during a reversal of current through the ignitron there may exist a transient arc created between the cathode and the igniter pin which causes a current surge into the ignitron triggering device. While not a common occurrence, the statistical probability of such an event and the requisite downtime resultant from the repair procedure are cause enough to minimize the likelihood of such an occurrence. This has been accomplished by the installation of a dump resistor into the crowbar portion of the circuit.

The dump resistor is able to eliminate the ringing within the plasma crowbar

sub-circuit by a direct damping of the reversal. An unfortunate, but expected consequence of this addition is that the validity of our prior direct integration method of determining stored charge within the plasma has been compromised. To counter this effect, corrections have been made to the crowbar calculation to recover the stored charge information.

### 2.3.3 Modified Crowbar Calculation and Errors

By performing a transient circuit analysis on the MCX power circuitry both immediately prior to and after the firing of the modified crowbar (denoted by the subscripts P and A respectively in the following equations) we are able to recover a measurement of the charge present upon the "plasma" capacitor (shown in Figure C.1) at the moment of crowbar. This measurement is based upon the observed current reversal as well as the resistance settings for the circuit.

Assuming that the voltage on the capacitor bank ( $V_B$ ) does not change appreciably during the timescale of the firing of the crowbar ( $\sim 10 \mu$  sec) the voltage on the bank immediately before (2nd term) and after (3rd term) the crowbar can be shown to be

$$V_B = I_P (R_S + R_P) = I_A \left( R_S + \frac{R_D R_P}{R_D + R_P} \right) \quad (2.5)$$

Where  $R_S$ ,  $R_P$ , and  $R_D$  are the series, plasma and dump resistances respectively.

The current ( $I_A$ ) through the series resistance after the crowbar is fired is therefore

$$I_A = \frac{(R_S + R_P)I_P}{R_S + \frac{R_D R_P}{R_D + R_P}} \quad (2.6)$$

This results in a post-crowbar expected plasma voltage of

$$V_A = V_B - I_A R_S = V_P + I_P R_S - I_P \left[ \frac{R_S + R_P}{R_S + \frac{R_D R_P}{R_D + R_P}} \right] R_S \quad (2.7)$$

Coupled with the assumption that the capacitance of the plasma remains the same, this leads to an equation for the total charge on the plasma capacitor  $Q_P$  as a function of the charge lost from the plasma capacitor during the crowbar  $Q_T$ . Explicitly, the equations are:

$$C_P = \frac{Q_P}{V_P} = \frac{Q_T}{V_P - V_A} \quad (2.8)$$

$$R_P = \frac{V_P}{I_P}$$

$$Q_P = \frac{Q_T R_P}{R_S} \left[ \frac{1}{R_S + R_P} \frac{R_S + R_P}{R_S + \frac{R_D R_P}{R_D + R_P}} - 1 \right] \quad (2.9)$$

Which, after some manipulation results in

$$Q_P = Q_T \left[ 1 + R_D \left( \frac{1}{R_S} + \frac{1}{R_P} \right) \right] \quad (2.10)$$

We note however that the quantity  $Q_T$  is the total charge which is removed from the capacitor during the reversal. This is not the same as the quantity of charge calculated by an integration of the reversal spike. The charge which exits the plasma capacitor is channeled both through the dump resistor as well as the plasma resistor. However, as the charge that is directed through the plasma resistor cannot be measured directly, an additional correction factor must be added to the preceding equation.

This correction factor is deduced by noting that the total current flowing off the charged plate is  $I_T = I_{RP} + I_{RD}$  and that

$$I_P R_P = I_D \frac{R_D R_S}{R_D + R_S}, \quad (2.11)$$

Solving for  $I_T$  and integrating over the current reversal we find

$$\int I_T dt = Q_T = Q_R \left( 1 + \frac{R_D}{R_P \cdot \frac{R_S}{R_S + R_D}} \right) \quad (2.12)$$

Resulting in our final correction factor for the reversal charge coming from the plasma capacitor.

$$Q_P = Q_R \left( 1 + \frac{R_D/R_P}{1 + R_D/R_P} \right) \left( 1 + R_D \left( \frac{1}{R_P} + \frac{1}{R_S} \right) \right) \quad (2.13)$$

This correction factor was tested on a control load consisting of a single high voltage capacitor connected in parallel to a resistor, thus simulating the plasma. The series and plasma resistances were varied from 1 to 4 ohms and the crowbar

resistance was alternated between 1/2 and 1/4 ohms. Comparing the recovered charge recorded from the control load shots with the theoretical charge on the control capacitor we found a maximum error of 10% when the "plasma" resistance was at its lowest value (1 Ohm), and a nominal error of less than  $\pm 5\%$  for all other plasma resistance values. This irregularity is comparable to the error associated with our voltage and current diagnostics and thus the correction factor for the crowbar calculation was determined to be adequate and was adopted into the subsequent diagnostic recordings.

The only further benchmarking which could be accomplished is a live discharge test of the calculation. As the control of this experiment would entail removal of all dump resistance so as to return to a true crowbar scenario for comparison, it was not attempted due to the possibility of damage to the fiber coupled ignitron triggering chassis. However, there exists no fundamental reason that such a process could not be attempted. As another independent check, an alternate method of deriving the correction factor was calculated and the results, which match exactly, can be found in Appendix C.

## 2.4 Controlled Plasma Load

The rotating MCX plasma may be modeled as a dielectric capacitor with associated leakage resistance. As these physical components are readily accessible we have undertaken to create a controlled plasma load which is comprised of just

such circuit elements. This “dummy load” consists of a single high voltage capacitor rated to 11 KV with a capacitance of 176  $\mu\text{F}$ . Connected to this capacitor are between one and four high current non-inductive bulk ceramic resistors valued at 1 Ohm  $\pm 10\%$ . The full setup is then connected in parallel to the terminus of the high voltage input cables coming from the capacitor bay. We note here that the precise wiring of the connection still leaves the core of the machine connected into the circuit thus maintaining the vacuum capacitance.

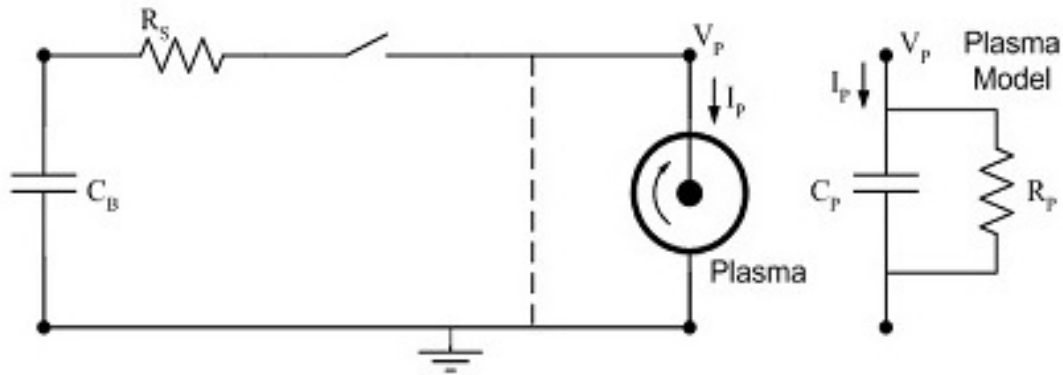


Figure 2.3: A 0-D model of the MCX discharge. Kinetic energy stored in the rotation of the plasma allows it to be modeled as a capacitor  $C_p$  in parallel with a leakage resistance  $R_p$ . These components are substituted for the plasma in order to create a control load.

We prevent a plasma discharge from forming by maintaining a high vacuum within the experimental chamber during these control load shots. Thus the inserted “dummy load” now functions strictly as a control plasma with the associated machine behavior subtracted out.

### 2.4.1 Supporting Theory

The ability to model a rotational plasma load as a set of circuit elements has been well documented (9, 11). At its most basic level, the configuration of the MCX experimental chamber is in itself a coaxial capacitor. An application of simple electrostatic theory finds that given our geometry, the ideal capacitance of the vessel and core setup, under a moderate vacuum of  $10^{-7}$  Torr is

$$C = \frac{Q}{V} = 2\pi\epsilon_0 \cdot \frac{L}{\ln(R_2/R_1)} \propto 100 \text{ pF} \quad (2.14)$$

A more detailed calculation of this quantity arrived at by utilizing an estimated plasma volume through field line mapping leads to a vacuum capacitance of 53 pF [48]. Thus there is a small but fundamental capacitance associated with the physical setup of MCX. The addition of a discharge into this static volume creates a substantial transverse dielectric constant. As MCX is well within the bounds enumerated by MHD theory we can assert

$$\rho \frac{dv_\phi}{dt} = \mathbf{j} \times \mathbf{B} - \mu v_\phi \quad (2.15)$$

where  $\rho$  is the requisite density and  $\mu$  is a viscosity term

Computing the perpendicular component of the volume current, and recalling that  $v_\phi = \mathbf{E} \times \mathbf{B}/B^2$  we have

$$\rho \frac{d}{dt} (\mathbf{B} \times v_\phi) - j_\perp B^2 + \mu (\mathbf{B} \times v_\phi) = \rho \frac{d}{dt} E - j_\perp B^2 + \mu E \quad (2.16)$$

By solving for  $j_\perp$  and dropping the viscosity term, which accounts for a leakage current through the plasma and thus the plasma resistance, we find through judicious application of Maxwell's equation that

$$\nabla \times \mathbf{B} = \mu_0 \left( j_\perp + \epsilon_0 \frac{dE}{dt} \right) = \frac{1}{c^2} \left( 1 + \frac{\mu_0 c^2 \rho}{B^2} \right) \frac{dE}{dt} \quad (2.17)$$

This results in  $\epsilon_R = 1 + \frac{\mu_0 c^2 \rho}{B^2} \sim 1 \times 10^6$  for standard MCX discharges, which leads to a plasma capacitance on the order of 100  $\mu\text{F}$ . Reincluding the viscosity term now introduces a loss mechanism through which charge can be transported between the 'plates' of the capacitor. These losses are manifest in a transverse current and can be utilized to calculate a plasma 'resistance'.

We note that a quotient of the plasma voltage over the plasma current can be interpreted as a bulk plasma 'resistance' if and only if one assumes that the majority of the current has traveled cross-field through the volume of the plasma. If there exist alternate current paths, then they must be accounted for and our simple model may no longer result in an accurate plasma 'resistance'.

## 2.4.2 Practical Implementation and Plasma Comparison

Having connected a control load to our power circuit, we are able to ascertain the validity of our simplistic plasma model through a battery of test shots. As shown in Fig. 2.3, the location of the current and voltage diagnostics allows us to compare the recordings taken with the dummy load to those which occur under standard experimental conditions.

While acknowledging that this simple model does not attempt to account for any of the initial breakdown activity, and noting that the recorded plasma resistance is not constant during a discharge as opposed to the static resistor attached to the dummy load, we assert that during the quasi steady state period of the discharge the control load and plasma load can be said to be undergoing similar behavior. Therefore the conclusion drawn, for purposes of this dissertation, is that the dummy load is similar enough to the plasma load such that the results garnered from a test of the alternate freewheeling crowbar method under rigid control should roughly translate to an actual discharge taken under similar circumstances and thus give comparable results.

## 2.5 The Freewheeling Crowbar

Decoupling the rotational plasma load from the capacitor bank (freewheeling) should allow for a direct measurement of the plasma decay time. However, successful

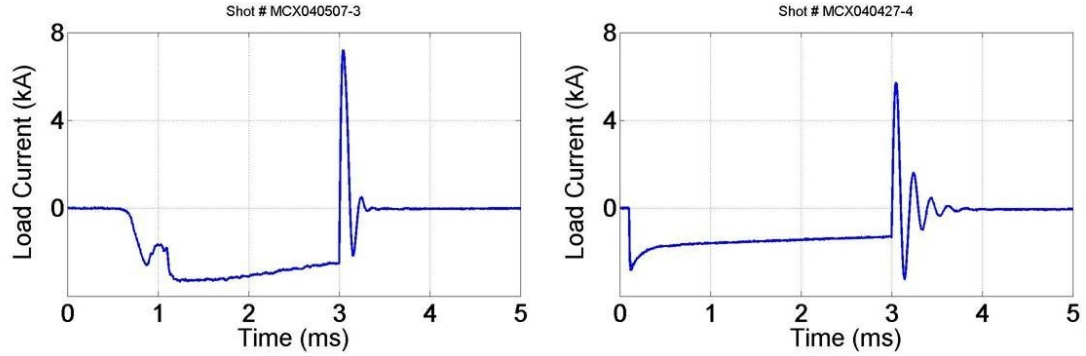


Figure 2.4: Comparison of recorded current reversals on the Plasma Load (right) and the Control Load (left). An examination of these traces displays the similarities in gross overall behavior which allows for the adoption of the control load as a predictor for approximate plasma performance. Integration of the current reversal reveals a capacitance for the Plasma Load of  $178 \mu\text{F}$  as compared to Control Load capacitance of  $176 \mu\text{F}$ .

freewheeling of the discharge requires that all connection between the core and the capacitor bank be severed, otherwise crosstalk with the original source bank will contaminate the result. This severance is accomplished by rapidly quenching the conductive mercury vapor discharge within the start ignitron, opening the requisite portion of the circuit. Once the ignitron no longer conducts, the decay of the plasma voltage should be a directly measurable exponential which corresponds to the momentum loss of the plasma.

In order to achieve freewheeling, the current through the start ignitron, as labeled on Fig. 2.1, must not only drop to a level low enough such that the power influx is no longer sufficient to support the mercury vapor discharge, it must also happen slowly enough such that there is no reversal current. This second constraint

is a direct result of the capability of the ignitron to conduct in both normal (cathode to anode) and reversed (anode to cathode) biases.

We meet these conditions by rapidly removing the voltage differential present across the start ignitron and series resistance. Without any potential difference to drive it, the current through this ignitron quickly goes to zero. To accomplish this, a second ignitron, labeled the "freewheeling crowbar" is fired. This ignitron is responsible for connecting the initial capacitor bank to a secondary bank which is initially uncharged with respect to ground. The resultant redistribution of the charge on the start bank between these two sets of capacitors now leaves us with a single larger bank at a significantly lower voltage.

The magnitude of the capacitive value of the auxiliary bank is actually the result of a calculation of the conservation of charge at the moment of the freewheeling crowbar trigger. This is so that, upon a redistribution of stored charge, the difference between the bank voltage and the discharge voltage will be lower than the holding anode rating of the ignitron thus curtailing the current flow through the series resistance and "opening" the ignitron switch.

$$Q = C_B \cdot V_B = (C_B + C_D) V_P \quad (2.18)$$

$$C_D = \frac{V_B - V_P}{V_P} \cdot C_B$$

In the preceding equations  $V_P$  is the plasma voltage that had been recorded at the crowbar time on a previous shot under similar discharge conditions and  $V_B - V_P = I_P R_S$  where  $R_S$  is the known series resistance and  $I_P$  is the plasma current also recorded from the previous shot.

Attached in parallel to the freewheeling bank is a dump resistor which allows the charge remaining on the banks to drain quickly to ground. The value of this resistor needs to be small enough to allow the bank side of the circuit to drain more rapidly than the plasma side, otherwise the ignitron will spontaneously reignite. That being said, the resistance cannot be too low, as this would cause the ignitron to ring due to the inductive response of the capacitors.

If the conditions on both the bank and the plasma are met, the ignitron will cease conduction approximately 150 - 200  $\mu s$  after the firing of the freewheeling ignitron as shown in Fig. 2.5.

### 2.5.1 Test Setup

The initial tests of the freewheeling crowbar were performed on the previously described control load at resistances ranging from one to four ohms in single ohm steps. During the first set of experiments at a particular resistance, the ‘plasma’ crowbar was fired and the stored charge computed from the recorded current reversal. From this measurement a decay time was calculated using equation 2.1. A second set of experiments was then performed whereby the freewheeling crowbar

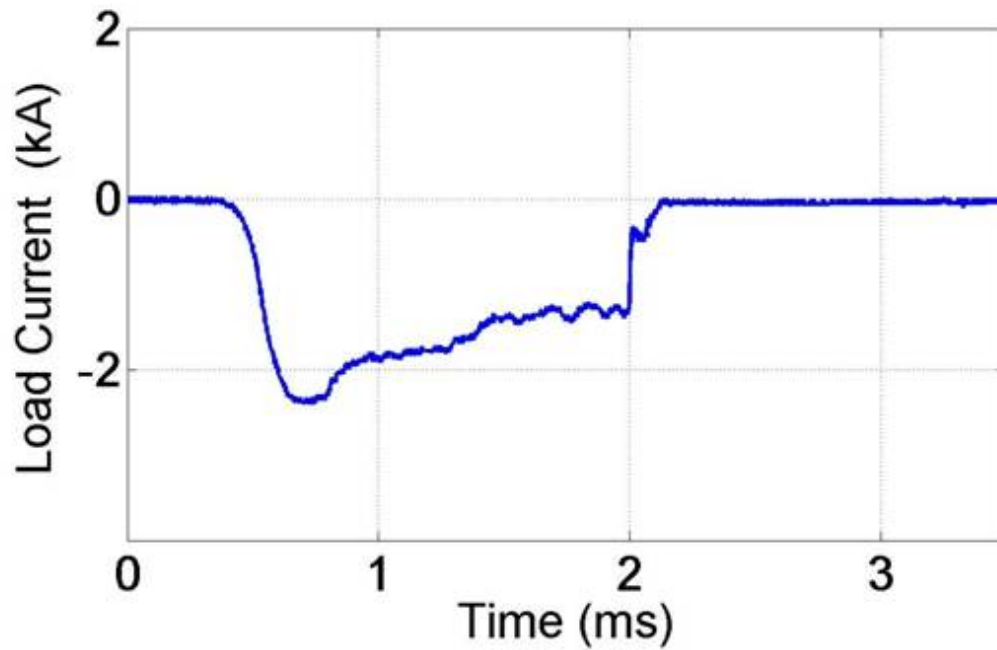


Figure 2.5: Typical freewheeling current trace for a plasma load. This shot was taken under standard conditions with an initial voltage of 7 kV, a midplane mirror field of 2 kG, a mirror ratio of 9, a series resistance of  $1.5 \Omega$ , an initial bank size of  $19 \times 176 \mu\text{F}$  and a freewheeling bank size of  $12 \times 176 \mu\text{F}$ . The freewheeling crowbar was fired at  $t = 2 \text{ ms}$  with confirmed shutoff of the start ignitron at  $t = 2.2 \text{ ms}$

was activated instead of the nominal plasma crowbar. An exponential curve was fit to the decay on the voltage trace and the resultant decay time recorded. These separately obtained decay times were then compared to each other, as well as to the decay time expected from the known values of the physical components.

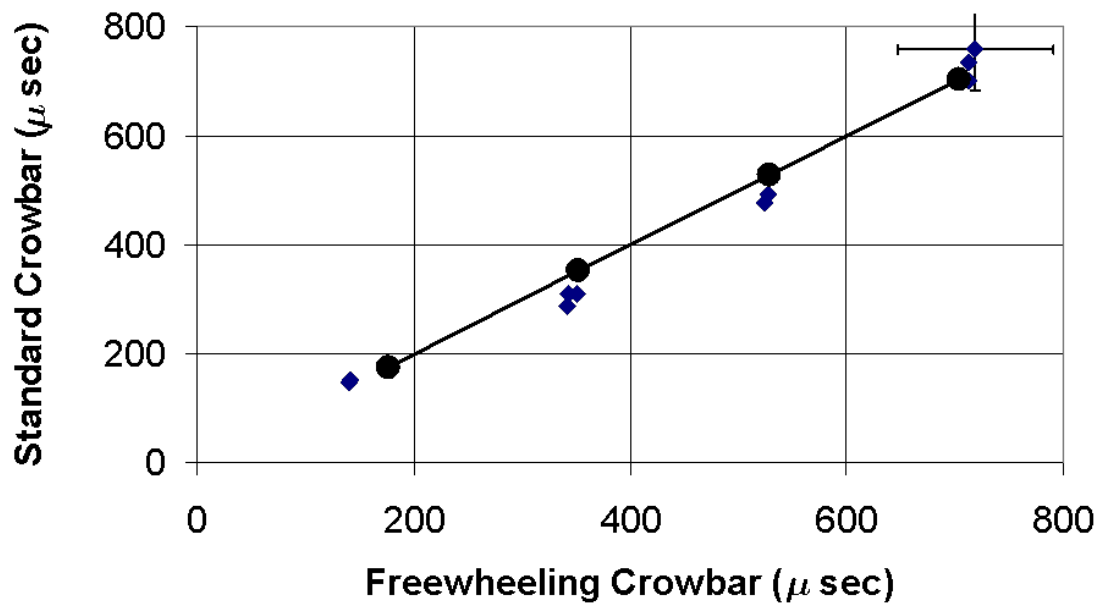


Figure 2.6: Comparison of decay timescales for standard and freewheeling control load shots. The decay time of each crowbar type is plotted on an axis, with the diamonds representing a recorded pairing of experimental crowbar values taken under identical conditions. The solid dots represent the theoretical decay values for  $R$  equal to 1, 2, 3, and 4 Ohms and a capacitance of  $176 \mu\text{F}$ . Representative error bars are displayed for the data point in the upper right of the graph

As shown in Fig. 2.6, the three methods delivered very similar numbers for the full range of resistors. It should be noted however, that freewheeling in the higher plasma resistance cases is a much more reliable measure due to the increased decay time of the load side of the circuit. The increased reliability is partially due to the fact that the ignitrons that we are utilizing are a great deal more susceptible to a spontaneous re-ignition than they are to a ringing discharge. Thus while we were able to convincingly freewheel with a tau of only 176  $\mu\text{sec}$ , it required a greater tuning of the circuit conditions (i.e.:  $C_D$ ) than did the longer decay times.

A simplistic force balance model shows that when decoupled from its driver, a rotating plasma should decay exponentially due to internal viscous forces. Thus if we are successfully turning off the start ignitron, the voltage on the control load will decay as  $V \sim V_0 e^{-t/\tau}$ . A logarithmic plot of the plasma voltage for a range of control load resistances (Fig. 2.7) shows that this is indeed the case.

The comparison of the circuit predictions and the actual data confirms that we are shutting off the start ignitron in the manner previously suggested. Were this not the case the slope of the exponential decay would more closely resemble that of the capacitor bank's decay time. This fault result has been confirmed through a deliberate unbalancing of the previously enumerated capacitor assisted freewheeling circuit.

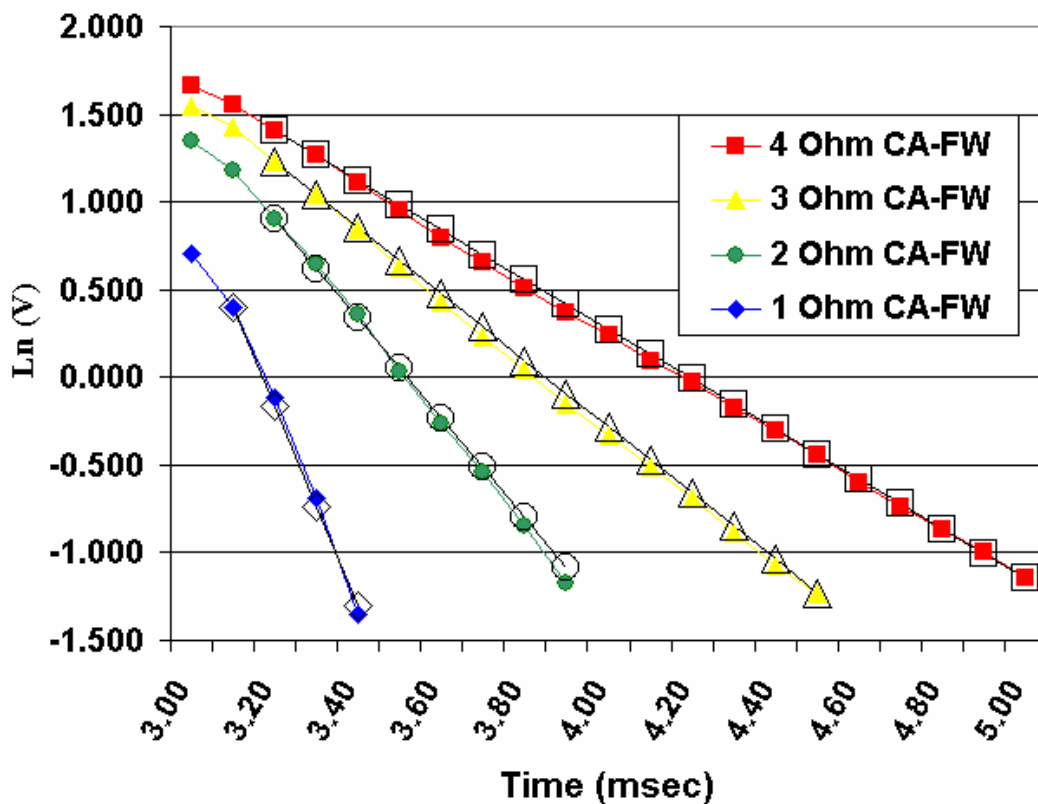


Figure 2.7: logarithmic decay of various control loads. Under the same conditions as Fig. 2.6, the decaying dummy load voltage is graphed on a logarithmic scale as solid plot points. Then, taking a voltage value directly after the crowbar time we calculate the logarithm of the load voltage given the expected decay time of the circuit components and graph these as hollow plot points. The strong agreement is evidence that the freewheeling crowbar is behaving as expected.

## 2.5.2 Freewheeling Experiments

Having demonstrated the ability to create the freewheeling condition in the control load, we return our experiment to its nominal setup with a true plasma load. As detailed in Chapter 3, MCX has two distinctive discharge modes. The H type modes (both HR and HV) have a higher stored energy, higher voltage, lower current and thus a greater plasma resistance (as defined by  $V_p/I_p$ ) than the O type modes. As had been noted with the control load, it is significantly easier to freewheel in cases such as these and thus we were able to achieve positive results with little difficulty. Our canonical result, displayed in the following figure shows that for identical initial conditions the decay times for the standard and freewheeling crowbars are in agreement to within 5%, which is within the acceptable error for these two measurements. Thus we are able arrive at an independent method for determining the decay time of the plasma which confirms the results of the nominal crowbar method in use since the experiment's inception.

## 2.5.3 Freewheeling Limitations

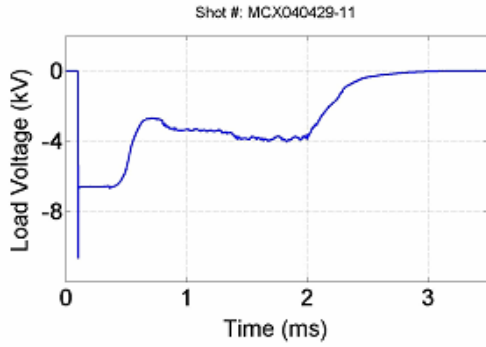
Attempts to freewheel a discharge consisting of a minimal stored energy and low plasma resistance (O type modes) have been mostly unsuccessful. This failure is due more to the rapid decay of the plasma while in this mode, than to any fault of the system. As the momentum confinement time in O-mode can be characterized as mildly poor and the voltage decay time rapid, once the discharge is decoupled from

the bank, the holding voltage across the plasma is lost extremely quickly. Thus the removal of charge from the bank by means of the dump resistor is not rapid enough to balance out the circuit, thus leading to a spontaneous reignition of the ignitron. This reignition allows additional current into the plasma contaminating the result. It is theorized that this problem could possibly be mitigated by reducing the value of the dump resistance further, however any attempts at this must be done carefully as we are nearing a regime whereby the capacitor-dump resistor sub-circuit will become underdamped leading to a harmful ringing both in the ignitrons as well as the capacitors. A further option includes the utilization of a smaller initial capacitor bank. This method would result in a shorter decay time, but is not optimal for fulfilling research criterion. The possibility of utilizing other switching methods has also been explored. However, pursuit of these options is has been mitigated by the fact that the O-mode is simply not the desired operational state, and as such further study on the merits of these possibilities has been limited.

## 2.6 The MCX Diagnostic Suite

In this section we briefly detail the major diagnostics utilized on the MCX system. This is intended simply as an enumeration of the various subsystems, and not a definitive guide as to their mode of operation or founding principles. Those not familiar with these type of diagnostics are directed to Ref [19]

Diagnostic signals from the MCX discharge are recorded onto a set of National



Shot Information for MCX040429 - 11  
 Tau (freewheel) = 222  $\mu$ s  
 C = 75  $\mu$ F  
 Q = 279 mC

Shot Information for MCX040429 - 12  
 Q (crowbar) = 285 mC  
 C = 77  $\mu$ F  
 Tau = 212  $\mu$ s

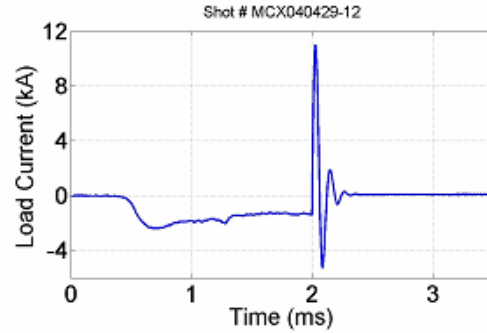
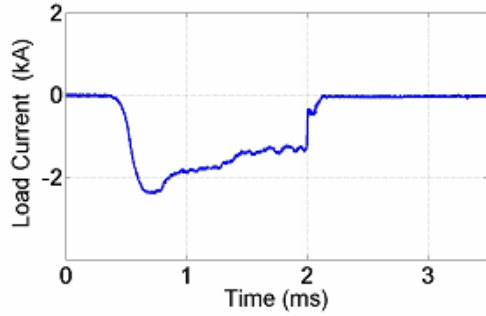


Figure 2.8: Tau comparison for the benchmark H-mode freewheeling crowbar test. The decay time recorded from the voltage trace of a freewheeling discharge (upper left) is nearly identical to the decay time calculated from the current reversal of an equivalent discharge (lower right) using the standard crowbar technique. The current trace for the freewheeling discharge (lower left) is included to demonstrate the rapid cessation of discharge current. The conclusion reached here is that the interpretation of the standard crowbar as a measurement of the momentum confinement time has been correct.

Instruments NI-6133 simultaneous sampling digital acquisition boards at a digitization rate of 1 MHz. As it is relevant for some of the diagnostics, we also note that each channel maintains an input impedance of  $1M\Omega$ . Post-discharge, the recorded data channels are saved by shot number and channel name both within the data acquisition computer as well within as the MCX control computer. For example, the plasma voltage recorded on the 5<sup>th</sup> plasma run of August 16<sup>th</sup> 2006 would be saved under the file name *MCX060816-05 Plasma Voltage.txt*.

Data within these diagnostic files are saved in two columns. The first column contains data which has been calibrated for its specific diagnostic, and the second column is the raw voltage signal recorded by the digitizer. The calibrations effected for each type of diagnostic are performed in the *Channel Save.vi* LabVIEW file.

### 2.6.1 Voltage Measurements and Calibrations

The canonical “plasma voltage” referenced throughout this thesis is in actuality a measurement of the voltage between the high voltage core and a ground reference located at the data acquisition system as recorded by a 2320:1 voltage divider and attendant low pass filter.

The signal must be grounded at the point of digitization due to large fluctuations in the value of the local ground at the vessel during the discharge. In addition to this limitation, we also concede that our method of determining the discharge voltage external to the vessel carries with it no profile information and thus any con-

cerns about sheath effects or radial penetration of the electric field must be answered in a more circumspect manner.

The initial calibration of the diagnostic was the result of a voltage divider calculation and a final calibration of these probes was then performed by monitoring the output voltage while connected to a known voltage source. Voltage measurements have been deemed accurate to within 5%.

## 2.6.2 Current Measurements and Calibrations

Current measurements are taken via a 445 turn Rogowski coil which surrounds the primary cable connecting the capacitor bank and the core. It has been installed immediately prior to the interface between these two sections. The Rogowski coil records the time derivative of the current through the cable. This signal is then connected to an integrator to recover a true current measurement. As this solid state RC integrator has an extremely long integration time ( $\tau = 104$  msec) the resultant output signal is relatively small. To compensate for this, the signal is passed through a  $10\times$  amplifier before being recorded into the data acquisition system.

Quantitative calibration of the Rogowski coil is a multi-step process. While a zeroth order calibration can be done by application of Ampere's law, as the equation below shows, there are additional dependencies to be considered.

$$V = An \cdot \mu_0 \frac{dI}{dt} \quad (2.19)$$

Here  $V$  is the output voltage,  $A$  is the area of a loop winding, and  $n$  is the winding density. Routing this signal into an RC integrator results in an signal voltage that is now a function of the current passing through the enclosed wire.

$$V = \frac{An}{RC} \mu_0 I \quad (2.20)$$

While it would be possible to simply record the raw signal and then integrate it once the signal has been digitized, the additional benefit of the solid state integrator as a filtering device make it a preferred, if anachronistic choice. However this does introduce an additional minor correction factor as there is a minute charge buildup on the integrating capacitor. Thus the final equation [19] for the current is

$$I(V) = \frac{RC}{An\mu_0} \left[ V + \frac{1}{C} \left( \frac{1}{R} + \frac{1}{R_L} \right) \int V \right] \quad (2.21)$$

As we do not possess a power supply capable of sourcing the kiloamps required for a reliable signal measurement, a final calibration of the diagnostic was performed on the previously enumerated control load. By monitoring the quotient of the independently calibrated voltage measurement with the current trace, we arrive at a resistance which can be compared to the “plasma” resistance existent on the control load described in section 2.4. Typical results are displayed in Fig. 2.9.

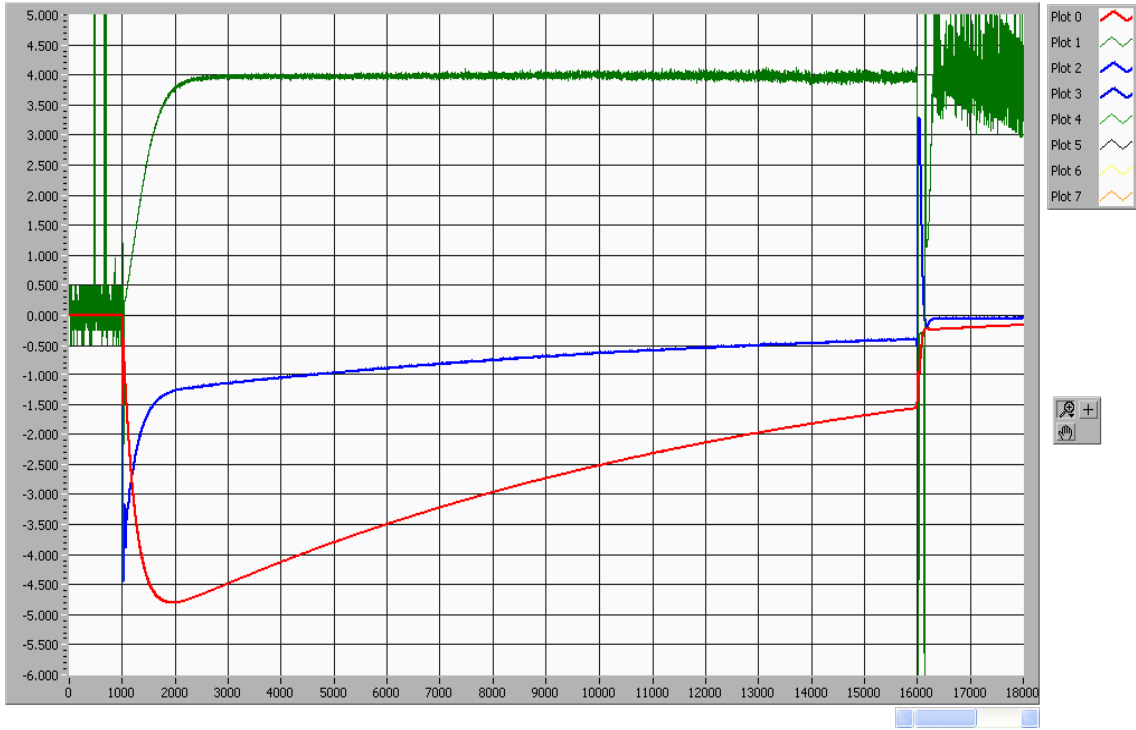


Figure 2.9: The raw signal from a experiment undertaken with a known control load displays the final calibration of the plasma current diagnostic. The quotient of the plasma voltage (red trace) recorded in kilovolts, with the plasma current (blue trace) recorded in kiloamps, results in an effective plasma resistance (green trace) calculated in Ohms. This can be easily compared to the physical value of the "plasma" resistance which was known to be  $4 \Omega$ . The above graph is a screen capture of the raw data output from a LabVIEW data acquisition program

### 2.6.3 Photodiode Diagnostic

An  $H_\alpha$  emissions monitoring system has recently been added to the MCX diagnostic suite [17]. External to the vessel are several sets of passive photodiode detectors which monitor the discharge through a number of viewports. These assemblies are presently equipped to record the intensity of the first Balmer spectral line from Hydrogen and from this measurement recover information germane to a discernment of the neutral population within the MCX discharge. For each of the MCX photodiodes, a plano-convex lens located external to the vessel focuses the visible discharge emission onto the tip of an optical fiber. The fiber transmits the signal to a second lens at the data acquisition site which collimates the exiting light prior to attenuation by a standard interference filter centered at 656 nm with a 10 nm passband. The signal then illuminates a photodiode detector. The photodiode sources a current proportional to the radiative flux received by the detector and this current is routed through an operational amplifier prior to being recorded as a voltage in the data system.

There are at present, a total of 7 detectors focused at various  $z$  locations along the transverse axis of the vessel. Each of these detectors possess a radial view of the discharge and relative calibration of these various photodiode lines has been accomplished through inter-line comparisons of a standard source. If radial profile information is required, the lens assemblies can also be arranged in a single  $z$  location to form a multi-chord array. These measurements are utilized to determine

the neutral density and profile [18] within the system

#### 2.6.4 Spectroscopic measurement of rotation velocity

Spectroscopic measurements of the MCX discharge [25, 24, 26] are utilized to determine a variety of local plasma features. The existence of lines other than the backfilled hydrogen indicate the presence of impurities within the discharge. The source and strength of these impurities may affect the interpretation of results. For example, as will be discussed in sections 3.4 and 4.5, when high density polyethylene cuffs are utilized as part of the insulator assembly there is a significant rise in the post shot fill pressure. Evidence suggests that this rise in pressure is due to an ablative removal of a monolayer of the plastic insulator. If that is indeed the case, then the timing of this event is of extreme importance due to the fact that once this bloom has occurred, the discharge becomes carbon mass dominated. The relative strength of the carbon II - IV spectral lines present throughout the discharge has been utilized to determine the temporal location of this surge in impurity concentration.

That being said, the primary function of the spectrometers attendant to the MCX system is to provide information about the rotational velocity of the discharge, as well as some insight into the operational temperature. Radially off axis observation of the ionized impurity spectral lines (as shown in Fig. 2-10) allows for a measurement of the Doppler shift of the line when compared to a laboratory rest

frame. Measurements taken both above and below the centerline of the vacuum vessel confirm  $\mathbf{E} \times \mathbf{B}$  rotation of the bulk discharge [20].

In addition to rotational information, thermal broadening of the emission line allows an order of magnitude estimate of the ion temperature. This information, coupled with the absence of atomic transitions past a certain energy level is utilized to determine an upper bound to the temperature of the MCX discharge. This is a critical number, as the figure of merit for centrifugal confinement theory is the sonic mach number.

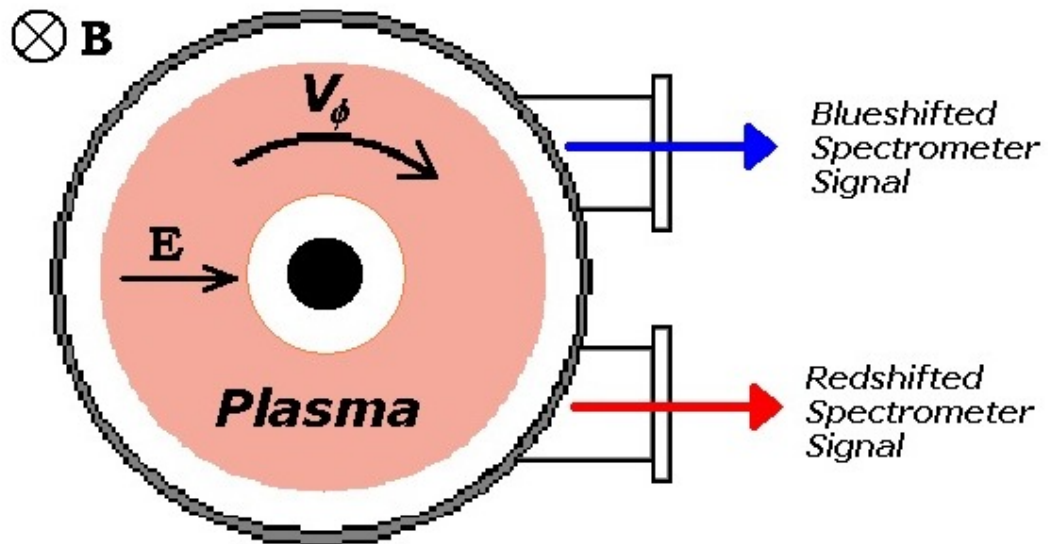


Figure 2.10: MCX spectroscopic arrangement. MCX has the ability to record midplane spectroscopic measurements both above and below the centerline of the vacuum vessel allowing confirmation of the direction of bulk plasma rotation as predicted by  $v_\phi = \mathbf{E} \times \mathbf{B}/B^2$ .

There is also smaller broadband spectrometer attached to the system. This smaller spectrometer, manufactured by Ocean Optics is able to record the entire visible spectrum with a 10 nm resolution and is employed in the diagnosis of major plasma characteristics.

### 2.6.5 Magnetic Probes

Resident within the scrape-off layer of the MCX discharge are several magnetic fluctuation diagnostics. Through Faraday's law, the voltage fluctuations present on a set of wire loops immersed in a magnetic field are directly proportional to the differential changes in the magnetic flux which transits the loop. These rapid changes in the magnetic field are due to inhomogeneities within the plasma which give rise to localized volume currents. Thus, these magnetic probes provide a record of the local structure of the discharge, as opposed to the voltage and current diagnostics which are a volume averaged global measurement.

The majority of the data reported herein has been recorded on a set of  $x$ - $y$ - $z$  triplet probes (referred to as the MS probes, displayed in Fig. 2.11) which are legacy items culled from the remains of the Maryland Spheromak [35]. Each of the MS probes contains a triplet of loops at three distinct radial locations.

There is also some preliminary data from a multi-point  $B_z$  array which has been installed on the inner wall of the vacuum vessel adjacent to a limiting flux surface. The purpose of this array is to attempt to discern modal perturbation

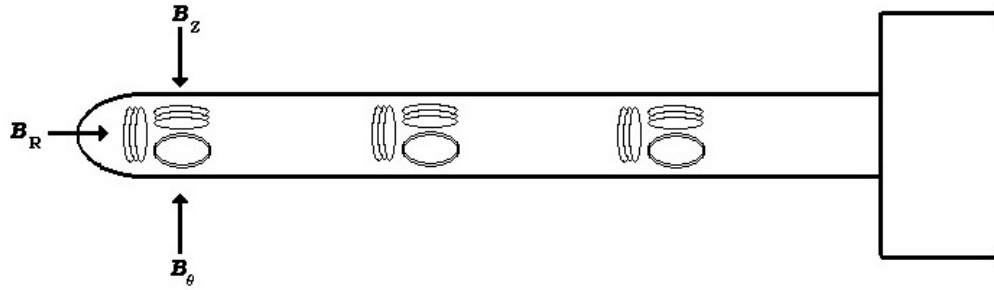


Figure 2.11: The "MS" magnetic probes in MCX contain three  $dB/dt$  pickup loops ( $R, \theta, Z$ ) at three distinct radial locations for a total of nine signals per probe.

numbers within the discharge. The sixteen probe locations allow for a resolution of azimuthal mode numbers up to  $m = 8$ .

Finally, external to the vessel are a set of circumferential loops which are sensitive to the diamagnetic properties of the discharge. Although precise information pertaining to discharge instability formation has yet to be culled from the recorded data, we have noted [15] extremely useful zeroth order information about the plasma performance during various discharge modes.

## Chapter 3

### The MCX Discharge

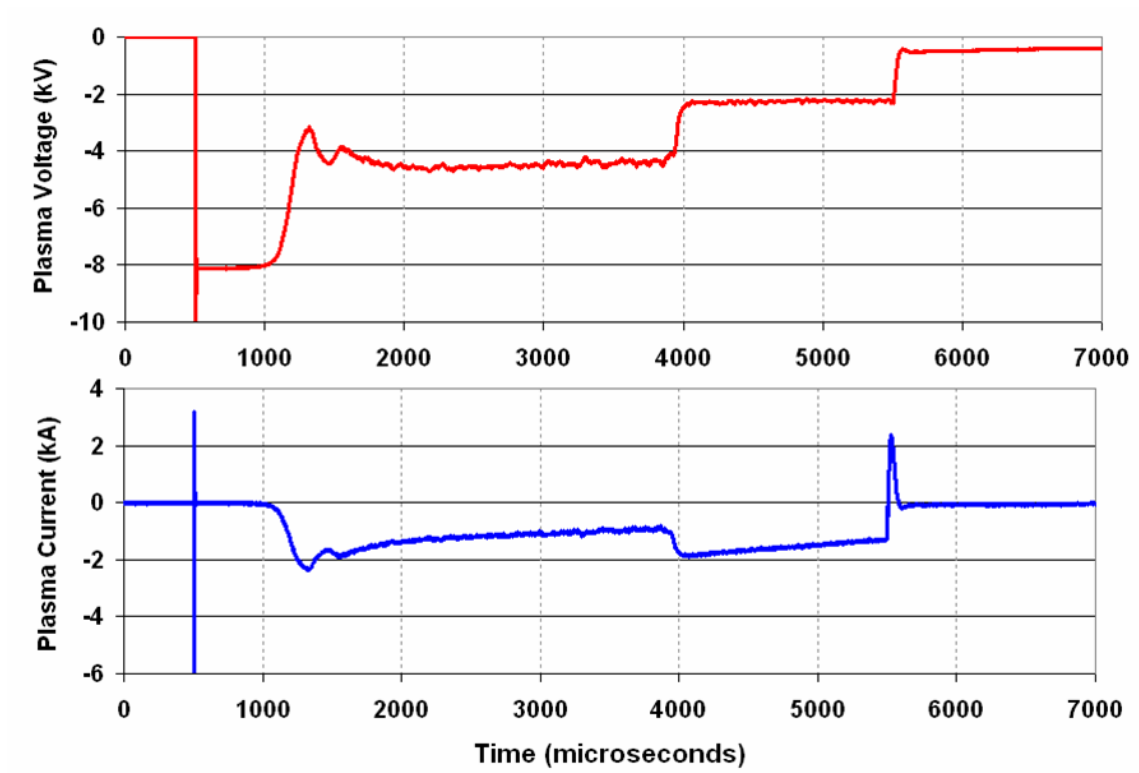


Figure 3.1: Plasma Voltage and Current traces for a standard MCX discharge. (MCX060915-1) This discharge was generated from an initial capacitor bank voltage of 8 kV, a series resistance ( $R_s$ ) of 2  $\Omega$ , a fill pressure of 5 mTorr, a central field strength of 3.8 kGauss, and a mirror ratio of 4.4. Plasma breakdown occurs at 1ms, with a transition from an H-type to an O-type mode at 4ms and a plasma crowbar at 5.5 ms. The single reversal spike noted on the current trace is a result of the modified crowbar system.

### 3.1 Introduction

There are several distinct stages present in a standard MCX plasma discharge, as shown in Fig. 3.1. A transient holding phase is achieved after the firing of the start ignitron. During this time, the core is raised to the same electrostatic potential as the capacitor bank. As the backfilled gas is not yet ionized, there is no plasma activity present.

The ionization event, instigated by the elevated voltage on the core, occurs quickly thereafter and the plasma begins its rotation. The first mildly quiescent phase is a high voltage state, termed the "H mode". The H mode displays supersonic rotation velocities, and is stable for many MHD timescales. It is possible for the discharge to remain resident in an H-mode until quenching however, some H modes will spontaneously decay into the ordinary mode (O mode).

The O mode is characterized by a lower holding voltage as well as a lower rotation speed, higher current, and a uniform magnetic activity throughout the chamber. This mode is capable of being supported until such time as the power influx into the discharge is no longer capable of maintaining ionization. However, this terminating condition is rarely reached as the plasma crowbar ignitron is usually triggered during one of the previously enumerated quasistatic modes

## 3.2 Voltage Holdoff and Initial Plasma Breakdown

The transition from the initial holdoff mode into a rotational discharge is a spontaneous process whose duration is dependant upon both the initial bank voltage and magnetic field strength at the midplane of the vessel as well as the fill pressure. There appears to be an empirical dependence between the ratio  $E/B$  and the duration of time spent in the holdoff mode.

### 3.2.1 Ionization Model

Studies of the ionization of a neutral gas within a strong crossed field geometry similar to the MCX system have been performed [45, 46, 42] and their results are similar to those observed on the present discharge.

Some time after the application of the external magnetic fields, triggering of the start ignitron raises the high voltage core to the same electrostatic potential as the capacitor bank. This deposition of charge creates a radial electric field. Examining the interior limiting magnetic flux surface, one which just contacts the core at the mirror throat, the voltage drop along this field line from the mirror throat to a point  $P$  at the midplane is given by

$$V(P) = - \int_a^P \frac{\lambda}{2\pi\epsilon_0 r} dl \quad (3.1)$$

For a standard 8 kV bank voltage, this results in a potential difference between

a point on the surface of the core ( $a = 2$  cm), and the field mapped midplane location of the first good flux surface ( $P = 6$  cm), of approximately 2kV

Thus the center of the field line is initially at a substantially lower electrostatic potential than the ends, which are still attached to the core. Since the vacuum electric field is not fully orthogonal to the magnetic field, it is therefore capable of accelerating the electrons along this field line and thus supplying the necessary ionization energy. Also, as the motion perpendicular to the field is magnetically inhibited, the innermost flux surface has been shown to exhibit a strong buildup of electrons [8].

These conditions suggest that the initial ionization mechanism is accomplished by trapped electrons as in a Penning type discharge [36]. Electrons from the core are conducted down this field line to the center of the vessel, they overshoot and are bounced back and forth in simple harmonic motion. If sufficiently energetic then this will result [46] in ionization of the surrounding neutral gas.

Thus the ionization rate of the MCX discharge should be proportional to the applied voltage, and inversely proportional to the magnitude of the magnetic field as well as the background fill pressure. While never explicitly recorded, this is a characteristic which has been noted throughout the experimental run.

Upon ionization, the resultant charged particles should begin the standard  $\mathbf{E} \times \mathbf{B}$  rotation. Rotating spokes of just this nature have been observed during the acceleration phases of several rotating plasma experiments [9]. This ribbon, after

a small number of rotations was noted [31] to develop into a spiral structure thus facilitating the creation of an azimuthally homogenous breakdown and resulting in the observed volumetric discharge. Thus it is not surprising that calculations have shown (see section 4.2.1) that the steady state MCX discharge is fully ionized

The energy expended in the initial startup of the MCX system can be divided into two phases, the ionization phase, and the acceleration phase. As an order of magnitude estimate of the energy required for ionization, we assume a density equivalent to that of the backfill gas ( $n = 3.5 \times 10^{20}$  particles/m<sup>3</sup>) and a cylindrical volume for the solenoidal region. Thus, assuming no losses during the ionization process the energy is required is

$$E_i = Ne\Phi_H \approx 350 J \quad (3.2)$$

Where  $\Phi_H$  is the ionization energy of Hydrogen in electron volts,  $e$  is the fundamental charge unit and  $N$  ( $= n\pi L(.28^2 - .08^2)$ ) is the total number of particles.

A similar order of magnitude estimate of the energy expended during the acceleration phase can be accomplished by noting the kinetic energy of the steady state discharge ( $v_\phi = 80$  km/sec)

$$E_r = \frac{N}{2}m_p v_\phi^2 \approx 850 J \quad (3.3)$$

To determine the percentage of the total system energy expended in the initial

discharge phase we estimate the change in the capacitor bank ( $C_B = 1.8 \text{ mF}$ ) voltage.

$$\Delta V = \left[ \frac{2(E_r + E_i)}{C_B} \right] \approx 1kV \quad (3.4)$$

Thus, the voltage available for the quasistatic portion of the discharge is approximately  $1kV$  less than the initial bank voltage.

### 3.3 H Type Modes

The preferred modality of the MCX rotational discharge is an H type mode. However, the analysis of these discharges is mildly complicated by the present supposition that there exist two distinct H type modes, classified as the HR (high rotation) mode and the HV (high voltage) mode. Though the externally measurable characteristics of these two modes are extremely similar, there is the noted exception of the system's measured rotation velocity. For an as yet undetermined reason the HR mode has been noted to exhibit a rotational velocity nearly twice that of the HV mode.

#### 3.3.1 The High Rotation mode

Historically, the first elevated discharge mode to be discovered on MCX was the High Rotation(HR) mode. The HR mode is denoted by a holding voltage of 3–5

kV on the core and a measured rotation speed of  $\sim 200$  km/sec [47]. This rotational velocity is computed from a measurement of the Doppler shift of a Carbon IV spectral line. If we assume a plasma temperature of 30 eV, which is not inconsistent with thermal broadening of the emission lines, this results in a sonic Mach number, defined as the ratio of the toroidal flow speed over the sound speed, of approximately three. In order for MCX to obtain this velocity and still be consistent with the  $E \times B$  drift equation, the radial extent of the plasma at the midplane must be compressed from 20 cm to a width of 13 cm. While the nascent cause behind this radial compression is not well understood, there are at present several conjectures which will be covered in section 4.3.3. In addition, we also note that C II and C III did not display rotational velocities in excess of 200 km/sec, but recorded velocities closer to 40 and 140 km/sec respectively [47].

The HR mode is also denoted by a higher activity level at the midplane magnetic probes as referenced to the probes at the mirror throat as well as a higher stored energy and longer confinement times. However, the initial HR type discharges recorded in 2003 and 2004 were not without detracting features. Primary among these was the presence of a transition within the discharge. All HR type discharges were noted to undergo a transition into an O-type mode. While extensive parameter scanning resulted in an ad-hoc set of guidelines which was able to maximize the length of the HR mode, there was never any indication that it was possible to avoid this transition altogether. This situation is of course extremely deleterious if one wishes to commission the operation of a steady state fusion type

reactor based upon this confinement scheme.

In addition, during the time HR modes were recorded a portion of the insulating assembly had been manufactured out of a high density polyethylene, which is not an optimal choice as a plasma facing component. The consequence of this selection being a uniformly dense carbon coating on the Pyrex backing disks due to ablative contact between the polyethylene and the discharge. In addition, macroscopic carbon deposition was noted on the interior vessel walls. This carbon layer on the walls was extensive enough at its maximum that it formed a hydrocarbon sheet which was able to be peeled off. This carbon deposition extended from the insulator location fully into the midplane of the vessel, albeit with a decreasing density. The subsequent replacement of the plastic cuff with a piece of similar geometry manufactured out of the machinable ceramic MACOR led to the discovery of the HV mode.

### 3.3.2 The High Voltage Mode

Replacing the plastic portion of the insulation assembly with a geometrically equivalent piece created out of MACOR and then later, a slightly more radially extensive disk of grooved MACOR (See section 4.1 for specific insulator discussion) resulted in the discovery of a new high voltage mode (HV mode). While displaying a similar holding voltage of greater than 3 kV across the discharge, it differs from the HR mode by the lack of a triply ionized carbon signal denoting rotation velocities

upwards of 200 km/sec. Thus the moniker High Voltage mode (HV-mode) has been adopted simply as a means of differentiation between this mode and its more rapid kin and not due to any greatly elevated discharge potential.

The rotational velocities recorded while in HV-mode are consistent with  $v_\phi = V_p/aB$  if one assumes that radial extent of the plasma is determined by the inner and outer limiting magnetic flux surface. This obviates the need for any radial discharge compression. The HV-mode also displays a similar momentum confinement time, plasma resistance, and stored energy as the HR type mode.

The other distinguishing feature which separates the two modes, is the ability to operate the HV-mode without transitions. Whereas an HR-mode discharge would always transition into an O-mode state after 2 - 4 ms, the extent of an HV type discharge is limited only by the capacitively stored energy available to offset viscous and recombinative losses. By increasing the size of the capacitor bank we have been able to extend the duration of the HV type discharge from 10 milliseconds up to almost 50 milliseconds with no indication of a gross destructive instability.

### 3.3.3 Modal Causality

As one might predict, a great many of the measurable performance factors of the discharge seem independent of the choice of insulating material, albeit with the single exception of rotational velocity. While there may be a minute difference in the location of the functional discharge parameter space, for example the discharge

achieved with a bank voltage of 7 kV and a series resistance of  $1.5 \Omega$  with a plastic insulator may be duplicated with a MACOR insulator at 8 kV and  $2 \Omega$ , for this pair of elevated discharge states (HR and HV modes) there is statistically no difference in the performance characteristics that are recorded. It is therefore the variation in rotational velocity which remains to be explained. In examining the various discharges and their governing equations, the assumption made to conform our spectroscopic measurement with the underlying theory was a radial plasma width of 13 cm. This inference appears to be consistent with interferometer based density measurements [48] undertaken in the HR-mode. Thus it is possible that one could view the elevated rotational velocity as a result of the compression of the radial extent of the discharge.

A few of the possible causes of such a compression are explored in the remainder of this section. In addition the results of several simple experiments conducted to determine the efficacy of these postulates will be presented. Finally, for completeness, we examine the possibility that there is no difference between the modes and examine the consequences of this conjecture.

In examining the possible differences between the plastic and MACOR insulators, two major divergent properties are the outgassing rate and the surface conductivity. The amount of material released from the polyethylene insulator during a discharge is enormous. As noted in section 4.1.3, there is a post shot rise in fill pressure recorded with the polyethylene inserts, whose magnitude is on the order of the fill pressure. Thus a discharge which began with a pressure of 5 mTorr could

terminate at a fill pressure 15 mTorr. This pressure rise is unique to the polyethylene inserts, and is never seen with a MACOR insert, thus giving credence to the ablative material removal theory.

The elevated impurity concentration from the polyethylene inserts could conceivably have a positive effect upon the discharge. If, during the formation phase of the discharge, a significant portion of the energy which would have been utilized in the heating of the plasma is lost due to neutral radiation, then it is possible that the discharge will be overall cooler. If this is the case, and if the bulk rotation velocity is equivalent to a discharge with a low impurity level, then the plasma will possess a comparatively elevated sonic mach number. As the efficacy of centrifugal confinement scales with the sonic mach number, it is possible that such a plasma could be strongly confined. This enhanced centrifugal confinement could pull the plasma towards the vessel midplane, thus shrinking the radial extent. Once decoupled from the insulator the subsequent acceleration could then increase the equilibrium temperature to the values observed.

A test of this theory was performed whereby the installation of a secondary gas inlet to the vacuum vessel which allowed the overlay of the backfilled hydrogen with a dopant impurity gas. The gas chosen for these initial experiments was nitrogen, due to its similarities to carbon in both mass and excitation energies. An additional .05 to 1 mTorr ( $\sim 1\% - 20\%$  by volume) was added to the standard 5 mTorr backfill and the singly through triply ionized nitrogen states were monitored for enhanced rotation velocities. While we were able to observe rotation on both N II ( $N^+$ ) and

N III ( $N^{++}$ ) spectral lines, velocities in excess of 100 km/sec were never observed. The caveat here being that since we were only able to record N II and N III with certainty, it is therefore not as close a correspondence to the 200 *km/sec* C IV data as one could wish. While it is possible that a larger impurity dopant is needed to generate this bifurcation in performance, a noted degradation of the discharge for dopant pressures  $\geq 1$  mTorr was observed, and as such the experimental run was discontinued.

A second possible explanation for the HR-mode radial discharge compression is based upon estimates of the fractional surface conductivity of high density polyethylene endplates. The ability of the ablated carbon to become mildly conductive could allow a shorting of the electrostatic potential present across the magnetic field lines which terminate upon the plastic inserts. Thus a majority of the electrostatic potential drop observed across the discharge would be located on field lines radially exterior to this piece. This hypothesis is the result of an observation that a discharge with a 13 cm radial extent would possess an interior first good flux surface which terminated at the edge of the high density polyethylene cuff. While these may be completely unrelated phenomenon, it is at least suggestive enough that further experiments needed to be conducted.

The results of a series of experiments conducted with a forced reduction in radial discharge extent can be found in Chapter 4.6. For the purpose of the present discussion it needs only be noted that while the utilization of Aluminum limiters to short out the most interior of the magnetic flux surfaces was successful in compress-

ing the discharge, there was not a resultant rise in rotational velocity as the voltage present across the plasma was also proportionally reduced.

Finally, there exists the possibility that there is in fact no substantial difference between HR and HV mode. This declaration leads to one of two conclusions. The first conclusion is that the lack of C IV signal is simply due to the reduced presence of carbon within the discharge. If we consider the observation that replacing the polyethylene with MACOR dropped all carbon impurity signatures by nearly a full order of magnitude, in conjunction with the knowledge that the fast C IV spectral signals were not exceedingly robust, it is possible that the signal is too small to be measured.

MCX has always observed [26] differential rotation speeds for various ionization states within the same impurity species. Thus if we compare the C II and C III signals which are observable in both HR and HV modes we find that the recorded velocity of these impurities is comparable for both of the H type modes. The conclusion drawn being that if we were able to locate a C IV emission, one might expect the rotational velocities to coincide here as well.

That being said, the alternate explanation must at least be acknowledged, namely that the previous data was misinterpreted and that the measurement of rotation velocities greater than 200 km/sec was unfortunately in error.

## 3.4 Discharge Transitions

There are spontaneous events which occur during the course of certain MCX discharges whereby the plasma rapidly decays from a higher discharge state into a lower one. This transition (noted at  $t = 4$  msec on Fig. 3.1) results in a loss of holding voltage, stored energy, rotational velocity and an overall degradation in plasma performance. As this is not a preferred operational mode, these transitions are examined in an attempt to determine their nascent cause and if possible, mitigate their presence through engineering. Data will be shown which seems to indicate that these transitions are not a fundamental limitation, but simply a result of a redirection of the current through the discharge. Explicitly we display strong evidence that the transitions are the result of an internal crowbaring across the surface of the end insulators which results in the creation of an alternate current path. We also demonstrate that this model is fully sufficient to forecast the numerous fundamental changes which are undergone during a modal shift.

### 3.4.1 Prevailing cause of MCX discharge transitions

At both the high voltage and near end of the vessel there exist insulating assemblies which terminate the magnetic field lines. Without these insulators unconfined electrons could easily traverse the field lines and short circuit the discharge. It now seems likely that during the course of a transitional discharge, these insulating assemblies allow the formation of a secondary surface breakdown which degrades

the primary discharge by creation of an alternate current path. This type of internal crowbarring has been documented in other rotating plasma devices [45, 22] and will manifest as an overall drop in the "plasma resistance" leading to a reduced system voltage. Thus, the conclusion reached is that the MCX discharge will spontaneously create an alternate insulator adjacent current path or paths which are responsible for the H to O modal shift within the discharge.

### 3.4.2 Photodiode recordings of transition induced optical bursting

To record any activity which might be coincident with the transition phenomena, a number of photodiodes were positioned such that the associated collection optics were focused at the front of the insulator assemblies. Throughout the course of this particular experimental run, both the high voltage (HV) and the near end (NE) insulating assemblies were positioned 11 inches outside the magnetic maximum. This position was determined by the availability of diagnostic access at this particular z location. Standard discharges were created and the signals recorded leading to the conclusions summarized in Figs. 3.2 through 3.6

### 3.4.3 Circuit Modeling of Discharge Transitions and Consequences

The primary assertion in this discussion of transitional discharges is that the event is caused by the formation of an alternate current path internal to the experimental vessel which is indistinguishable from the primary path when monitored

### Experiment MCX060413-07, No Transition

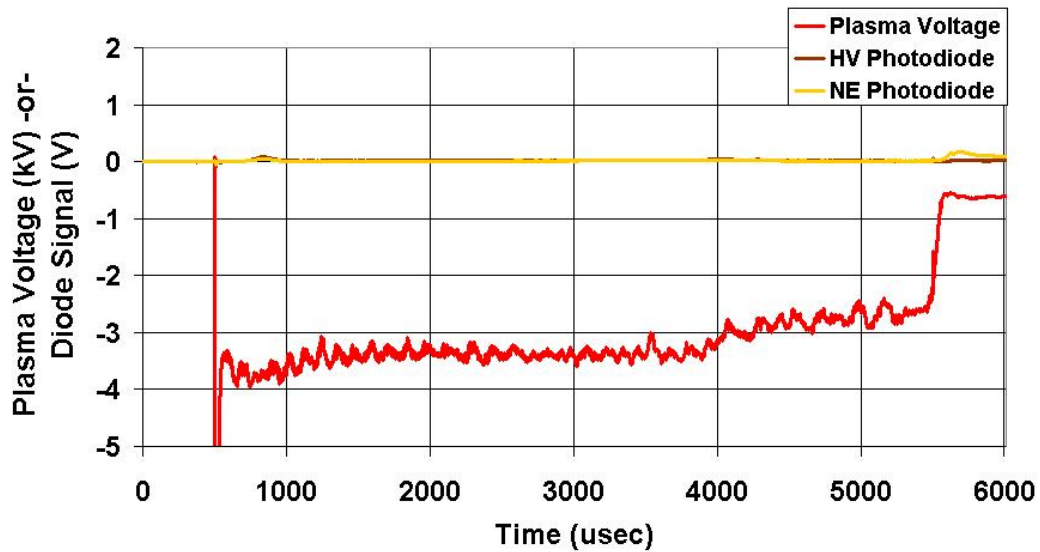


Figure 3.2: This figure depicts the voltage and photodiode traces for a discharge in which there is no transition event. It is included to permit comparisons to the attendant transition type discharges found in Figs. 3.3 and 3.4. It is also pertinent to note that the record of the plasma voltage for the time prior to the transitions denoted in the following figures is nearly identical to the measurement recorded for the non-transitional case.

### Experiment MCX060413-06, Transition noted at the Near End Insulating Baffle

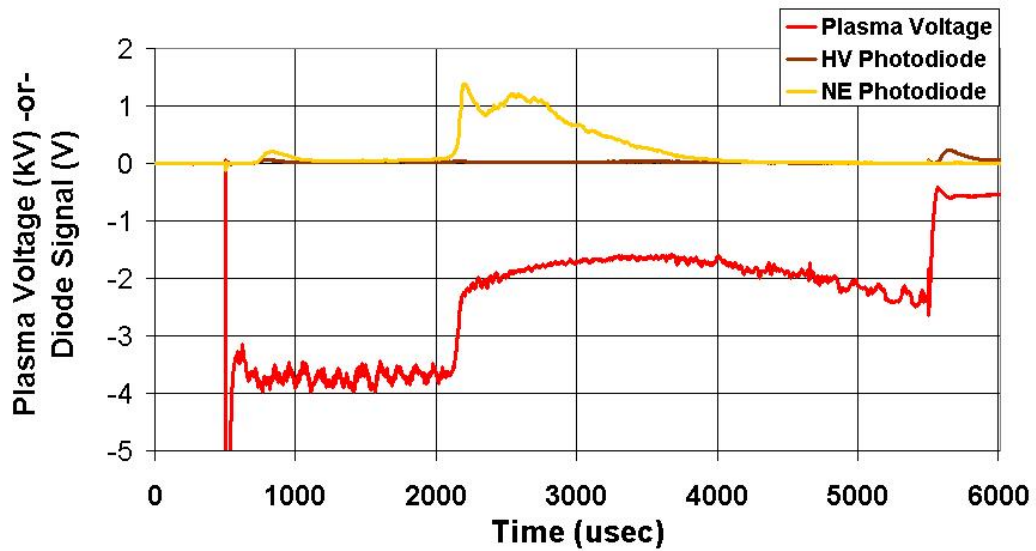


Figure 3.3: Standard MCX discharge with a transition from an H-type to an O-mode present at  $t = 2200 \mu\text{sec}$ . The coincident activity at the Near End(NE) and subsequent lack of activity at the High Voltage (HV) end would indicate that this transitioning discharge state is due to a localized phenomenon occurring at the near end.

### Experiment MCX060413-08, Transition Noted at the High Voltage Insulating Baffle

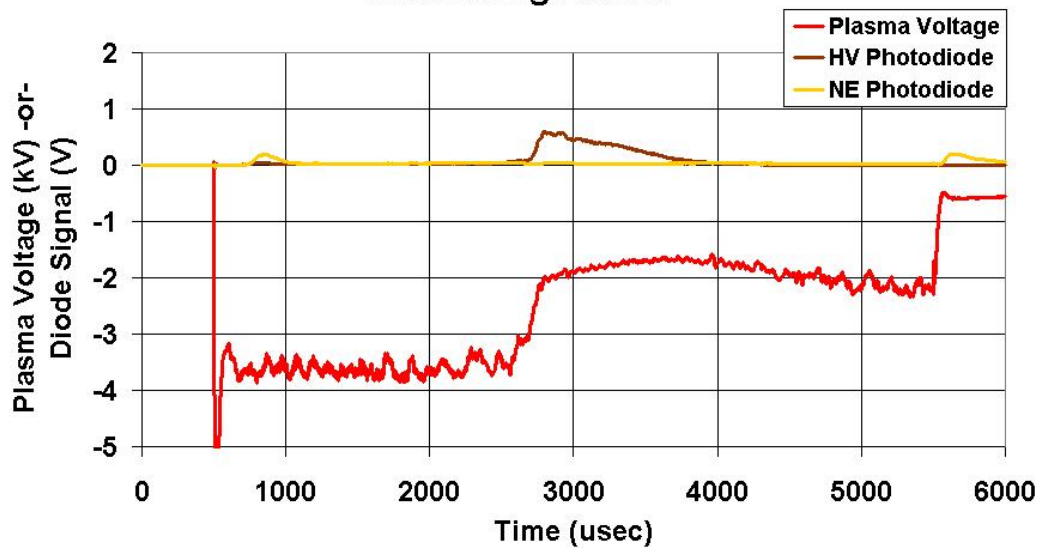


Figure 3.4: Standard MCX discharge with a transition from an H-type to an O-mode present at  $t = 2700 \mu\text{sec}$ . The activity on the HV photodiode coincident with transition subsequent lack of activity at the near end (NE) would indicate that this transitional discharge state is due to a localized phenomenon occurring at the high voltage end.

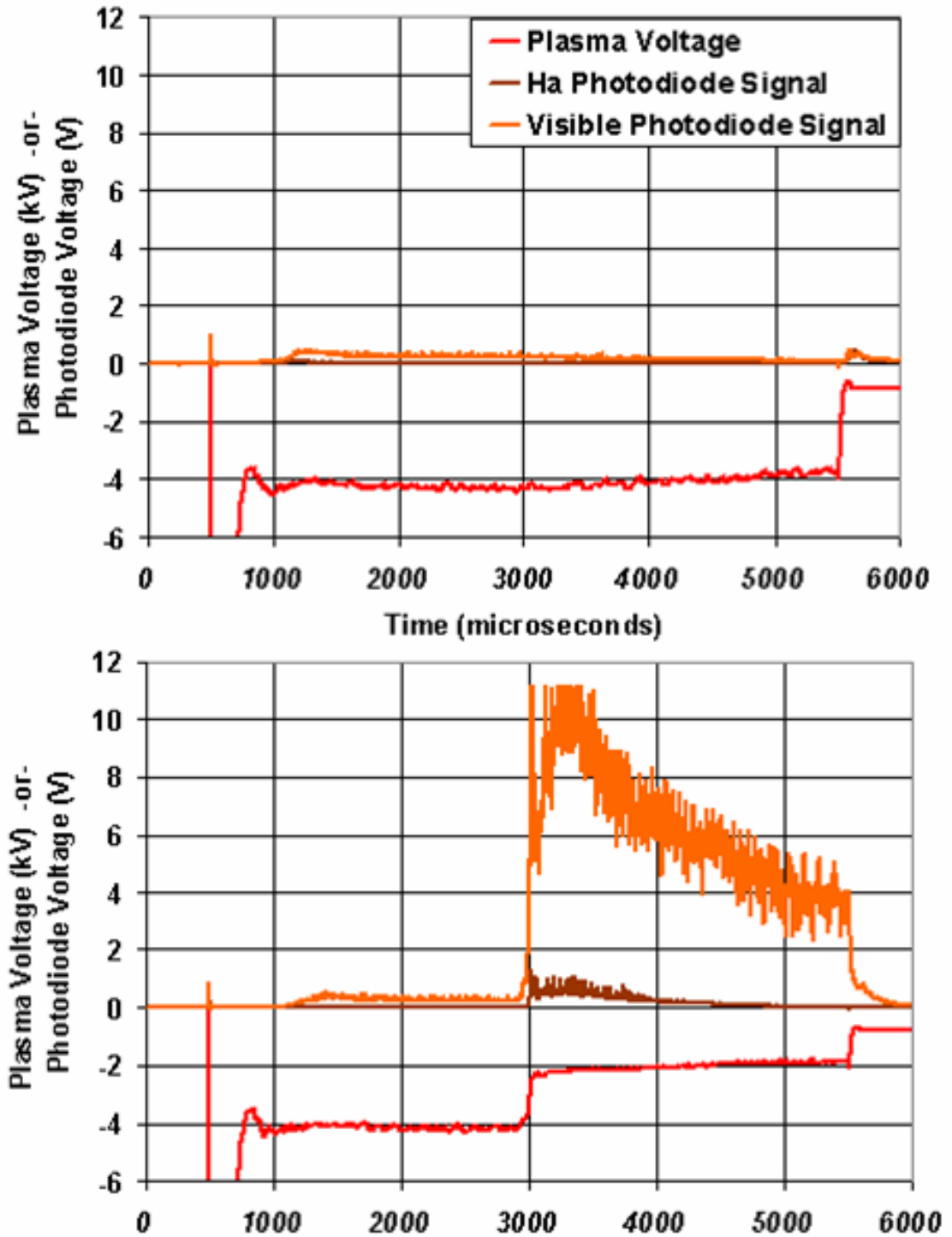


Figure 3.5: Unfiltered photodiode recording of the MCX discharge at the High Voltage(HV) end. The upper figure displays the photodiode trace recorded during a non-transitional discharge, while the lower figure displays an unfiltered photodiode trace for a discharge which undergoes a transition

through our external diagnostic. To test this hypothesis, the standard MCX 0-D circuit model (See Fig. 2.3 for the model in its most basic form) has been modified. A circuit model was created in the industry standard P-SPICE software which creates an alternate discharge path at a predetermined time after the initiation of the simulation.

This modified circuit is displayed in Fig. 3.6 and the resultant code run output in Fig. 3.7. As is shown, the plasma voltage and plasma current traces behave similarly to the actual MCX discharge. However, of interest at this point is the previously unresolved current through the volume of the discharge as denoted by the light blue current trace in Fig. 3.7. After the charging of the "plasma capacitor" and prior to the transition event, all the current flowing into the MCX system is traversing the bulk of the discharge. However, once the transition event occurs, even though the current through the full MCX system increases, actual current through the bulk of the discharge is greatly reduced. This could account for the drop in plasma measurables and also affect the accuracy of the measured quantities. For example, if we are incorrectly measuring the volume current, then the quantity  $Q/I$  is no longer an accurate representation of the momentum confinement time.

### 3.4.4 Additional Supporting Evidence

There are additional signs which point to an insulator driven occurrence as the underlying cause of the MCX modal transition. While somewhat anecdotal

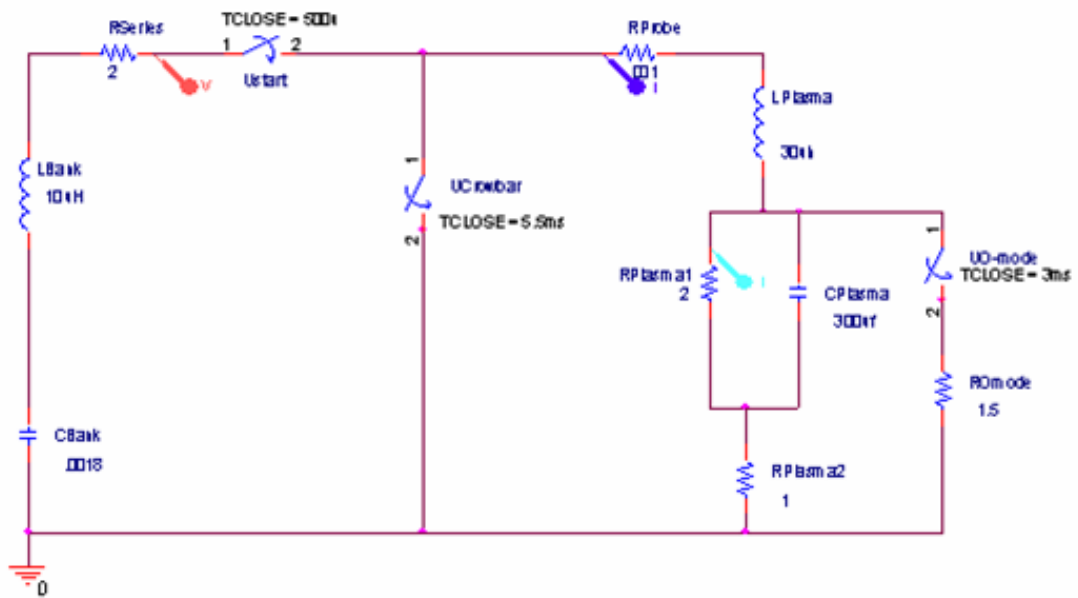


Figure 3.6: MCX circuit model, modified to include transitions. The discharge circuit now includes a second (rightmost) branch to the previously enumerated discharge model which simulates the presence of transitions. The closing of the switch (UO-mode) represents a transition initiation, which brings that resultant portion of the circuit into effect. Probes have been placed to monitor the system voltage and current as well as a probe which explicitly monitors current through the bulk volume of the rotational discharge. The traces recorded on these probes are displayed in Fig. 3.7. This final probe allows for the recovery of a measurement which is not physically possible in the actual system.

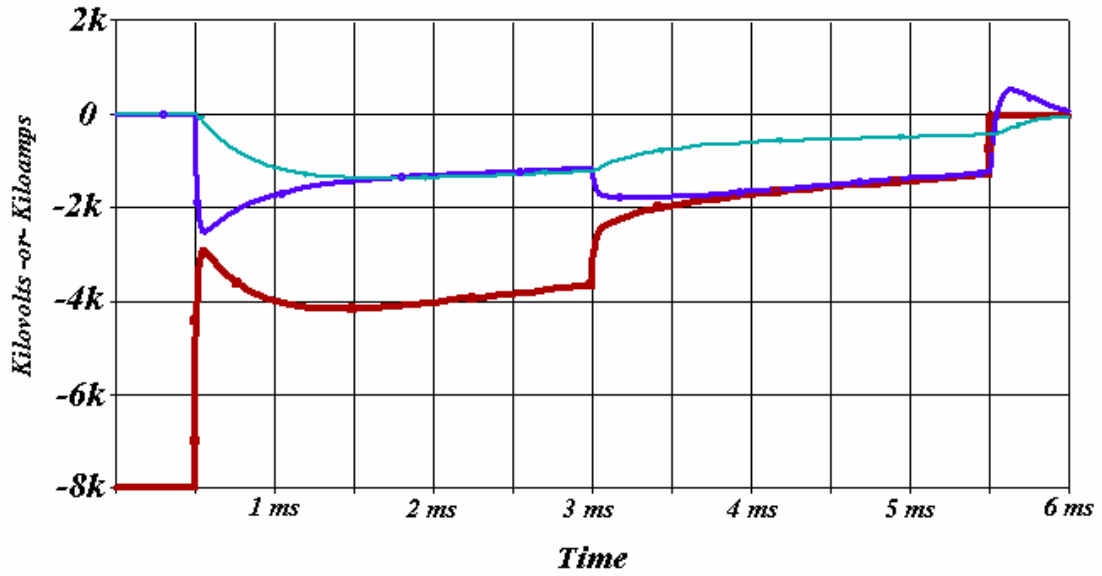


Figure 3.7: Results of the P-SPICE transitional discharge simulation. This plot displays the output results of an 6msec P-spice code run. The voltage and current traces, shown in the same color scheme as figure 3.1, are seen to undergo a typical H-O transition at 3 msec. The point to note is that even though the current through the entire discharge (dark blue) increases, the portion of the current traversing our original plasma path (light blue) has decreased drastically. This drop in actual plasma current would be consistent with a reduction in rotation velocity and attendant decrease in plasma confinement.

they, coupled with the data recovered by the various optical diagnostics present a compelling picture which points to a failure of the insulators as the cause of the O-type mode rather than any sort of tokamak equivalent pedestal collapse.

It has been noted that during shots with a strong H-O transition and a robust O type mode that there exists a strong post shot rise in pressure when utilizing high density polyethylene plasma facing surfaces. If the discharge is fully manifest in a robust H-type mode, the post shot rise in pressure is limited to a few millitorr. Explicitly, a discharge which begins at 5 mTorr will conclude at 7 mTorr. If there exists within the discharge an strong H - O transition, such that there is an extensive O-mode recorded in the time history of the discharge, then the subsequent pressure rise is recorded at 10 millitorr, if not more. Finally discharges which have been sufficiently detuned to allow access to an all O-mode type discharge show a post shot pressure rise of nearly a full order of magnitude.

While attempting to locate emission lines from discharge impurities, it has also been observed that these signals, most specifically those for the carbon type impurities are much stronger when viewed during an O-type phase. To examine this phenomenon we positioned the Ocean Optics broad band spectrometer adjacent to the High Voltage end insulators and recorded a time averaged spectrum for both transitional and non-transitional discharges. The overlay of these experiments is presented in Fig. 3.8.

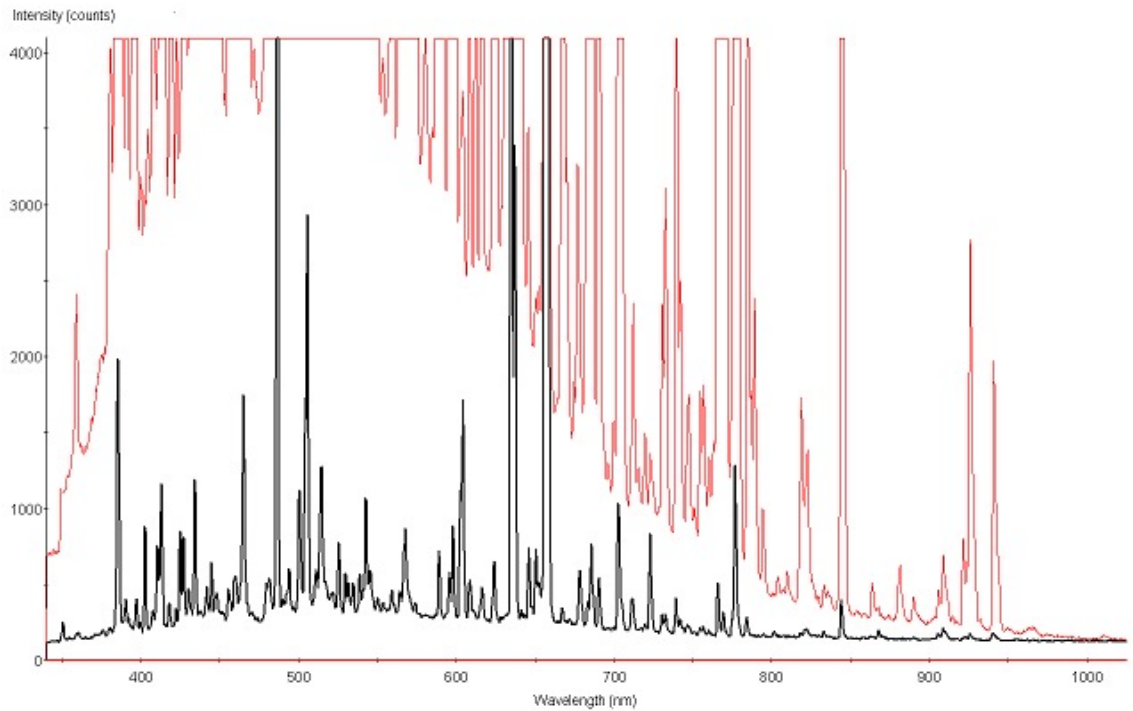


Figure 3.8: Comparison of the spectral emission recorded at the insulator face for transitional and non-transitional discharges. This figure displays the difference in emission spectra between a transition state (MCX060705-10 Red trace) and the nominal MCX H-type mode (MCX060814-16: Black Trace) as recorded on the Ocean Optics spectrometer.

### 3.4.5 Transition induced discharge limitations

The efficacy of the MCX system is dependant upon its ability to operate free from any large scale disruptions. A transition of the discharge from a desired state into one whose measurable characteristics represent a severe decrease in performance would certainly qualify as just such a disruption. It is therefore gratifying to note that the limitation presented by a transition within the discharge can be circumvented through careful choice of insulator configuration.

### 3.5 Low Voltage Mode (O-mode)

After the completion of a transition, the discharge becomes resident in an O-type mode. This mode is characterized by a lower holding voltage, slower rotation and a reduced stored energy when compared to either of the H-type modes. The discharge remains in this mode until such time as the power input is no longer sufficient to support the secondary discharge. As the O-mode is a result of the creation of an additional low impedance path to ground, attempting to disengage from this mode and return to an H-type mode by means of additional power input (boost bank) will only result in additional current through the alternate path, and not increased performance.

As a historical note, the initial rotational plasma mode discovered in MCX was christened an O-type mode [43], however it is unclear if this original mode is

indeed the same as the post transition O-mode now observed. As the initial data was recorded prior to the inclusion of the photodiodes into the diagnostic suite, the insulator burst signatures associated with transition and an O-type mode were unable to be recorded. However inspection of the momentum confinement time scalings [44] as a function of midplane field displays a degradation of return at higher magnetic field values. This may be a result an inhibited cross field diffusion through the central region resulting in an increase in internal insulator crowbaring. An experiment created to monitor surface currents across the insulator surfaces would resolve this issue.

### 3.6 Alternate Discharge Modes

The operational parameter space of the MCX discharge lies within a moderately narrow band of the total available input variable set, as displayed on Fig. 4.13. As indicated, the parameters amenable to the creation of a favorable discharge are severely limited by the discharge response to the level of power input to the system. In this section we document the resulting discharge conditions which lie outside the nominal performance zone.

If the power is below a minimum threshold, the input energy will be insufficient to offset discharge losses and the resultant plasma will not be fully ionized. If the power input is excessive, the holding voltage drops and an extreme current will be conducted, a mode similar in mannerisms to an extreme O-type mode.

### 3.6.1 Low Density Plasma Breakdown

If the capacitor bank voltage is too low, or the series resistance too high, the input power to the discharge will be insufficient to fully ionize and rotate the discharge thus resulting in a low density plasma breakdown. In this case, the input power is able to maintain a minor degree of ionization, but appears to be insufficient to offset the energy losses due to viscous damping and recombination effects. Thus there should exist a threshold input energy below which a fully ionized discharge cannot be maintained.

This minimum power theory is not a unique phenomenon to MCX and has been observed in similar rotating plasma experiments [41]. As such, efforts were undertaken to confirm these previous results on MCX.

If we assume that the presence of a current reversal during the plasma crowbar is indicative of a bulk rotational discharge, then locating the minimum input power necessary for the operation of the MCX system is reduced to a fine scan of the requisite input voltage, under constant external resistance. The results of this experiment are summarized in Fig. 3.9 and show that for a small increase in peak input power, there is a marked difference in stored charge.

For bank voltages below the minimum power threshold the discharge behavior is characteristically different. Comparing the upper I-V trace in Figure 3.9, to the standard trace shown in Figure 3.1 it is evident that the plasma voltage displays a constant increase throughout the time history of the discharge, the perturbations to

voltage trace are highly damped, and the discharge resistance is large. In addition, there is virtually no measured current reversal during the crowbar phenomenon. This final indicator, coupled with the low output light levels recorded on the photodiodes are interpreted as evidence of a lack of a robust rotational discharge.

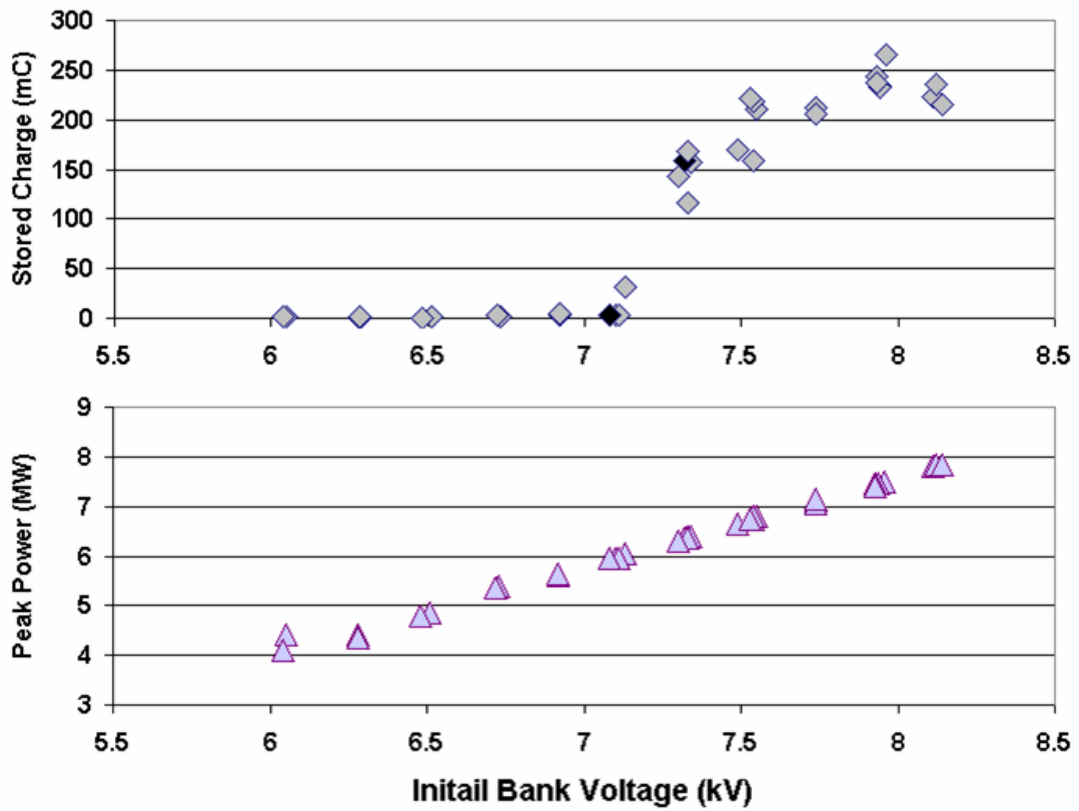


Figure 3.9: Location of the minimum input power necessary for operation of the MCX system. For a constant external series resistance ( $2 \Omega$ ), a steady rise in bank voltage leads to a commensurate increase in the peak power observed on the MCX system. This results in a manifestation of the minimum power necessary to fully ionize and rotate the discharge at this particular magnetic field (2kG). The pair of black data points shown in the upper figure denote the input conditions of the discharge traces displayed in Fig. 3.10.

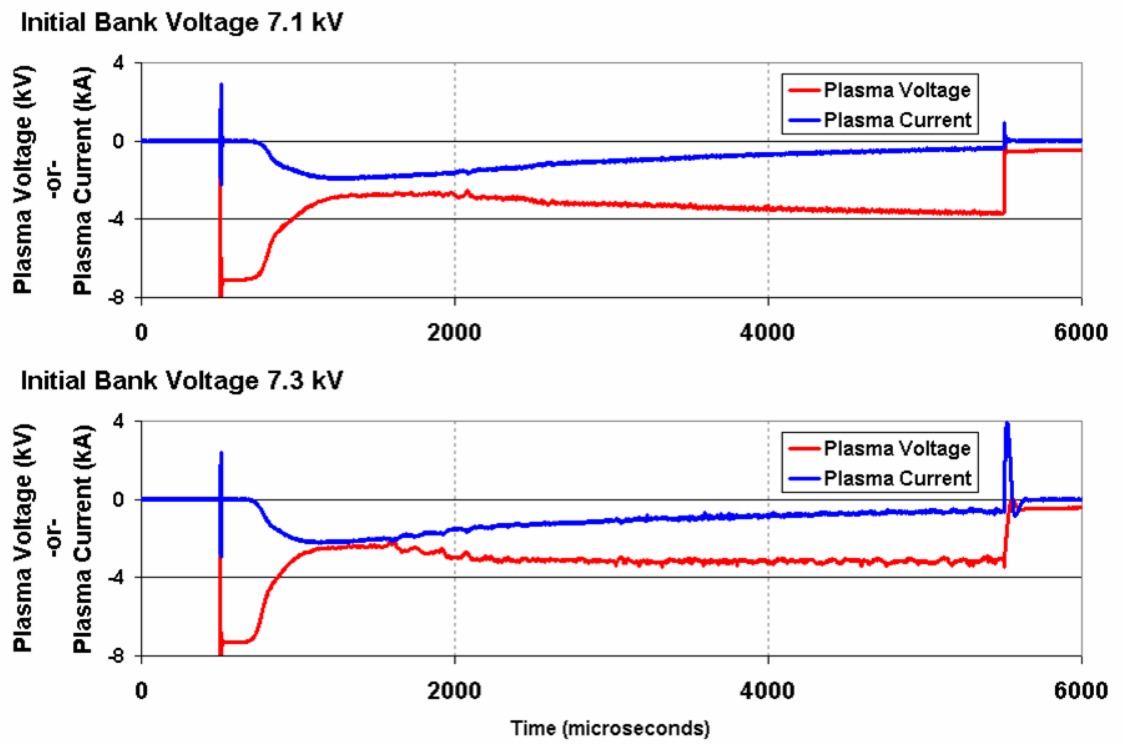


Figure 3.10: Comparison of nominal (lower trace) and low density (upper trace) discharge modes. As shown in the above graphs, for a minimal perturbation in the input power to the discharge, there are significant variations to the overall plasma behavior. This appears to be consistent with the crossing of an input power threshold.

### 3.6.2 High Current Plasma Breakdown

If the input power to the MCX system rises above a certain level, the discharge will move into a high current mode. While the transition to this mode type is not nearly as abrupt as the one noted between standard and low density modes, it is still unique enough to warrant individual classification. In the high current case, the discharge immediately becomes resident in an O-type mode, the plasma resistance drops sharply below  $1 \Omega$ , the stored charge is nearly nonexistent, and the plasma current is extreme. As such the momentum confinement time ( $\tau_M = Q/I$ ) is minuscule. For this reason, as well as the excessive damage caused to the equipment due to such large peak powers, few experiments have been conducted in this regime. Its existence is noted solely for the purpose of completing the phase map such that the high power section need no longer read “Here there be dragons”.

### 3.7 Rubric for Classification of Discharge Performance

Diagnosis of the MCX discharge performance, throughout the parametric variations undertaken in this dissertation, requires that a set of guidelines be administered to allow for comparisons to be made. We therefore explicitly state the discharge conditions which will be monitored when attempting to classify said performance, as well as the errors which will be implicit in the numbers quoted.

As the Maryland Centrifugal Experiment is first and foremost a plasma confinement device, the primary number which is monitored to determine discharge performance is the momentum confinement decay time. As demonstrated in section 2.5.4 the momentum confinement time of the MCX rotational discharge can be calculated by taking the ratio of stored charge within the plasma over discharge current at crowbar.

$$\tau_m = \frac{\int_{\text{crowbar}} I_P dt}{I_P(t = t_{\text{cb}})} = \frac{Q_P}{I_P} \quad (3.5)$$

The errors present within this measurement are twofold. The primary error source is the result of uncertainties within the calculation of  $Q_P$ . As noted previously, the modified crowbar calculation is a mathematical fit to an engineering problem, and is not without uncertainty. Primary among these is the assumption that the plasma capacitance remains relatively unaltered during the crowbar time. Also included are any errors which might be present in the calibration of the current trace. As the larger of these errors is conditionally plasma dependent, a firm number for its magnitude cannot be given, but as an estimate, we assume momentum confinement time measurements to contain an error of between 10 and 20%.

The second metric utilized for quantification of discharge performance is the calculated maximum rotational velocity. As the efficacy of the centrifugal confinement mechanism is highly dependant upon the sonic Mach number, and as we have assumed that the ion temperature remains fairly constant within the discharge pa-

parameter space, then this dependency is most easily monitored by measurement of the volume averaged rotational velocity. While it has not been practical to obtain a doppler shifted spectroscopic measurement for every discharge, benchmarking of the data has shown that dividing the maximum discharge voltage recorded after the breakdown event by the field mapped radial plasma extent and the vacuum magnetic field returns a roughly equivalent number.

$$v_{\phi,\max} = \frac{V_{P,\max}}{a_{\text{map}}B_{\text{vac}}} \quad (3.6)$$

In all the rotational velocity calculations performed within this dissertation, the radial extent of the discharge is assumed to be 20 cm unless explicitly stated otherwise. (See section 4.5 for the lone exception). Thus, in no way are we assuming a radial compression of the discharge during the H-type mode. Placed within the context of the previously described discharge modality, we are hereby assuming that all H-type modes are HV and not HR modes.

Errors within the components of this measurement (Voltage, Magnetic Field and Radial Extent) have been detailed within their relevant section, however we note here that the principle error in this case lies not with the actual experimental readings, but with the interpretation of their result. As spectroscopic measurements are only accurate to within  $\pm 20$  km/sec we have only corroborated and not confirmed the voltage based velocity measurements. In addition, we have ignored any radial profile or shearing effects. Thus the velocity measurements which are quoted

throughout this dissertation are meant only as a method of performance comparison.

The third figure of merit utilized for quantification of discharge performance is the recorded plasma resistance as calculated by  $R_P = V_P/I_P$ . This metric is utilized as increased discharge resistance is indicative of increased confinement as well as a greater discharge efficiency. However, since the plasma resistance is non-constant throughout the time history of the discharge, comparisons of this value at differing times in corresponding experimental runs would provide ambiguous results. Therefore, as many of our other measurements are recorded at the termination of the discharge, we have chosen to utilize the value of the plasma resistance at the crowbar time as the relevant performance factor.

While the components of the plasma resistance measurement are unambiguous in their errors, fluctuations within the discharge voltage and the recorded current could manifest as a nearly 50% variability within the discharge resistance. For that reason, the voltage and current traces are averaged over the final 100  $\mu\text{sec}$  prior to the crowbar, and it is the quotient of those averages which is displayed as the crowbar resistance.

## Chapter 4

### Variational Discharge Parameters and their performance effect

The performance of the MCX discharge can be modeled as a highly multi-dimensional space whereby each axis in the space is representative of a particular variational parameter. An attempt to orthogonalize the space by decoupling the parametric interconnections results in the ability to discern the effect of a particular input variable upon the overall discharge. To this end we independently perturb the major parameters, namely insulator placement and composition, background fill pressure, bank voltage, series resistance, magnetic field, and radial discharge extent and observe the discharge response. This is all performed with an eye toward the quantification of the functional dependence of the parameter's particular performance subspace as well as the enumeration of any limitations which may be encountered.

#### 4.1 Insulators

The geometry and composition of the insulating surfaces axially bounding the experimental region have been noted to have a substantial effect upon the discharge. These insulating assemblies are composed of several distinct components as shown in

Fig. 4.1. An alumina tube surrounds the high voltage stainless steel core preventing an arcing discharge from occurring in the end regions. This insulating sleeve also acts as a high voltage vacuum feed-thru for the core as it undergoes the transition into the experimental chamber. The longitudinal extent of the sleeve was originally designed to penetrate from the end flange to the magnetic field maximum, however repeated discharges resulted in structural damage throughout the length of the tubing. The end result being that the portion of the alumina cylinder located between the disk insulators and the mirror throat was explosively displaced from its original position during an experimental run and subsequently removed. At present, the plasma facing edge of the alumina tubing is nominally located 3 cm inboard of the Pyrex disks.

The Pyrex disks ensure insulator termination of the plasma carrying magnetic flux surfaces. A cuff insulator has also been added to facilitate a solid interface between the Pyrex disks and the alumina tubing. It is this cuff which has undergone the most variation and is the focus of sections 4.1.2 and 4.1.3.

Past the edge of the alumina, the core is bare through the central section of the chamber until it reaches a 2<sup>nd</sup> insulating assembly located on the far side of the alternate mirror throat. This second assembly is topologically identical to the high voltage feed through with respect to the magnetic field, however it simply encapsulates the terminus of the core rather than facilitating an exit from the vessel. While it has been noted that this results in a slight inhomogeneity with respect to the two ends of the machine, differences within the discharge at these opposing

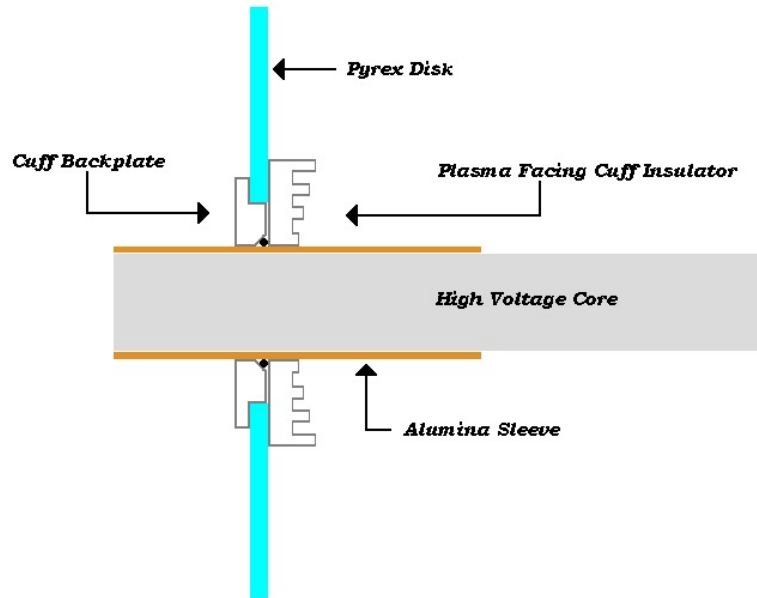


Figure 4.1: Schematic of the MCX insulating assembly. The alumina sleeve which encircles the core prevents a discharge from occurring on the left hand side of the diagram, while the Pyrex disk and attendant cuff terminate the magnetic field lines on insulating surfaces allowing a radial penetration of the electric field to occur on the right hand (plasma facing) side of the diagram

ends have been found to be minor enough that the engineering difficulties which are involved in a true symmetrization have outweighed any perceived gains up to this point.

#### 4.1.1 Disk Position and Results of position scan

To determine the effect of axial insulator placement on the discharge performance, a scan was undertaken whereby the full assemblies at each end were translated symmetrically outward with respect to along the center of the machine as denoted in Fig. 4.2. Consistent with our previously enumerated rubric, we examined the relative values of the momentum confinement time, plasma resistance, and maximum rotational velocity at each position and list the average values for these parameters in Table-4.1.

In examining these performance parameters, we are able to denote a set of qualitative patterns both about the observed changes in the values as well as the distribution of that data. From this we note that there is an slight boost in plasma performance when the insulator assembly is located just back from the mirror throat when compared to a position right at the mirror maximum. This may be due to an enhanced plasma-insulator interaction present at the first location. In such a case, particles would not be required to fully escape the mirror confinement in order to interact with the insulators, and thus a greater portion of the ion velocity space is insulator adjacent. From this peak in performance which is marginally present at

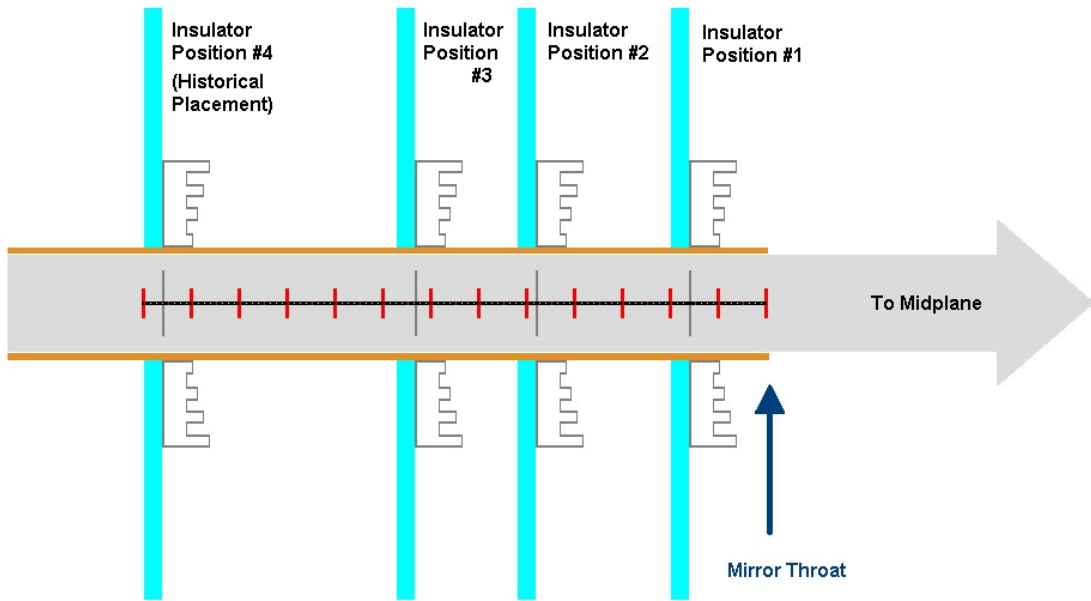


Figure 4.2: Placement of the insulating assembly during the position scan. Omitted from the diagram for reasons of clarity is placement "1a" which is 3 cm behind position 1. The distance from the grooved Macor plate to the end of the alumina tubing is a constant 3 cm. Thus the entire assembly is translated along the z axis as opposed to a relative motion of the disk insulator with respect to the alumina cylinder.

a location just behind the mirror throat, there is then a mild drop off in plasma measurables. There is also a slight increase in the spread of the data as the insulator is pulled away from the primary discharge volume. As an example of this increase in the range of the data we plot Fig. 4.3 which displays the resultant momentum confinement time as a function of insulator position.

Longitudinal Position	Z=MT	+1.25"	+3.75"	+5.75"	+11"
$v_{\phi, \max}$ (km/sec)	86	87	87	87	83
$\sigma$	1.6	2.9	3.0	4.7	3.5
Momentum Confinement time ( $\mu\text{sec}$ )	311	353	328	308	252
$\sigma$	26	42	34	45	57
Plasma Resistance ( $\Omega$ )	3.39	3.40	3.27	2.99	2.52
$\sigma$	0.30	0.31	0.23	0.16	0.42

Table 4.1: Listed are the average values for critical plasma performance parameters and standard deviations observed during a scan of insulator position. Each data point represents the average of a set of greater than 10 experiments, all of which were taken at the equivalent parameter set of between 9 and 10 kV bank voltage, 1.5 to 2 Ohms series resistance and a midplane field of 2.2 kGauss with a mirror ratio of 7.8.

This variability in the discharge could be due to the chaotic formation of a set of secondary breakdowns occurring in the non-confined regions located between the mirror throats at each end and their respective disk insulators. Any plasma which forms in this region will be accelerated by the same centrifugal forces as drive MCX, however as these minor discharge events will be driven into the insulator surface, their effect could become manifest as an instability in the overall system.

Supporting this conjecture is an observed decrease in the overall plasma resistance, perhaps indicating the presence of a mild alternate discharge path, the strength of which could influence the resultant globally averaged data.

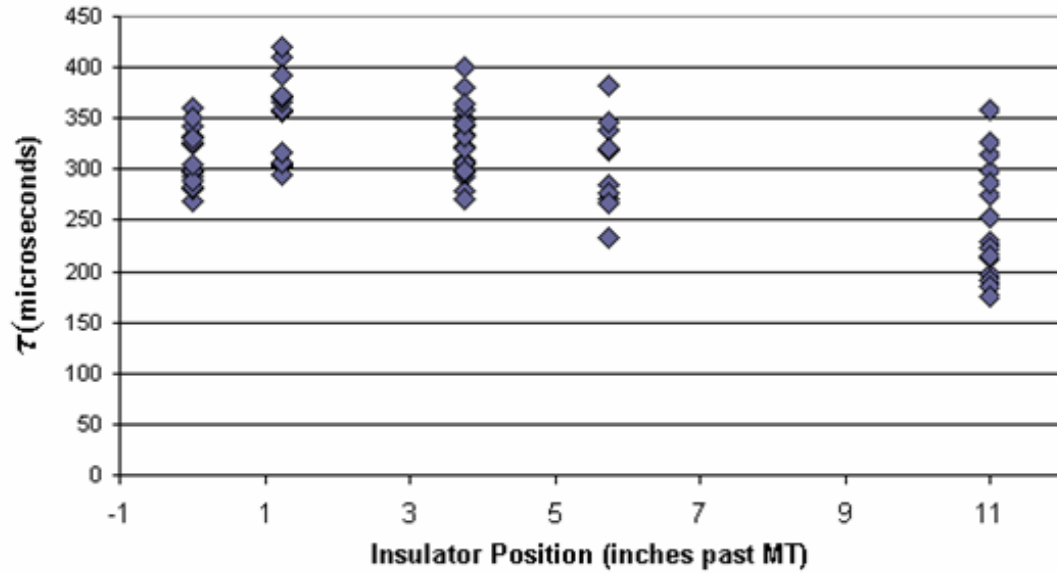


Figure 4.3: Momentum confinement time as a function of insulator position. The salient feature which we note here is that while an insulator positioned at the mirror throat shows a variation in the momentum confinement time of roughly  $100 \mu\text{sec}$ , for a similar set of input parameters, experiments undertaken at mirror throat + 11" show a resultant variation of almost  $200 \mu\text{sec}$ .

There is also the wholly unambiguous data point of discharge transition probability. For the insulator positions close to the mirror throat (positions 1 - 3 in figure 4.2), there is little to no evidence of the strong H-O transitions which are consistently evident at MT+11" (historical placement). This lack of transitions at the

closer locations is consistent with a reduction in the volume of unconfined regions as well as an increase in the strength of the magnetic field at the insulating surfaces.

Therefore, we conclude that for minor variations (again referring to positions 1, 1a and 2 in figure 4.2), the insulator placement has a minimal effect upon discharge performance. However as this effect is cumulative, performance losses could become pronounced as the assemblies are distanced from the magnetic maximum.

#### 4.1.2 Ceramic Plasma Facing Components (MACOR)

As shown in Fig. 4.1, the alumina tube does not mate directly with the Pyrex disks. The inability to create a tight seal at this point necessitated the addition of an insulating cuff which could create a compression seal around the alumina cylinder, thus preventing an arcing breakdown from forming along this surface. As of this writing, there have been two separate materials which have been utilized to create this aforementioned cuff insulator, namely high density polyethylene, as well as the machinable ceramic MACOR. Although historically not the first insulator attempted, we begin the discussion by documenting the performance features of the MACOR insulating cuff. As all of the insulator composition experiments were performed at a MT+11" axial position, we adopt the final column of Table-4.1 for utilization in comparisons here.

As shown in the earlier diagram (Fig 4-1), the MACOR cuff insulator has been implemented with a grooved surface geometry. It was this configuration of

insulating assembly which was held constant through the position scan described in the previous section. The grooving of the MACOR was performed in an attempt to increase the distance that a surface breakdown must traverse in its path from core to vessel wall thus decreasing the likelihood of such an event. That being said, there do exist some material based physical limitations that mitigate this attempt to extend the breakdown path length. Note that these limitations are material specific and more a set of guidelines than hard rules, however as they address the structural stability of the piece, violations will result in a reduced piece lifetime.

The maximum path extension allowable for a set of grooves machined into a MACOR blank is derived from the consideration that physically the machinable ceramic is quite brittle. Thus when creating a groove, the material will only comfortably support a groove depth which is twice the groove width. If the width of both the positive and negative portions of the groove is  $d$  (giving a total length  $L = n \cdot 2d$ ) and the depth is  $2d$  then the total path ( $P$ ) covered is

$$P = n(d + 2d + d + 2d) = 6nd = 3L \quad (4.1)$$

The stepped grooves which are depicted in the earlier figure effectively double the path length along the MACOR, and were adopted as a test of the material. As evidenced by the extensive damage on the alumina tubing, the MCX discharge is stressful on insulating surfaces. Thus creating a series of increasing grooves allowed for some quantification of the material's ability to withstand these forces. Exam-

ination of the piece after several hundred discharge events revealed no structural weakness in any of the grooves.

To determine the effect of an increased path length, these grooved insulator experiments are compared to a set of control shots undertaken with a flat MACOR plate affixed overtop the grooves. Table-4.2 displays the results of a comparison between grooved and flat MACOR substrates. As noted in the table, the only truly noticeable effect that the grooving of the insulator appears to have had is in the mitigation of a transitional discharge state. This is supportive of the “transitions as insulator breakdown” theory postulated in section 3.4. Other than this observation, it does not appear that a factor of 2 increase in path length will summarily boost the primary discharge by a commensurate amount.

Insulator Type	Grooved	Flat
Maximum Rotational Velocity (km/sec)	80	80
$\sigma$	3.7	2.1
Momentum confinement time ( $\mu\text{sec}$ )	247	224
$\sigma$	60	73
Plasma Resistance ( $\Omega$ )	2.96	2.61
$\sigma$	0.56	0.57
Transition Probability	60%	90%

Table 4.2: Comparison of grooved and flat MACOR cuffs for a series of approximately 20 shots each with attendant standard deviation. This data was taken under an identical parameter set for both insulators. The only appreciable difference between the two systems appears to be the probability with which a shot will transition

### 4.1.3 Polymer based Plasma Facing Components (HDPE)

Historically, the cuffs utilized to anchor the Pyrex disks to the alumina cylinders were constructed out of high density polyethylene ( $C_2H_4$ ). These cuffs were abandoned after approximately a year and a half of experiments when an examination of the interior surface of the vacuum vessel displayed macroscopic carbon deposits. These deposits were centralized about the insulator assemblies and propagated into the midplane of the vessel with decreasing density. At their thickest, these carbon layers had accrued enough mass to become reminiscent of a polymer film, and were able to be flaked off of the vessel wall.

Very recently however, we have returned to polyethylene plasma facing surfaces in an attempt to return to the HR mode described in section 3.3.1. This return was effected, not by wholesale replacement of the insulator assembly, but by replacing the previously detailed flat Macor inserts with equivalent polyethylene pieces.

The preliminary data taken with these plastic plasma facing disks shows no statistical difference in the discharge voltage, however there does seem to be a slight increase in the reversal charge. This increase could be a result of an uptick in density due to the now persistent occurrence of H-O transitions and attendant post shot pressure rise observed with polyethylene insulators.

Possibly relevant to the examination of the insulator's role in the transition phenomenon is the observation that the transitions incurred while the insulator is composed of polyethylene were much more abrupt ( $< 80 \mu\text{sec}$ ) than the transitions

which were noted with the Macor endplates ( $> 300 \mu\text{sec}$ ). This may be due to the comparatively lower melting point of the plastic insert, which creates a faster impurity bloom allowing for enhanced collisions at the endplates and thus resulting in a greater cross field conductivity.

A concern that should also be raised at this point is the extent to which the content of our background gas is influenced by the ablation of the high density polyethylene cuff. If one were to assume a standard H-O transitioning shot with an attendant nominal pressure rise from 5mTorr to 10mTorr, one could surmise that the resultant increase in fill pressure is the result of a monolayer vaporization of the polyethylene insulator. This supposition is supported by the lack of a comparable pressure increase under identical conditions with a MACOR insulator.

If that is the case, and we make the simplifying assumption that the carbon from the polyethylene ( $\text{C}_2\text{H}_4$ ) cuff remains fully in suspension during the discharge, we arrive at a background gas fill which is 8.3 mTorr hydrogen and 1.6 mTorr carbon. This results in a plasma which is 16% carbon by volume but is 70% carbon by mass. This would affect any calculations where the dominant species mass is assumed. That being said, as it appears that this post shot rise in pressure is dependent upon the existence of a transition and proportional to the strength of the resultant O-mode, one could conclude that the impurity bloom does not occur until the transition and as such any measurements recorded pre-transition could still be assumed to be hydrogen dominant.

#### 4.1.4 MYLAR end wrap

An attempt to block secondary discharge formation at the insulators was undertaken by covering the interior vessel walls in the regions near the insulating assemblies with a high voltage insulating thermoplastic film (MYLAR). The MYLAR was wrapped fully around the inner circumference of the vacuum vessel and extended from the end flanges, past the insulating assemblies and terminated approximately 7" inboard of the mirror throat, resulting in a full axial extent of 36" on both the near and high voltage ends. It should be noted here that while this excursion into the active plasma region is large, it is not sufficient to reach the outer last good flux surface which bounds the main discharge. In addition, even though the outgassing from this material was significant, we were still able to achieve a nominal base pressure of  $5 \times 10^{-5}$  torr. This is 1% of the standard discharge backfill pressure and as such we were able to accomplish a set of reliable experiments.

Results from this test showed that while the presence of the MYLAR was able to mitigate the occurrence of H-O transitions, it did not appear to effect the holding voltage of the discharge during the H-mode. Tempering this conclusion is the observation that the physical damage pattern present on the disk insulator assemblies only extends out to a radius consistent with a field line mapping of the last good flux surface. This would suggest that any discharge present on the surface would traverse the insulator only until such time as it reached this terminal flux surface. It would then preferentially choose the magnetic field line as a current

path, thereby completing the circuit to ground. If this were the case, it would suggest that the MYLAR test, as implemented, was not completely successful in eliminating these alternate current paths.

## 4.2 Effects of variational Fill Pressure

The background hydrogen fill pressure in which the MCX discharge is ignited has been scaled through 2 orders of magnitude centered about our nominal fill value. This results in a data set ranging from 0.5 mTorr to 50 mTorr inclusively. We will deviate from our standard performance metric slightly by noting that there exist qualitative as well as quantitative results of differential pressure operation. The first part of this section details the results of this pressure scan, outlining the major features noted in each regime by highlighting their variations from the standard performance conditions. The subsequent portions are then left to denote the experimental consequences of these particular pressure choices. For example, operation at a reduced pressure will require a larger initial voltage in order to ionize the background neutral gas. This reduces the range over which an input voltage parameter scan can be accomplished.

### 4.2.1 Discharge Performance

We begin with a discussion on the variations in overall global plasma behavior which have been observed throughout this scan. These variations are most easily

observable by monitoring the behavior of the plasma voltage diagnostic as shown in Fig. 4.4. Unfortunately, magnetic and interferometric diagnostics were offline during the course of this experimental run, so we are constrained to the realm of speculation when attempting to explain the observed tendencies.

We assert that the unstable behavior which seems to occur at the higher fill pressures is due to an incomplete ionization of the background neutral gas. This conclusion is supported by a calculation of the plasma density. The plasma capacitance  $C_P$  as calculated from the stored charge recorded during the crowbar equals

$$C_P = \frac{Q_P}{V_P} = \epsilon_R C_0 \quad (4.2)$$

where  $C_0$  is the vacuum capacitance and the dielectric constant( $\epsilon_R$ ) of the MCX discharge has been confirmed to be [48]

$$\epsilon_R = 1 + \frac{\mu_0 \rho c^2}{B^2} \text{ where } \rho = n M_i \quad (4.3)$$

This leads to a density calculated from the stored charge and plasma voltage at the crowbar of

$$n = \left[ \frac{Q_P}{V_P C_0} - 1 \right] \frac{B^2}{\mu_0 M_i c^2} \quad (4.4)$$

The results of this scan, displayed in Fig. 4.5 show that while a lowering of the fill

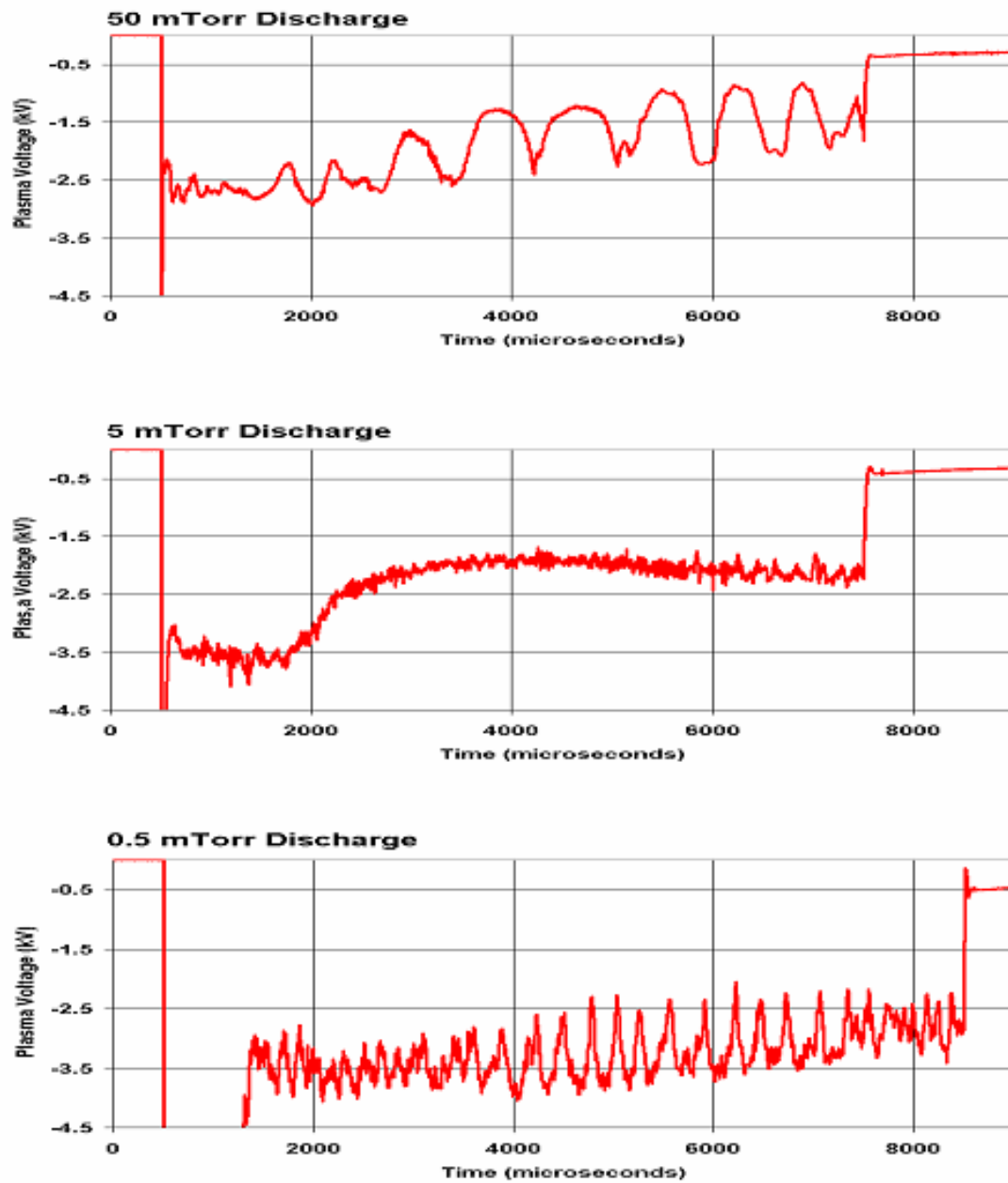


Figure 4.4: Qualitative comparison of discharge behaviors. This figure displays the differences in discharge behavior observed at alternate fill pressures. Most notably the large periodic structures in the top and bottom graphs would seem to be indicative of overall instabilities. In all cases, termination of the voltage signal is due to an externally imposed crowbar.

pressure will result in a depressed density, an increase in the fill pressure does not result in a commensurate density rise. This conclusion is supported by the increased level of the  $H_\alpha$  photodiode signal recorded at the higher fill pressures as shown in Fig. 4.6.

The data recorded within this scan also supports the assertion that, for a nominal 5 mTorr background fill, the MCX discharge is fully ionized. A check of this can be undertaken by assuming that for a fully ionized discharge, charge exchange is the dominant loss mechanism such that for a charge exchange cross section ( $\sigma_{cx}$ ), the momentum confinement time ( $\tau_m$ ) is

$$\frac{1}{\tau_m} = \frac{I_P}{Q_P} \sim \frac{1}{\tau_{cx}} = n_0 \sigma_{cx} \sqrt{v_{T_i}^2 + v_\phi^2} \quad (4.5)$$

and the neutral density ( $n_0$ ) is therefore

$$\begin{aligned} n_0 &\cong \frac{I_P}{Q_P} \frac{1}{\sigma_{cx}} \frac{aB}{V_P} \frac{M_s}{\sqrt{1 + M_s^2}} \\ &\cong \frac{aB}{\sigma_{cx} Q_P R_P} \frac{M_s}{\sqrt{1 + M_s^2}} \end{aligned} \quad (4.6)$$

If we assume  $\sigma_{cx} = 4 \times 10^{-19} \text{ m}^2$  [27, p. 157] for a mildly supersonic discharge ( $M_S \sim 1.5$ ) then the average neutral density calculated for the 5 mTorr shots recorded in Fig. 4.5 is  $n_0 \sim 3 \times 10^{17} \text{ m}^{-3}$  which is significantly less than 1% of the ion density.

Moving from elevated to depressed densities we note the erratic behavior of the bottom voltage trace in Fig 4.4 which corresponds to a lowered fill pressure. While we are again unable to present any experimental data for the following hypothesis, there have been observations [39] that below a certain critical density the volume discharge becomes permeable to full neutral penetration. This neutral penetration could be responsible for the periodic irregularities observed at these low discharge pressures and could be monitored by the newly installed multichord photodiode array.

Fill Pressure	0.5 mTorr	5 mTorr	50 mTorr
Maximum Rotational Velocity (km/sec)	94	87	68
$\sigma$	3.2	3.0	6.5
Momentum confinement time ( $\mu\text{sec}$ )	39	148	102
$\sigma$	20	30	56
Plasma Resistance ( $\Omega$ )	3.12	2.07	1.36
$\sigma$	0.65	0.46	0.51

Table 4.3: Critical discharge parameters at altered fill pressures. This table lists the average values of critical parameters at various fill pressures as well as the standard deviations. Each average value is representative of a data set of greater than 10 identical individual experiments.

We move now to a set of qualitative discharge comparisons, as summarized in Table-4.3. Within our previously enumerated set of discharge guidelines we discern that for the discharge experiments which MCX wishes to conduct, the 5 mTorr pressure range appears to be optimal. While we note mildly elevated rotational

velocities at reduced pressures, these have been calculated from a maximum recorded voltage signal and therefore may be due more to the large amplitude modulation of the voltage signal than any true boost in performance.

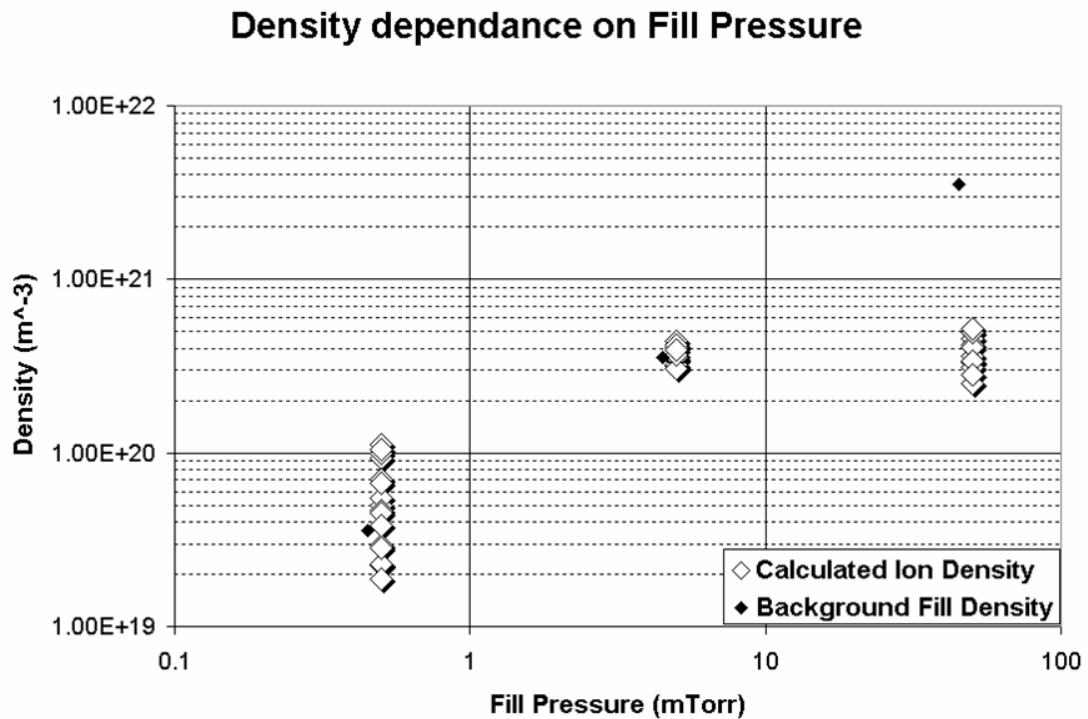


Figure 4.5: Density dependence on fill pressure. The above figure shows the calculated plasma density for the 0.5, 5, and 50 mTorr pressure regimes (open diamonds) as compared to the density derived from a fully ionized background fill gas (closed diamonds). The observation to be noted here is that an increased fill pressure above nominal values does not induce an increased discharge density. We therefore conclude that an elevated neutral density is resultant from the elevated backfill pressure.

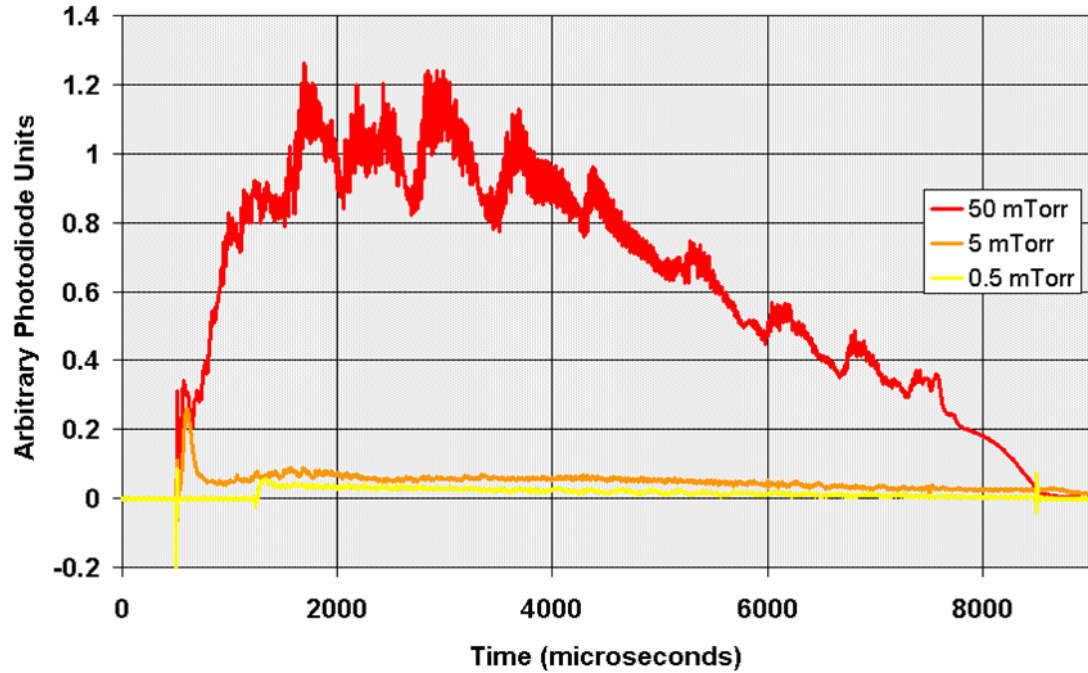


Figure 4.6: Increased neutral signal evident at elevated fill pressures. The above figure displays the  $H_{\alpha}$  photoemission signal recorded at the MCX discharge midplane for variational pressure regimes. The order of magnitude increase in recorded signal for the 50 mTorr reading is consistent with a corresponding neutral density increase. Thus providing an independent confirmation of the results displayed in Fig. 4.5

## 4.2.2 Effects of insulator composition on the ability to operate at reduced fill pressures

It should be noted that all shots in this section have been undertaken while utilizing the MACOR cuff insulators. This is due to the propensity of the polyethylene insulators to ablate a monolayer of material during the discharge and thus increase the effective fill pressure. While we are presently unable to temporally resolve the increase in fill pressure, it has been noted that there is a momentary post shot rise in the pressure displayed on the capacitance manometer gauge. This rise in pressure is transient, lasting only a few seconds, as the turbopump continues to evacuate the chamber, however by monitoring the post-shot pressure peak we have been able to draw some rough conclusions. These observations are noted in section 4.1.3, suffice it to say that at this point the accessibility of the low density discharge state is firmly mitigated by the presence of the high density polyethylene plasma facing surfaces.

## 4.2.3 Static Pressure Fill Tests

Given the radical pressure increase seen under dynamic conditions with the polyethylene insulator cuffs, one may be concerned about the ability to operate the MCX discharge at a reduced fill pressure irrespective of the insulator configuration. To that end, a series of experiments was undertaken with the MACOR insert whereby the nominal dynamic fill conditions were abandoned in favor of a static gas fill. This allowed for a greater quantification of any post shot impurity bloom, as

well as the ability to monitor any conditioning effect which may be experienced due to repeated runs at a reduced fill pressure.

The dynamic fill conditions which are nominally employed on MCX are the result of a continual evacuation of the chamber by an LH1000 Turbomolecular pump offset by a constant influx of neutral hydrogen gas as regulated by a micrometer fill valve. This results in a constant backfill pressure of 5 millitorr. As the nominal pumping rate of  $1 \times 10^3$  cubic centimeters per millisecond (1000 L/sec in more relevant units) is small when compared to our  $8 \times 10^5$  cubic centimeter internal volume we have heretofore assumed that these conditions approximate a roughly static volume throughout the duration of a discharge. However, this rate is large enough to effect pressure measurements which are resolved on a multi-second rather than a millisecond timescale. Thus we have adjusted our fill technique for this particular set of experiments.

The gate valve which connects the turbopump to the experimental chamber was closed, effectively sealing off the discharge volume. Then the interior pressure was slowly increased by means of the gas fill valve until the desired reading was accomplished, at which point the gas valve was also closed. We then monitored the pressure reading over the course of 15 minutes to determine the baseline pressure drift. Over the course of this observation, an initial pressure of 4.97 mTorr was noted to rise to 4.99 mTorr. This was judged to be small enough that we could assert with reasonable confidence that any variation in the reading after a discharge was in fact due to the discharge itself.

Experiments performed with the MACOR cuffs under these static fill conditions at a standard pressure of 5 mTorr displayed none of the post shot bloom effects which are common to the polyethylene. In fact, shots taken at these conditions showed a mild ( $\sim 0.3$  mTorr) drop in the post shot pressure, possibly due to gas absorption at the bounding surfaces.

These observations about the pressure response of the MACOR led to the conclusion that it was now possible to attempt the low pressure shots which have been detailed at the beginning of this section with a confidence that we were able to remain in the depressed pressure regime throughout the entire discharge. This stands contrary to previous static fill attempts conducted with a HDPE cuff whereby a 500  $\mu$ Torr initial pressure had become a 9500  $\mu$ Torr pressure by the termination of the discharge. (The shot referenced here is MCX051005-3, singularly included into the MCX06 data set for this comparison).

To create the operational conditions enumerated in the low pressure section, a set of conditioning experiments needed to be performed. These experiments were enacted under static fill conditions with a 130  $\mu$ Torr backfill. Post discharge pressure was recorded and then the chamber evacuated and re-set for the next discharge. The results of these discharge cleanings are displayed in Fig. 4.7 and show a definitive conditioning effect. After these conditioning shots were taken, a set of static fill discharges were attempted at 500  $\mu$ Torr to test the efficiency of the method. This

baseline conditioning test was performed each day that low pressure experiments were undertaken and in all cases the post shot pressure rise noted for these static fill tests was less than  $50 \mu\text{Torr}$ .

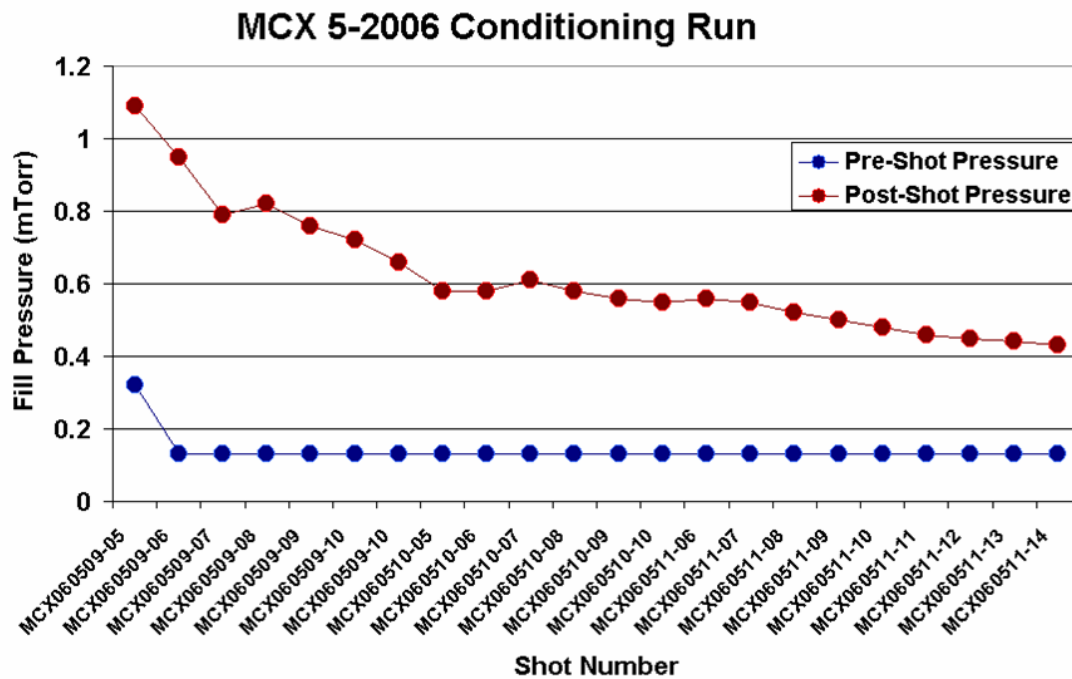


Figure 4.7: Results of MCX conditioning run. The lower line represents the background fill pressure of the experimental vessel before a discharge was attempted. The upper line displays the corresponding rise in pressure resultant from the discharge. The merging of the two lines gives confidence that discharges attempted at depressed pressures will remain in this lower pressure regime throughout the experimental run.

#### 4.2.4 Effect of fill pressure on discharge diagnostics and parameter range

While the variation of the discharge itself with respect to adjustments in the fill pressure is of primary importance, there were noted effects upon the diagnostics implemented in MCX. As detailed in section 3.2.1, MCX utilizes its crossed field geometry not only for a bulk plasma rotation, but also for its initial ionization. Therefore, until such a time as there is implemented an alternate ionization source, the ability of MCX to operate at reduced pressures is limited by its ability to achieve a breakdown at those pressures.

This of course falls under our primary class of limitations, namely those which can be easily surmounted through engineering solutions. An increase in the available bank voltage or the construction of an alternate ionization source would certainly allow for a subsequent expansion of the accessible pressure regime.

However, increasing the accessibility of the reduced pressure regime will not alter the effects that these type discharges have upon the employed diagnostics. The two systems most affected by the adjustment in fill pressure are the spectrometer and the discharge current diagnostics.

When compared to a discharge undertaken with standard conditions, the current diagnostic, and most specifically the current reversal, is no longer a reliable measurement at lower densities. The utilization of the current reversal as a measure

of stored energy within the discharge is based upon the assumption that the value of the “plasma capacitor” does not vary greatly during the limited time in which the reversal is measured. The smaller inherent densities seen at reduced pressures result in a reduced capacitance and as such the resultant decay of the plasma is faster than the RC time of the reversal, resulting in an undervalued stored charge.

Standing contrary to this however, is a noted increase in the sensitivity of the spectrometer. While the strength of the impurity lines regularly recorded on the spectrometer does not notably decrease with a reduced fill pressure, the broadband radiation which acts as a noise floor for the signal appears highly dependant upon this parameter and is proportionally reduced. Thus, while the overall strength of the true signal is unchanged, the signal to noise ratio increases by nearly a factor of 2, allowing for a clearer identification of the spectral emission lines as well as the ability to resolve lines which may have previously been obscured by this noise floor.

### 4.3 Magnetic Field Variance

Adjustments to the applied magnetic field can take two separate, if not uncoupled forms. The primary number of merit when discussing the magnetic field is the value of the field at the longitudinal center of the vessel, also termed the midplane magnetic field. It is this field which, more than any other parameter, appears to determine the value of the holding voltage of the discharge. This dependence upon the midplane field is explored and a possible link between magnetic field and plasma

voltage is discussed.

The second relevant parameter to note is the quotient of the magnetic field at the mirror throat over the midplane magnetic field, a number recognized as the mirror ratio ( $R_M$ ). The coupling between these numbers is a result of the limitations on available current through the electromagnets as dictated by the Eratron power supply. The MCX system is field limited at the magnetic mirrors to a value of 1.8 Tesla, therefore the maximum midplane field for a given mirror ratio is the ratio of the mirror field over the mirror ratio. In essence, the larger one wishes the mirror ratio, the smaller the available maximum midplane field.

### 4.3.1 Field Strength

Adjustments to the midplane magnetic field have resulted in a linear scaling in the discharge voltage as evidenced by Fig. 4.8. Increasing the magnetic field by nearly a factor of 2 results in an increase in discharge voltage by a commensurate amount. As  $v_\phi = V_P/aB$ , this type of scaling could be consistent with the observation of a constant rotational velocity. A possible causal relationship resulting in just such a scaling has been determined and is explored in Chapter 6.

In looking to our other discharge signposts to determine experimental performance we observe an increase in plasma resistance at higher midplane fields. For the following values, the second number is representative of the standard deviation

for a set of greater than 10 data runs, and not the true experimental error.

$$R_{B=2.2 \text{ kG}} = 1.7 \pm 0.05 \Omega$$

$$R_{B=3.84 \text{ kG}} = 2.4 \pm 0.02 \Omega$$

This could be indicative of a decreased cross field diffusion consistent with a Bohm type diffusion term proportional to [16, p. 190]

$$D_B = \frac{1}{16} \frac{T_e}{B} \frac{\text{m}^2}{\text{s}} \quad (4.7)$$

The conclusions that  $V \propto 1/B$  and  $R \propto 1/B$  results in a discharge current which is very nearly constant throughout the magnetic field scan. Unfortunately, due to crowbar ignitron failure at elevated voltages, we were unable to record a full range of current reversals during this midplane field scan and so are unable to make any claims as to the possible momentum confinement scalings at this point.

### 4.3.2 Mirror Ratio

Discharge performance has been shown [44] to scale positively up to a mirror ratio of approximately 7. Beyond this point there then appeared to be a leveling off, possibly due to geometric issues concerning a varying location of the outer terminal flux surface. A possible explanation, which appears to be commensurate with the Critical Ionization Velocity plasma limiting model, is discussed in Chapter 5.

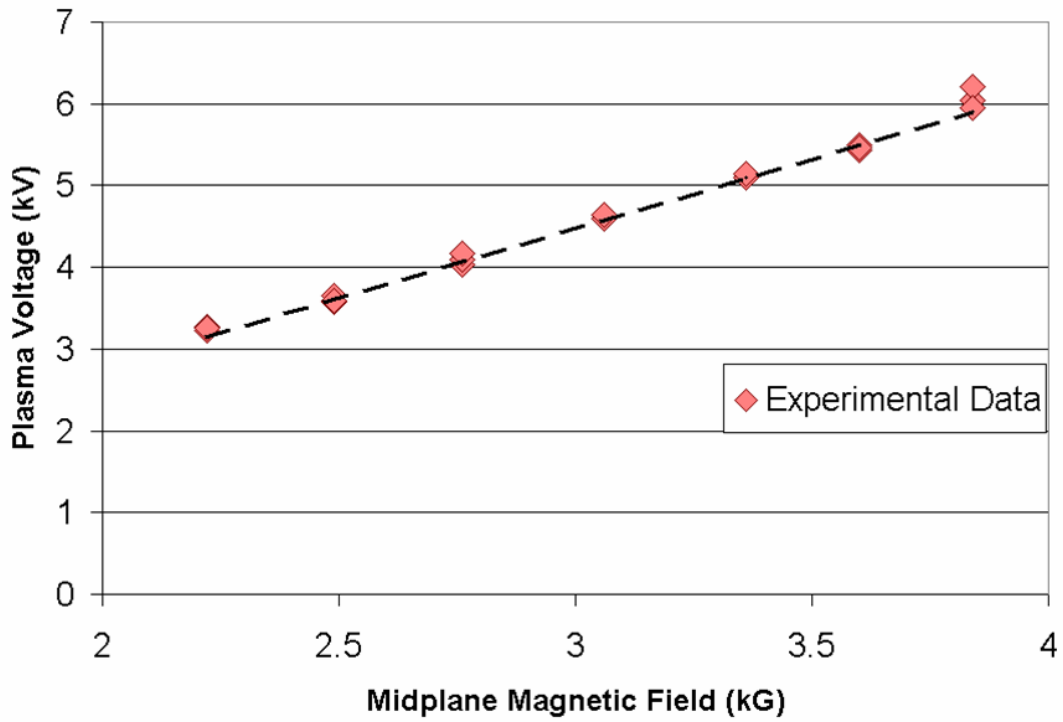


Figure 4.8: Dependence of plasma voltage on midplane magnetic field for a fixed mirror ratio. The large data points represent a set of maximum recorded plasma voltages for the particular midplane magnetic field at a constant mirror ratio of 4.4. We note that there are at least three distinct data points for each magnetic field value, however the shot to shot repeatability for this particular parameter scaling results in an overlap, in addition the error bars are covered by the data points. The dashed line represents is a plot of the equation  $V_P = v_\phi a (B_{mid} - 0.3)$  for a constant  $v_\phi = 85$  km/sec with an  $x$  offset of  $+0.300$  G. Justification of this model can be found in Chapter 5.1

## 4.4 Input Power Circuit Variables

As denoted in chapter three, the Maryland Centrifugal Experiment is a pulsed system whose discharge is powered by a set of dielectric capacitors. These capacitors provide the ionization energy necessary to initiate the discharge, the electrostatic potential necessary to induce bulk rotation, and the radial current necessary to offset viscous losses. They are also among the simplest of the parameters to vary. An alteration to the voltage present on the capacitor bank at the initiation of the discharge can be accomplished by adjustment of the settings on the charging power supply. In addition, an alteration to the size of the discharge bank, is also not a complicated task.

Included in this discussion of the input power variables is the current limiting series resistor. This component, as described in section 2.2.3 limits the available current as well as reducing the available bank voltage across the plasma, thus placing restrictions on the available input power. Also designed to allow for rapid variation, the resistor has been engineered so as to allow value alterations of this discharge parameter to be fully completed within the 5 minute quiescent period between experimental runs.

We have therefore, by design, been able to determine the effect of a variation in these initial parameters within a great many of the MCX performance subspaces. Experiments conducted at alternate magnetic fields, alternate fill pressures, and alternate radial extents have all been accomplished by an initial adjustment of the

primary parameters ( $B$  (kGauss),  $p$  (mTorr),  $a$  (m)) followed by a secondary scan of the bank voltage so as to better determine the requisite performance effect congruent with the subspace. Such a comparison is possible due to the robust behavior of the discharge under variations of both the bank voltage and series resistance, thereby allowing any deviations within the discharge to be attributed to the primary parametric adjustment. The experiments denoted within this section are the nominal exemplifiers which display the standard observed behavior over these secondary value scalings.

#### 4.4.1 Capacitor Bank Size

The majority of the experiments within the data set covered by this dissertation have been accomplished on a single 30 unit capacitor bank with a total capacitance of 1.8 mF. For a nominal series resistance of 2 ohms and assuming a roughly 2 ohm “plasma resistance” the decay time of the capacitor bank is then  $\tau_B = 7.2$  msec. This value is substantially longer than the nominal 300  $\mu$ sec momentum confinement time of the discharge, and as such the capacitor bank can be treated as a quasistatic input parameter. That being said, it is still possible that the variation of this parameter could have some unforeseen effect.

As described in section 2.2, the MCX capacitor bank is divided into two equal subsections, each containing 30 capacitors, and each with its own dedicated series resistance. This design was adopted so as to allow independent operation of the

smaller banks, permitting a greater flexibility. Primary among its intended uses was the ability to trigger a second bank at a time substantially after the formation of the discharge so as to 'boost' the plasma into an elevated state. Few of these experiments have been conducted, and as the results are exceedingly preliminary, they will not be reported here. Instead we confine this discussion to the particular case whereby both banks are triggered simultaneously, thus behaving as a single larger capacitor bank. We note again that in the following discussion, the value quoted for the external resistance is the equivalent resistance generated by a parallel combination of the physical resistances attached to bank 1 and bank 2.

As expected, we found very little difference in the plasma measurables for discharge times which were small when compared to the bank decay time. In addition to quantities within the previously enumerated rubric, spectroscopically measured doppler shifted rotation velocities showed no variation. The point is best illustrated by a comparison between the time history of the discharge voltage for a pair of experiments taken under identical conditions, modulo the capacitor bank size, as displayed in Fig. 4.9.

#### 4.4.2 Capacitor Bank Voltage

The circuit model of the MCX discharge displays the rotating plasma as the parallel combination of a resistance and capacitance connected to the supply bank through a current limiting series resistance. Therefore one might assume that were

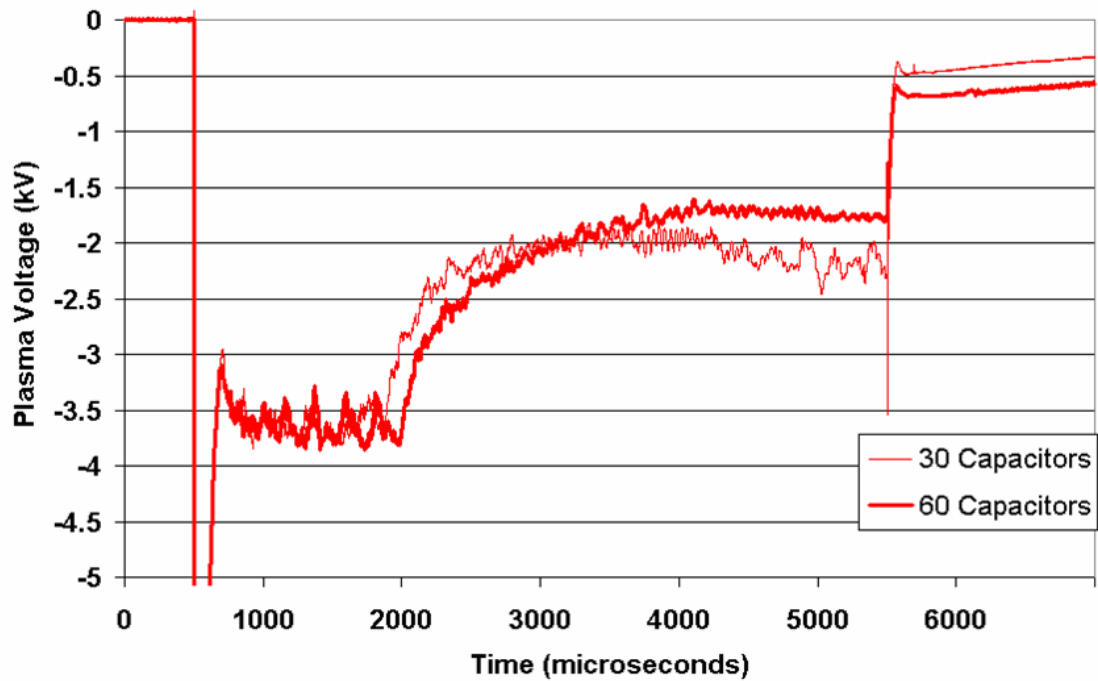


Figure 4.9: Comparison of plasma voltage traces with alternate source bank sizes. The above figure displays the time history of the MCX discharge for experiments undertaken with varying capacitor bank sizes. For times short as compared to the decay time of the bank, there is very little distinction. The differences become apparent in the larger bank's ability to maintain the O-mode type secondary discharge as well as the larger post crowbar voltage and decay time.

we to increase the initial voltage on the supply bank, an increase to the voltage across the discharge would result. As displayed in Fig. 4.10 this does not appear to be the case. The roughly linear scaling evident at the lower bank voltages does not continue past a peak discharge voltage of approximately 4 kV.

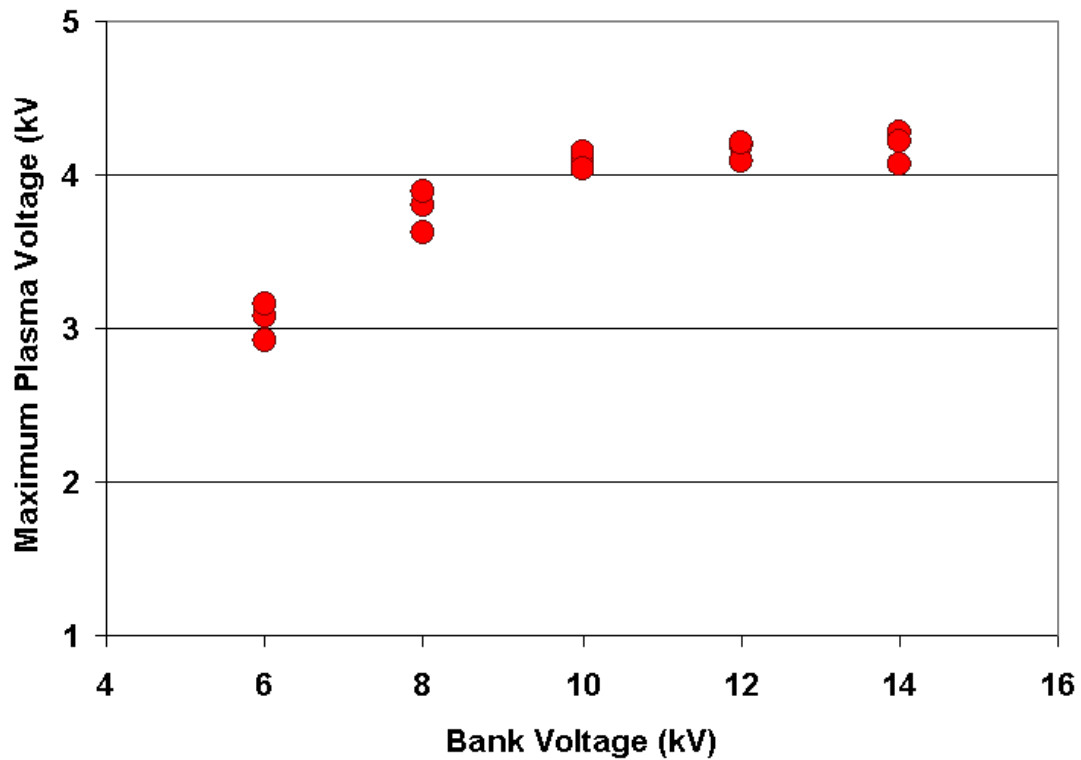


Figure 4.10: Effect of increased initial capacitor bank voltage upon maximum discharge voltage. This voltage scan was undertaken with all alternate external parameters held fixed and shows that increasing the bank voltage beyond a critical value does not result in an increase in the voltage present across the discharge.

This voltage limit has been evident despite variations in all other input parameters besides the magnetic field. Increases to the midplane magnetic field, will allow for an increased discharge voltage, however as  $v_\phi = V_p/aB_{mid}$ , this increase in the plasma voltage does not result in a larger rotational velocity. Therefore the conclusion reached is that the behavior of the discharge voltage is due to a limitation within  $v_\phi$  rather than the voltage explicitly. The underlying cause of this limitation is discussed in Chapter 5

In addition, an increase in bank voltage will result in a decrease in overall discharge resistance as displayed in Fig. 4.11. This is also consistent with a voltage limit across the discharge. For a constant external series resistance, as the source voltage is increased the overall plasma resistance must drop in order to maintain a constant voltage across the discharge. Thus for a constant plasma voltage, the plasma resistance ( $R_P$ ) should vary according to

$$R_P = \frac{V_P}{V_B - V_P} R_S \quad (4.8)$$

As the discharge resistance is an intrinsic parameter, this decrease in overall system resistance could signify the creation or strengthening of insulator interaction based current paths as predicted by the Critical Ionization Phenomenon enumerated in Chapter 5. These events are separate but possibly not uncoupled from the full insulator breakdowns which occur during the H-O transition state.

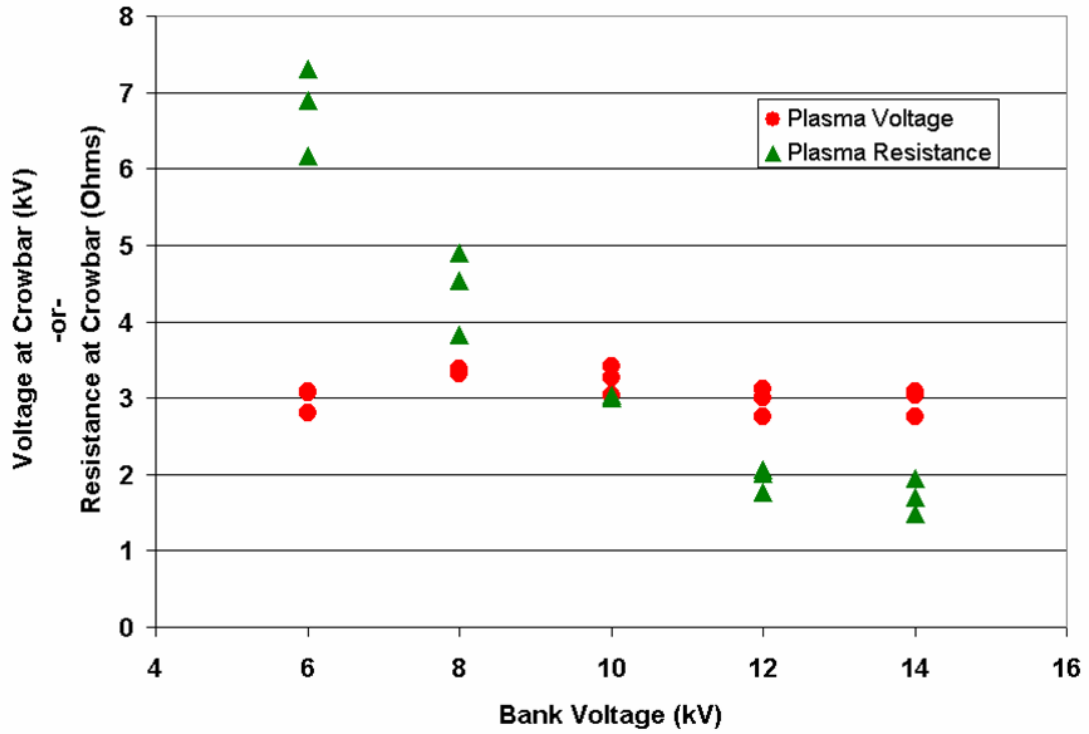


Figure 4.11: Effect of increased bank voltage on discharge resistance. Increasing the voltage applied to the capacitor bank decreases the effective plasma resistance. This behavior appears to be a result of the limitation on the maximum plasma voltage experienced by the discharge. The plasma resistance drops at higher voltages so as to maintain the nominal 4 kV discharge voltage as shown in Eqn. (4.8). The voltage and resistance measurements shown above are both recorded at the plasma crowbar

Operation at elevated bank voltages precludes a full crowbar scan of the data due to ignitron holdoff problems. As such we simply note that there does not appear to be any dependence between bank voltage and momentum confinement time. For the few instances where a plasma crowbar has been accomplished, we have noted an elevated recovered charge which compensates for the increased discharge current, thus leaving the momentum confinement time nearly constant.

### 4.4.3 Series Resistance

An alternate method of increasing the voltage across the discharge would be to reduce the value of the current limiting series resistance. If the MCX discharge was able to manifest a constant plasma resistance, a larger portion of the bank voltage would then appear across the discharge. This does not appear to be the case. As long as there is sufficient input power to maintain a nominal volume discharge, the external series resistance has no demonstrable effect upon discharge velocity or momentum confinement time.

There is however, an apparent dependence between the external series resistance and the measured plasma resistance as shown in Fig. 4.12. We believe that this effect is also due to the critical ionization effect. If there is a limit to the voltage which can be maintained across the discharge, then the plasma will adjust its overall resistance to compensate for adjustments to the series resistance thus preserving that voltage. This could be accomplished by the introduction of lossy areas at the

axially terminating ends of the vessel which could conduct additional current, thus presenting the appearance of an overall lower plasma resistance.

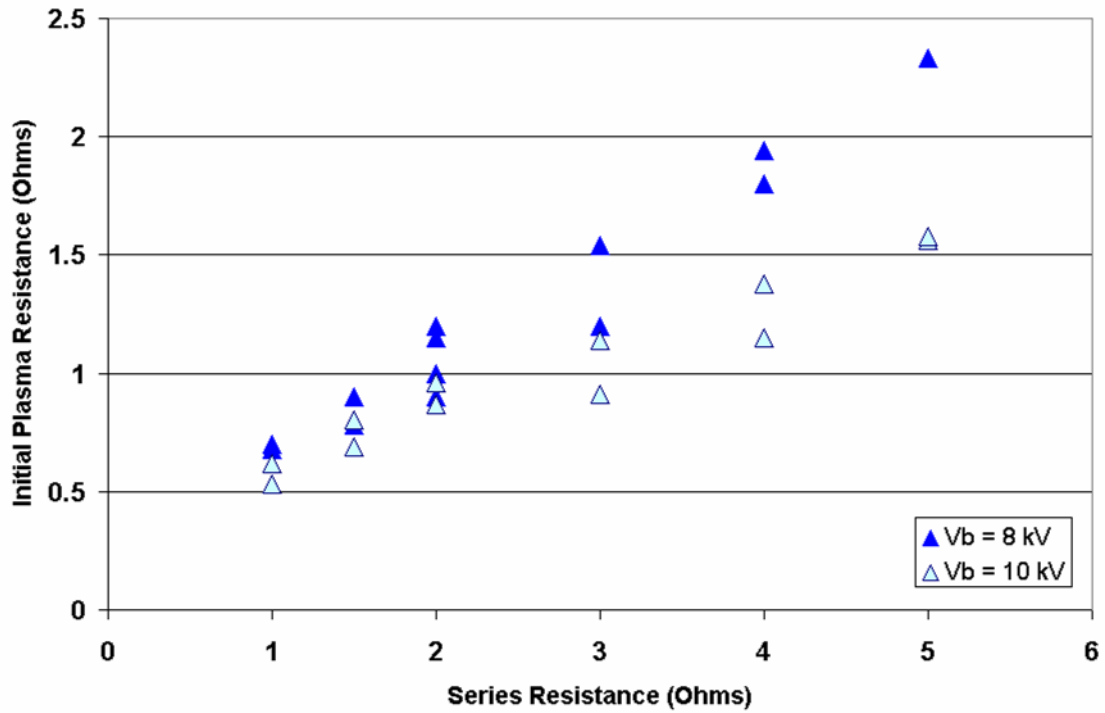


Figure 4.12: Functional dependence of the initial plasma resistance upon external series resistance. In this instance, the plasma resistance was recorded at the conclusion of the formation phase. Experiments were undertaken at both 8 and 10 kV over a range of 1-5  $\Omega$  so as to illustrate the discharge dependence upon variations to the external series resistance.

#### 4.4.4 Coupling between bank voltage and series resistance

The functional coupling between the applied capacitor bank voltage and the series resistance results in band of operational parameter space as displayed in Fig. 4.13. Excursions from this narrow parameter band result in discharge conditions, as described in Section 3.6, which are not optimal for achievement of program goals.

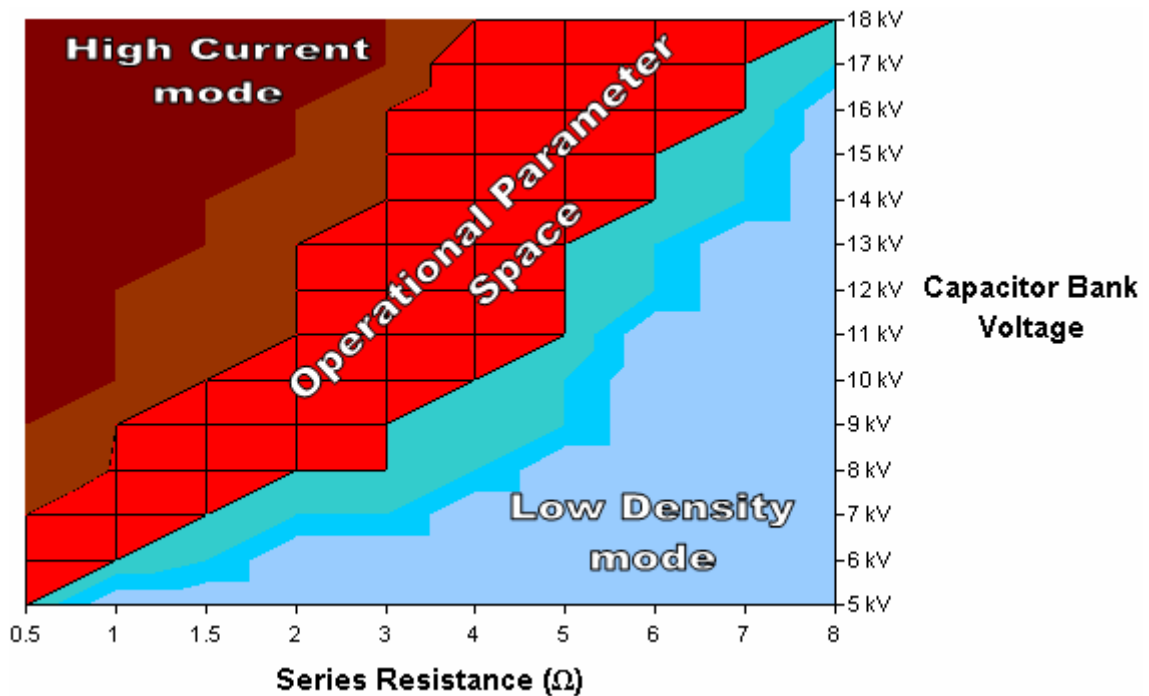


Figure 4.13: Operational parameter space for the MCX discharge. This plot of the available MCX voltage and resistance scalings displays the coupling between bank voltage and series resistance in determining the parametric band in which MCX should operate so as to achieve optimal performance. The non-ideal “Low Density” and “High Current” modes have been described in section 3.6

The maintenance of an equivalent parameter set over a nominal voltage and resistance scaling requires more than the application of a multiplicative factor applied to both components. The discharge achieved with a bank voltage  $V_B$  and series resistance  $R_S$  (Case 1) will not behave identically to a discharge achieved for a bank voltage  $2V_B$  and resistance  $2R_S$  (Case 2). The equivalent series resistance to obtain an identical discharge for condition 2 based upon condition 1 is

$$R_{S2} = R_P + 2R_{S1} \quad (4.9)$$

As such, an 8 kV, 2  $\Omega$  discharge is most closely mapped to a 16 kV, 6  $\Omega$  parameter set given a nominal 2  $\Omega$  estimated discharge resistance. In addition, in order to maintain an equal time history throughout the discharge, the time decay of the capacitor bank should be equivalent.

$$\begin{aligned} \tau_1 &= (R_{S1} + R_P) C_1 \\ \tau_2 &= (R_{S2} + R_P) C_2 = 2(R_{S1} + R_P) C_2 \\ C_2 &= \frac{1}{2} C_1 \end{aligned} \quad (4.10)$$

This is equivalent to the statement that the charge present on the capacitor banks in the two instances, needs to be equal. Thus our 8 kV, 2  $\Omega$  discharge undertaken with 60 capacitors can only be fully replicated at the 16 kV, 6  $\Omega$  parameter set with 30 capacitors. This equivalence could be utilized to circumvent the inhomogeneities in discharge performance caused by the variable behavior during the ionization event, as the elevated voltage in the latter case will allow a more rapid discharge formation than in the former.

## 4.5 Forced limitations on radial discharge extent

The volume averaged rotational velocity of the MCX discharge is governed by the equation  $v_\phi = V_P/aB$ , and while it is relatively simple matter to adjust the externally applied magnetic field  $B$ , and we have also demonstrated at least a mild control over the discharge voltage  $V_P$ , the radial extent of the discharge, "a" is a much more difficult parameter to modify. To quantify the discharge dependence upon radial extent, we have undertaken a set of experiments whereby we have adjusted the plasma radius by explicitly reducing the number of viable plasma carrying flux surfaces. This has been accomplished by clamping a set aluminum rings onto the core of the vessel. During the discharge, these rings are lifted to the same electrostatic potential as the core and thus extend the no-slip boundary condition from its original location at the field line which just brushes the core, to one which is now terminated on the edge of the aluminum disk.

### 4.5.1 Aluminum Limiter Schematic

As shown in Fig. 4.14, the aluminum limiters which have been installed on MCX are best characterized as sets of rings which can be rigidly clamped onto the high voltage core. There are three such sets, with outer radii of 1.5, 2, and 2.5 inches. These rings have been used to redefine the first good magnetic flux surface by forcing all of the inboard field lines to the same electrostatic potential. As these lines will no longer support a rotational discharge, the plasma's radius is reduced

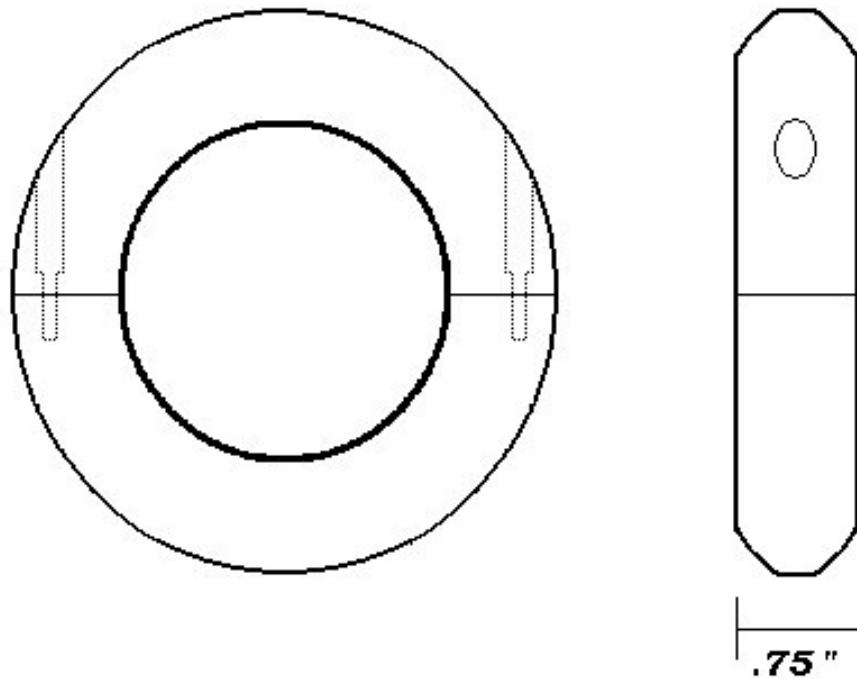


Figure 4.14: Diagram of the discharge limiting clamp. This drawing is representative of the aluminum clamps utilized to radially limit the MCX discharge. The pieces were machined from aluminum disks which were subsequently cut in half. The dotted lines represent tapped holes into which were inserted vented machine screws allowing the assembly to be rigidly clamped onto the central core. This facilitates the installation of the limiters without necessitating a removal of the high voltage core from the interior of the experimental chamber.

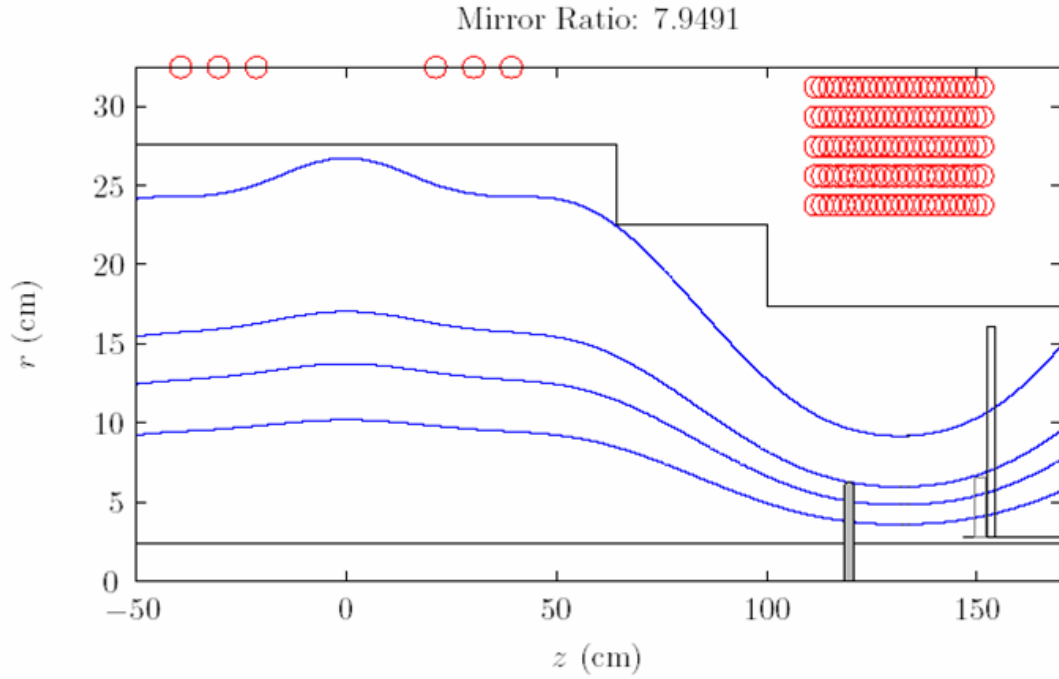


Figure 4.15: Magnetic field map for radially limited discharges. The above graphic displays the limiting flux surfaces present for the various aluminum clamps. The largest of these is represented here by the grey rectangle at  $z = 120$  cm. The outermost field line is representative of the last good magnetic flux surface, while the three inner lines display the mapped locations of magnetic field lines which would just contact the edge of the 1.5, 2, and 3 inch radial limiting surfaces placed symmetrically at an axial location 5 inches inside the respective mirror throats.

by a commensurate amount. This results in plasma widths of 10, 13 and 16 cm respectively as displayed in Fig. 4.15. Data from this set of experiments is then compared with our nominal 20 cm radial extent.

#### 4.5.2 Results of radial scan

These limiter experiments were initiated in an attempt to return the discharge to an HR type mode. In order for a 200 km/sec discharge to maintain consistency between an  $\mathbf{E} \times \mathbf{B}$  rotation velocity, and a nominal discharge voltage of 4 kV, the concession had to be made that the discharge was radially compressed from a nominal width of 20 cm down to  $\sim 10$ -13 cm. The inability to recover these high velocities upon alteration of the bounding insulators from plastic to MACOR led to the conjecture that perhaps the surface of the polyethylene had become partially conductive during the discharge, thus leading to a electrostatic shorting of the field lines which had terminated upon its surface. To test this, the aforementioned limiters were inserted.

Within the context of the rotational velocity, the experiment was unsuccessful. The decrease in radial discharge extent was more than compensated for by a subsequent drop in burning voltage, as shown in Fig. 4.16. The quadratic scaling noted in the discharge voltage for the 8 kV parameter scan can be accounted for by examining the power balance MHD equation

$$\frac{(Vol)nM_i u_\phi^2}{\tau_m} = I_P V_P \quad (4.11)$$

$$(Vol)nM_i \frac{V_P^2}{a^2 B^2} = V_P Q_P \quad (4.12)$$

By defining the "charge density" as  $q = \frac{Q}{(Vol)}$  we remove the volumetric dependencies of the discharge and are left with

$$V_P = \frac{B^2 q}{nM_i} a^2 \quad (4.13)$$

This observed quadratic scaling fails at higher voltages, a condition we believe to be primarily due to the velocity limiting effect noted in Chapter 5. In such a case the plasma will transition to a model whereby the discharge voltage is limited by the critical velocity and the scaling then becomes linear in the radial variable  $a$ .

$$V_P = v_{\phi,crit} a B \quad (4.14)$$

A decrease in the exponent within the power law data fit at higher voltages supports this conclusion. To demonstrate that we had not yet reached a condition of this sort at the 8 kV parameter set where the previous scaling was undertaken, we plot Fig. 4.17 which displays the calculated rotational velocity for the already presented data.

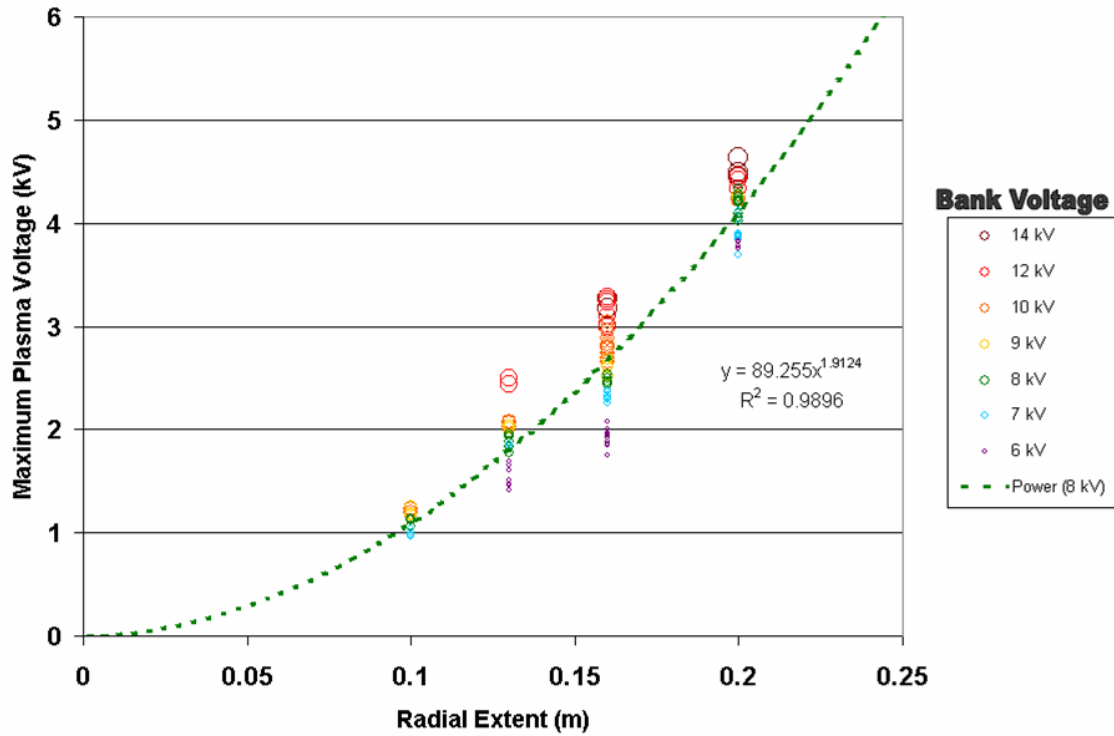


Figure 4.16: Radial scaling of maximum discharge voltage. The scaling of the discharge voltage is very nearly quadratic for an 8 kV bank voltage. This concise power law scaling disappears at higher voltages, possibly due to limit on the rotational velocity.

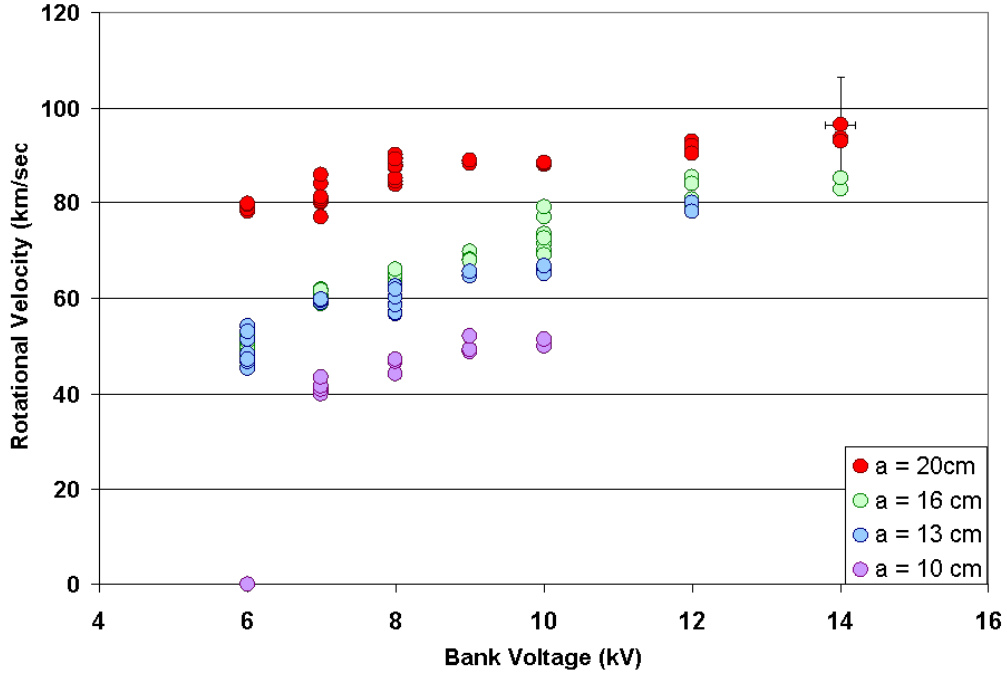


Figure 4.17: Rotational velocity for varying discharge extent and initial bank voltage. The salient point to discern from this display of calculated rotational velocity ( $v_\phi = V/aB$ ) is that we have not yet achieved the limiting velocity for the majority of the radial extents at 8 kV, and therefore the scaling should not be CIV limited. Representative error bars are displayed for the uppermost point

We initiate the discussion on the effects of radial variation on the discharge resistance by plotting Fig. 4.18. We further supplement our discussion of radial dependencies with an additional examination of the parametric reliance upon input voltage. This additional axis has been added to illustrate the difficulty in determining a scaling law for this particular parameter. As shown in Table-4.4, the results of a power law fit to the recorded data varies greatly, depending upon the input bank voltage. As shown, a larger radial extent will always result in a greater plasma resistance, however as maximum plasma voltage for a particular radial extent appears to be a fixed quantity, discharge resistance decreases with applied bank voltage in agreement with Eqn. (4.8)

Plasma Resistance Equation ( $\Omega$ )	$R^2$ Fit Value
$R_{(V_B=7kV)} \cong 1400a^{3.2}$	.96
$R_{(V_B=8kV)} \cong 500a^{2.9}$	.97
$R_{(V_B=9kV)} \cong 130a^{2.3}$	.97
$R_{(V_B=10kV)} \cong 75a^2$	.96
$R_{(V_B=12kV)} \cong 20a^{1.4}$	.84

Table 4.4: Empirical fit to the variation of discharge resistance with radial extent. The preceding tabulation displays empirical fits to the resistance data plotted in Fig. 4.18 explicitly displaying the dependence of discharge resistance upon initial bank voltage.  $R^2$  is the standard coefficient of determination and is a measure of the strength of a fit between the model and the data ( $0 < R^2 < 1$ ).

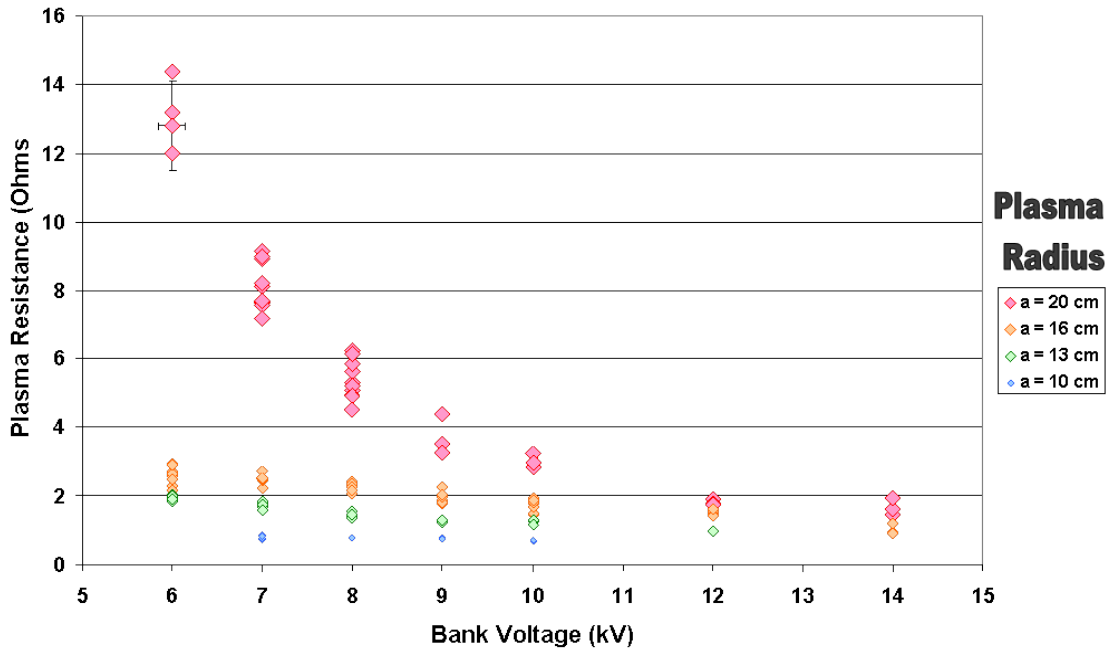


Figure 4.18: Discharge resistance with varying radial extent. We display discharge resistance at plasma crowbar as a function of both radial extent as well as initial capacitor bank voltage. A representative error bar is displayed for a single point. The only conclusive statement which can be made at this juncture is the assertion that an increased radial extent to the discharge will result in an increased system resistance.

Initially ignoring any dependence of the momentum confinement time with initial bank voltage, we plot Fig. 4.19 which seems to display at least a quadratic scaling between momentum confinement time and radial extent. Overlaying a best fit quadratic onto this data, we arrive at an empirical diffusion coefficient for MCX ( $D_{\text{MCX}}$ ).

$$\tau = \frac{a^2}{D_{\text{MCX}}} \quad (4.15)$$

$$D_{\text{MCX}} = 1.19 \times 10^2 \frac{\text{m}^2}{\text{s}}$$

Comparing this to the classical and Bohm diffusive coefficients [16] for the standard perpendicular resistivity ( $\eta_{\perp}$ ), an estimated electron temperature of  $T_e = 10\text{eV}$  a midplane magnetic field of  $B=0.24$  Tesla, and a standard density of  $n=3 \times 10^{20} \text{ m}^{-3}$  we find that

$$D_{\perp} = \frac{2nKT_e\eta_{\perp}}{B^2} \cong 6.4 \times 10^{-1} \frac{\text{m}^2}{\text{s}} \quad (4.16)$$

$$D_B = \frac{1}{16} \frac{KT_e}{eB} \cong 2.6 \frac{\text{m}^2}{\text{s}}$$

$$\frac{D_{\text{MCX}}}{D_B} \cong 45 \text{ and } \frac{D_{\text{MCX}}}{D_{\perp}} \cong 190 \quad (4.17)$$

While it has been shown [32] that the centrifugal force as well as the pressure gradient will assist in the diffusion process, enhancing it by a factor of  $\sim 1 + M_s^2 a/r$ , at our present estimates of a mild supersonic state this does not appear to be sufficient to account for the difference.

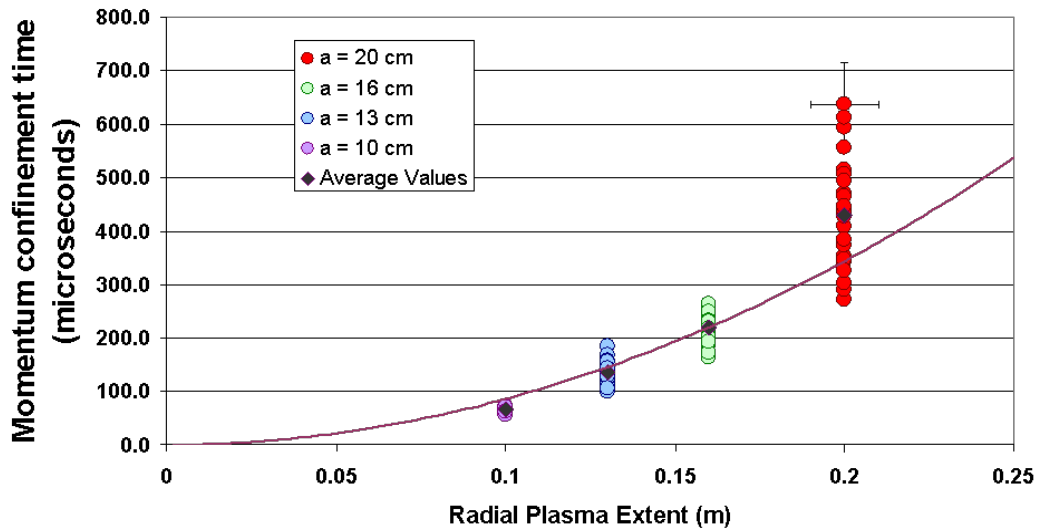


Figure 4.19: Scaling of momentum confinement time with radial discharge extent. The black diamonds represent an average of the momentum confinement times for a particular radial extent and the dotted line represents a forced quadratic least squares fit to the averages. It is this equation ( $\tau = 8400a^2$  (microseconds)) from which we have determined a diffusion coefficient for the MCX rotational discharge. Representative error bars are given for the uppermost point.

If we now subdivide the tau scaling by initial bank voltage as shown in Fig. 4-20 we can see that for an initial input far below the CIV limit (the 7 and 8 kV traces) the diffusive scaling noted earlier is extremely modest. The fact that the power law scaling is stronger than the expected quadratic may be indicative of a nonlinear behavior. One possibility is that we are incorrect to utilize the magnetic limiting flux surfaces to determine the radial extent of the discharge. The neutral penetration depth, calculated in section A.3.4, is 1.54 cm per side. This means that for a plasma width, as defined by the limiting flux surfaces, of 10 cm, only the innermost 7 cm maintains a high degree of ionization and can be expected to facilitate diffusive transport and thus the "a" utilized to determine the empirical diffusion coefficient could require modification. Measurement with a radially resolved H- $\alpha$  detector array is needed to further quantify the radial profile as well as the neutral penetration depth.

## 4.6 Parsing the Multi Dimensional Space for Peak Performance

In summary, we are now able to observe the discharge mapping over the full multidimensional space, thus giving us the ability to ascertain the conditions under which optimal discharge performance may be achieved. Mirroring the order of this chapter we note the following.

- Insulators: The position and geometry of the insulators has a greater effect upon transition probability than nearly any other factor. However, once tran-

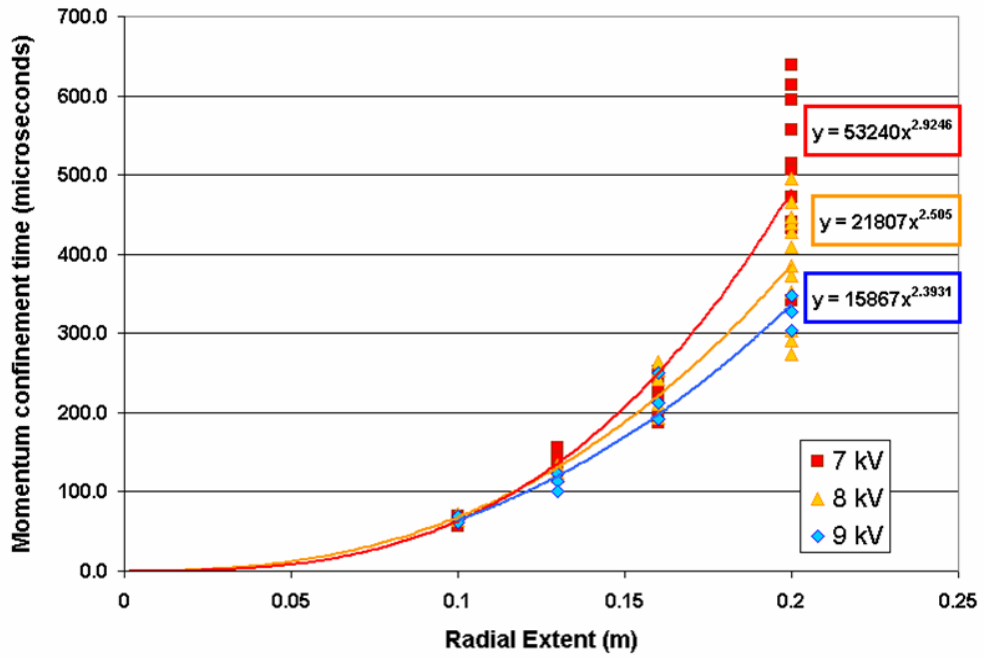


Figure 4.20: Radial dependence of momentum confinement time subdivided by initial bank voltage. The above figure displays the empirical scalings of the momentum confinement time for 3 separate initial bank voltages. The errors for this graph are identical to those in fig 4.19. This graph shows that the dependance of momentum confinement time upon radial extent, is stronger than a quadratic scaling. As a result, a increase in the radial extent could significantly augment the momentum confinement time.

sitions have been eliminated, further insulator adjustments may have little effect. That being said, the plasma neutral boundary interaction at the insulators may be the primary cause of the observed velocity limiting effect. If a way is found to initially mitigate this effect, then the configuration of the bounding insulators may again require careful study.

- Fill Pressure: Under the current auspice of a self generated discharge created by externally applied electromagnetic fields, operations at the present nominal fill pressure of 5 mTorr appear to be ideal.
- Magnetic Field: A larger magnetic field will allow a respectively larger maximum plasma voltage across the discharge. While this may not increase the rotational velocity, the concomitant reduction of the Alfvén Mach number ( $M_A = v_\phi/v_A$  where  $v_A = B/\sqrt{\mu_0\rho}$ ) may allow for greater stability.
- Capacitor Bank Parameters: To an extent, a larger voltage on the bank will lead to a greater plasma voltage. However attempts to drive the system past the CIV limit leads to an overall reduction in plasma performance. The same can be said for the series resistance. The impulse to reduce the series resistance, thereby increasing the discharge voltage is only useful when dealing with a section of parameter space below the voltage limit. While adjusting the number of capacitors will allow for a commensurate increase in the duration of the discharge, it does not appear that this increase will significantly boost the discharge performance.

- Radial Extent. A larger radial extent is strongly beneficial to the discharge. In monitoring the dependent parameters enumerated in our rubric, all scale positively with an increased plasma radius. Although impossible at present to effect a larger radius, it should be noted for future iterations of MCX that even a mild increase in midplane plasma radius may provide a substantial return.

## Chapter 5

### The Critical Ionization Velocity Effect

As a portion of his theory on the origin of the solar system, Alfvén postulated the existence of a critical ionization velocity [4]. This theory predicts an extremely strong increase in the ionization rate of a surrounding neutral gas cloud when the kinetic energy of a transiting ion immersed in a magnetic field is greater than the principle ionization energy of the dominant neutral species. The applicability of this theory to MCX lies in its supposition of a limiting critical velocity as governed by the equation

$$v_{\text{crit}} = \sqrt{\frac{2e\Phi_i}{M_n}} \quad (5.1)$$

Where  $M_n$  is the mass of the dominant neutral species and  $\Phi_i$  is its ionization potential. Many cosmological experiments as well as rotating plasma machines have reported observation of just such a limit [13]

As the rotational velocity in MCX is defined by  $v_\phi = V_P/aB$ , this limitation should manifest as a bounding to the electrostatic potential which can be supported across the discharge for a particular magnetic field and radial extent. Thus increasing the bank voltage would result in little to no effect upon the plasma voltage. To determine if such a limit exists, we have calculated the maximum rotational velocity

for the entire MCX parameter space and plotted it versus applied bank voltage, creating Fig. 5.1. Included in this data set are all the commensurate variable scalings which have been noted in Chapter 4. As is clear from the graph, there is indeed a limitation in the rotation velocity which can be achieved.

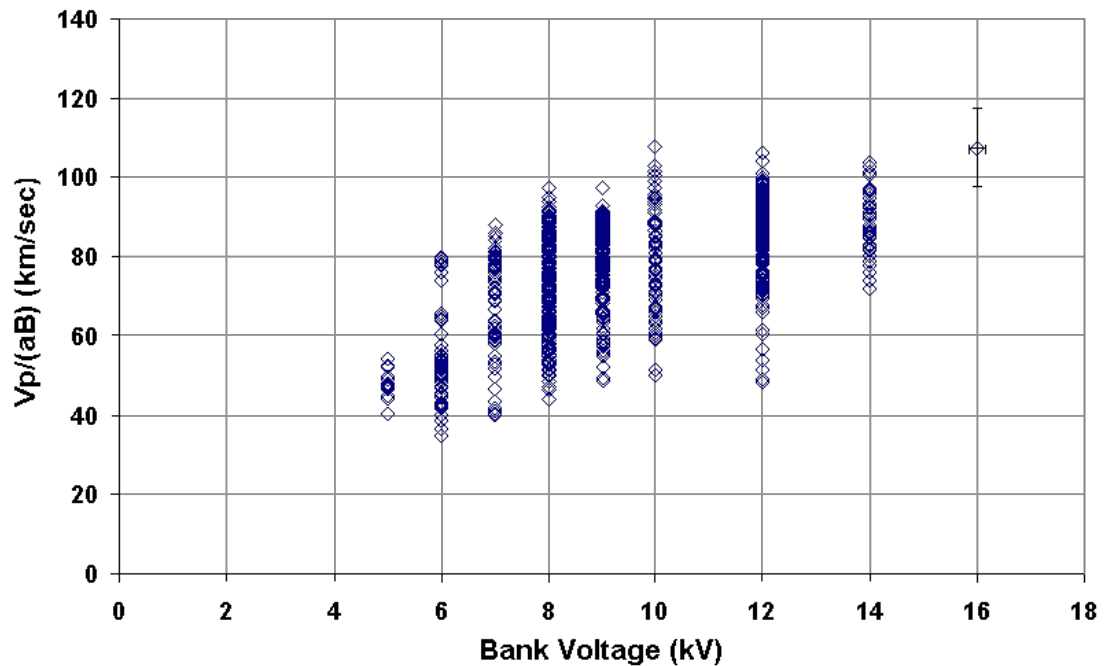


Figure 5.1: Evidence of a velocity limitation on MCX. The above graph plots the maximum calculated rotational velocity ( $v_\phi = V_P/aB$ ) vs. applied bank voltage for the entire data set discussed in this dissertation. Subsumed within this graph are the parametric adjustments made in magnetic field, mirror ratio, fill pressure, series resistance, radial discharge extent, insulator position and insulator geometry. The result of this graph is a clear limitation in the rotation velocity.

The remainder of this chapter outlines the supporting evidence which has been gathered suggesting that the velocity limitation encountered on MCX is consistent with Alfvén's theory of a critical ionization velocity. The question is raised and answered as to the localization of this phenomenon and its commensurate effects upon the volume discharge. We also address the consequences that this presents for the efficacy of the MCX device, including evidence that this limit may be surmountable by judicious choice of discharge conditions.

## 5.1 Manifestation of the CIV

Placing the respective numerical values for a hydrogen type discharge into Eqn. (5.1) results in a projected limiting velocity of 51 km/sec. As the velocities denoted in Fig. 5.1, are clearly larger than this value it remains to be shown how these velocities could be said to be limited by this particular phenomenon. The answer resides in the geometric scaling of the mirror field lines and an assumption that during the quiescent phases of the discharge this limiting effect is localized about the axially bounding insulator surfaces.

### 5.1.1 Location of the discharge limiting surface

The volume of the MCX discharge has been shown to be fully ionized, and far from being velocity limited, the inner and outer radial flux surfaces are subject to no-slip boundary conditions. Therefore, if we are to purport that this velocity limitation

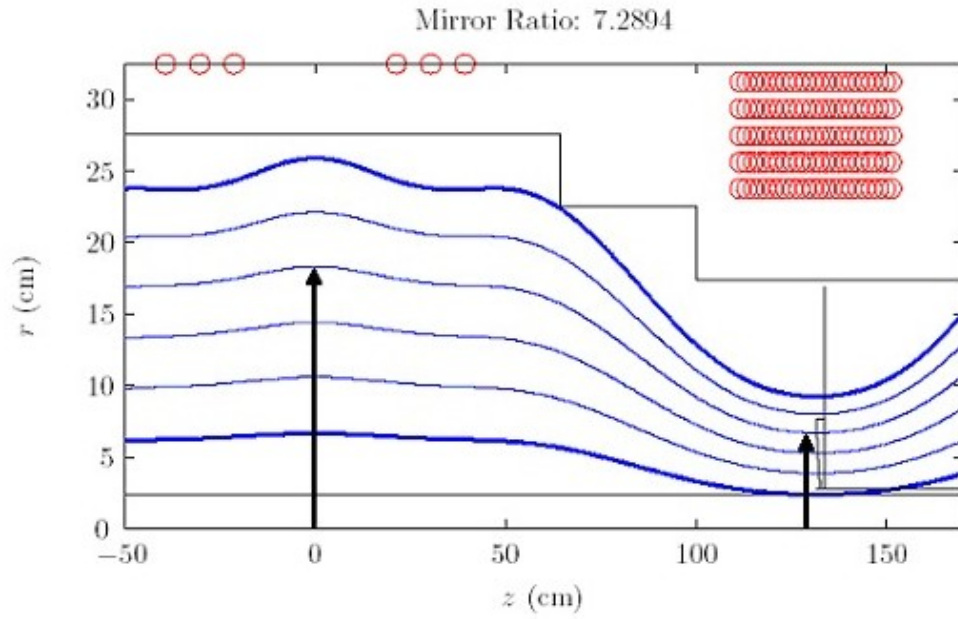


Figure 5.2: Geometric scaling factor for a mirror ratio of 7.2. Assuming isorotation of the field line, the rotational velocity at the midplane for a magnetic field line tied to the insulator surface and limited by the critical ionization velocity is given by  $v_\phi = v_{\text{CIV}}[R_{\text{midplane}}/R_{\text{mirror}}]$ .

is the result of an increase in the plasma-neutral interactions, then the location of this contact must reside at the disk insulators which terminate the magnetic field lines. Treating these field lines as rigid rotors with a constant angular velocity and assuming a radial velocity profile peaked about the core of the discharge, then the central magnetic field line, when mapped back to the insulator location, should become the one limited by the critical ionization phenomenon. For our nominal mirror ratio of 7.2, as displayed in Fig. 5.2, this results in a geometric scaling factor of approximately 2.2. Applying this factor to our calculated critical ionization velocity we arrive at a maximum midplane velocity estimate of between 100 and 120 km/sec in agreement with the presented data.

### 5.1.2 CIV limitations on Discharge Voltage

As noted previously, this phenomenon can also explain the linear dependence between the discharge voltage and the magnetic field. Presented in Fig. 5.3 is the magnetic field scan taken at mirror ratio 4.4 as previously displayed in section 4.3 with an overlay representing a set of assumed constant  $v_\phi$ . As shown, all data falls within the 10 km/sec band between 70 and 80 km/sec. There appears to be a mild dependence upon  $B$ , but over nearly a factor of 2 increase in field strength, there is only a 5% resultant variation in rotational velocity. Even this mild dependency could be explained by constant velocity theory if we relax the requirement that the limiting velocity equation maintains a 0 intercept of  $v_\phi$  with  $B$ . This correction factor amounts to a devaluing of the magnetic field observed by the discharge by

approximately 300 gauss. As all magnetic field values have been recorded en vacuo, this correction factor could be the result of a combination of calibration errors as well as plasma effects.

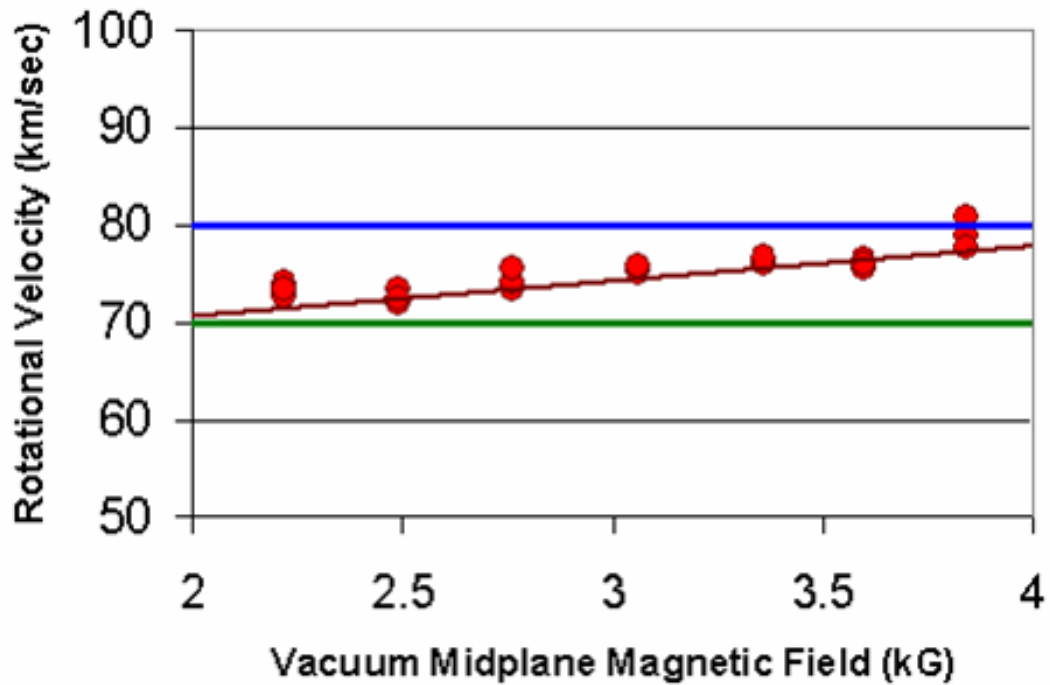


Figure 5.3: Velocity limited magnetic field scaling for mirror ratio 4.4. The dark red line is representative of an 85 km/sec limiting velocity with a magnetic field devalued by 370 Gauss. This adjustment to the vacuum magnetic field removes all scaling of the rotational velocity with magnetic field

### 5.1.3 CIV model for mirror ratio scalings

The mild scaling of plasma performance found to occur within the MCX discharge at alternate mirror ratios can also be explained by the Critical Ionization Velocity phenomenon. If we assume that a corotational magnetic flux surface terminated at the insulators gives rise to the velocity limit noted within the bulk rotational discharge, then an adjustment to the geometric mapping of that field line should result in an alternate midplane velocity.

Therefore, to the previously displayed plasma voltage data, we add an additional discharge voltage scaling at the alternate mirror ratio of 7.2. These results, shown in Fig. 5.4, are consistent with a upshifted constant rotational velocity of 97 km/sec at this new mirror ratio, as compared to a rotational velocity of approximately 85 km/sec at mirror ratio 4.4. While in no way conclusive proof of the CIV effect, this analysis is offered as an addition to the preponderance of evidence which suggests that the MCX discharge is limited by this constraint at this time.

There are some caveats to this particular section which should be enumerated before proceeding. This analysis assumes that the magnetic field offset discussed in the previous section remains constant throughout the mirror ratio scaling as would be consistent with a calibration error. Also, due to the extremely high currents present in the system at reduced magnetic fields, the capacitor bank voltage for the second mirror ratio scan was reduced from 12 to 9 kV. The mild plasma voltage scaling (as displayed in figure 4-10) between these input values was compensated

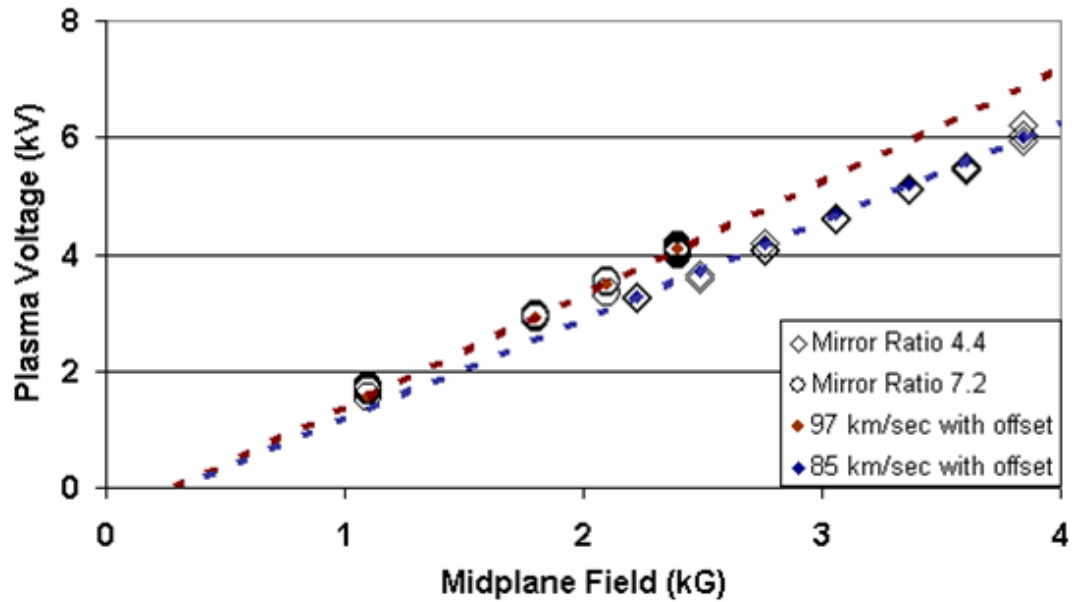


Figure 5.4: Effect of mirror ratio upon magnetic field scaling. The effect of midplane magnetic field upon maximum discharge voltage is plotted for the mirror ratios 4.4 and 7.2. If we apply identical magnetic field offsets to a linear extrapolation of the data we find that a mirror ratio of 4.4 gives rise to a constant maximum midplane velocity of 85 km/sec whereas a larger mirror ratio of 7.2 is consistent with a constant 97 km/sec rotational velocity. This is consistent with the an increased geometric CIV scaling factor for the increased mirror ratio.

for by multiplying the original voltage data by a correction factor. This factor was determined by averaging the maximum discharge voltage for an initial bank voltage of 12 kV over many experiments and dividing this result by a similar average undertaken at an initial bank voltage of 9 kV. Both of these averages were undertaken with a nominal midplane field of 2.4 kG and a mirror ratio of 7.2

## 5.2 Causes of the CIV in MCX

The contact between the ionized discharge and the background neutral gas which gives rise to the critical ionization velocity can become manifest as either a surface or a volume interaction. As there is evidence [5] that even minimal wall contact can be extremely efficient in limiting  $v_\phi$ , interactions of this type are behaviorally similar to volume driven effects, thus making it difficult to distinguish a modal causality when attempting to interpret the CIV. As such, it is entirely possible that both types of relations are present during the time history of the MCX discharge, and therefore both should be examined in an effort to categorize their effect.

### 5.2.1 Physical underlying mechanism for the CIV effect

Alfvén noted [4] that the orbital distances of the various planets can be explained if one theorizes that a rapid increase in the ionization of a neutral gas falling through a magnetic field is governed by the condition

$$\frac{1}{2}Mv_{crit}^2 = e\Phi_i \quad (5.2)$$

In such a case, the nonionized gas, gravitationally attracted to a central body becomes ionized and tied to the magnetic field lines and thus ceases its descent. The critical ionization velocity phenomenon is thus proposed as an explanation for the origin of the solar system.

However the elegance of this particular theory is somewhat marred by the fact that there is no easily explainable mechanism which allows for the efficient transfer of energy between the species. Direct ion-neutral collisional ionization appears to be insufficient to explain this phenomenon as there is inadequate energy available to a critical velocity ion, in the center of mass frame, to effect the rapid ionization of the background neutrals. A critical velocity many times larger than observed would be necessary for this sort of occurrence. As such, there is general agreement that the energy must somehow be transferred to the attendant plasma electrons, which are then themselves responsible for the ionizing event. Therefore most of the accepted explanations of the CIV phenomenon are based upon an electron ionization model.

The initial such model was presented by Alfvén [3] in conjunction with his first homopolar CIV experiments. He explains:

”Seen from the coordinate system of the plasma, atoms with an energy  $eV_1$  knock out ions from certain regions of the plasma, creating irregularities within the plasma. The magnetic field prevents the electrons from neutralizing the charge

differences immediately. The process can continue until voltage differences are produced which are large enough to prevent further ions from leaving the region. In this way voltage differences  $V_1$  are produced in the plasma and electrons can be accelerated by these. Hence, electron velocities corresponding to  $V_1$  are produced and these velocities just suffice for the ionization of the atoms”

Spatial irregularities sufficient for ionization have also been proposed by Lehnert [38] and tested in the F1 device by Bergstrom and Hellston [10] In their experiment, a set of 50 diagnosed concentric metal rings were placed on the end insulators. The initial motivation was to surpass the CIV limit by ”short circuiting” these spatial electric field structures. In this attempt they were unsuccessful, however they did make an interesting observation.

Their discharge displayed a quiescent corona for rotational velocities below the CIV. However, as the applied transverse electric field was increased into the CIV regime, the plasma resistance between the rings which corresponded to a local critical velocity dropped precipitously. At this point the discharge became lossy and irregular and ceased further acceleration.

The conditions depicted in the above experiment, as they apply to MCX are of the plasma-insulator interaction type. These effects are visible in MCX as we attempt to drive the discharge past the critical ionization velocity for our system. Attempts to increase the discharge voltage by a subsequent application of elevated capacitor bank voltage simply leads to a severely depressed plasma resistance.

The utilization of the CIV as an ionization source to facilitate the widespread volume breakdown of a crossed field discharge as suggested by Himmel and Piel [31] is not readily demonstrable by this particular model. However as the CIV process has been found to operate over a wide range of parameters, it does not seem at all unlikely that a single model will be insufficient for all situations.

### 5.2.2 Plasma/Neutral interactions during ionization phase

Conditions favorable for the formation of a critical ionization phenomenon exist during the initial stages of a rotating discharge. As the breakdown is a localized occurrence within a previously neutral volume, it has been suggested by some [13] that the presence of this ionizing mechanism is responsible for the robustness and totality of the ionization present in crossed field discharges.

Rotating spokes observed during the acceleration phases of several rotating plasma experiments [9, 40] are consistent with the ionizing front model of the limiting velocity phenomenon. In summary, this model suggests that the formation of a spoke within a crossed field geometry leads to a localization of the electric field resulting in a supercritical spoke drift. This supercritical ribbon, after a small number of rotations was observed [31] to develop into a spiral structure instrumental in facilitating the creation of an azimuthally homogenous breakdown thus resulting in the observed volumetric discharge.

This interaction, beneficial in its creation of a fully ionized plasma and would

still exist in the boundary layers of the discharge as defined by neutral penetration depth, however given that extensive shearing between radial layers is expected, this may not be able to explain the limit on the rotational velocity found within the fully ionized core of the discharge.

### 5.2.3 Boundary interactions at the insulating surfaces

Recombination of the plasma on the insulator surface creates a boundary wall layer. While this layer may not be extensive, it has been observed by Lehnert [6] that for a fully ionized volume discharge, a wall layer thickness of as little as 1mm is fully capable of limiting the rotational velocity of the entire discharge. It is this interaction which appears to be responsible for the inability to further accelerate the discharge once a complete ionization has occurred.

As outlined at the beginning of this chapter, the interaction located at the insulator face is translated into the central plasma volume by means of the co-rotation of the field lines. Removing this interaction would require a decoupling between the primary discharge volume and the insulating surfaces. To facilitate this event, the insulator position was varied from a location directly at the magnetic maximum to a position roughly  $1 \times 10^3$  ion larmor radii behind this mirror throat. It was hoped that there might exist a critical distance beyond which the central rotating plasma could detach from the insulators, thus allowing for a supercritical state. No such threshold distance was observed.

We note here that throughout the insulator scan, the rotational velocity of the discharge remained unchanged. This may initially present as somewhat surprising given the varying magnetic field geometry at the insulator face. As the assembly is moved away from the magnetic maximum, the field line which corresponds to a plasma-central location terminates on the insulators at an increasing radius, thus reducing the CIV geometric scaling factor. We explain this discrepancy by noting that while axially translating the insulators should result in a change in the limiting flux surface due to variations in the magnetic field, there will still exist a field line at the insulator face which reaches the critical velocity and it will still map back to the center of the discharge at the nominal geometric scaling. This may however result in an alternate velocity profile, one peaked more to the inboard side of the discharge as the insulator is moved further out. Radially resolved spectroscopic measurements should be able to determine if such an effect occurs. This would also suggest that there exists a point beyond which the first good flux surface also becomes the CIV limiting surface. If such a point exists, translation of the insulators beyond this juncture should result in a marked decrease in overall performance.

An additional consequence of this insulator interaction is the limitation which it places upon penetration of the discharge for diagnostic purpose. It has been demonstrated [12] that an intrusion into a discharge by an object of radius greater than 2.5mm can have a demonstrable limiting effect upon the entire plasma volume thus making a minimally perturbative diagnostic almost functionally impossible

### 5.3 CIV check with alternate fill gas

As CIV theory is completely upon the majority species of the neutral gas, the most obvious test for this limiting mechanism would entail an alteration in the type of backfill gas, thus allowing the discharge to be struck in an alternate medium. As the velocity scaling is highly species specific, one should easily be able to monitor the discharge to see if the results are indeed consistent. Exactly this experiment was undertaken for a Macor insulated MCX discharge. If we assumed that recorded voltage on the magnetic field scaling data from section 4.3 was limited by a critical ionization velocity effect then the CIV equation for a Hydrogen discharge (subscript H) with equivalent geometric scaling factor  $\alpha$  is

$$v_\phi = \frac{V_{P_H}}{aB} = \alpha \sqrt{\frac{2e\Phi_H}{M_H}} \quad (5.3)$$

As such, a prediction for the maximum voltage of a majority Helium type discharge should follow the form

$$V_{P_{He}} = V_{P_H} \left[ \frac{\Phi_{He}/M_{He}}{\Phi_H/M_H} \right]^{1/2} \quad (5.4)$$

The results of this experiment, displayed in Fig. 5.5, show strong agreement between the predicted values for a helium discharge, and the recorded experimental data. The correlation between the experimental results and the theoretical prediction provide further evidence that the MCX discharge is ionization velocity limited.

A confirmation that we were creating a majority helium discharge was performed utilizing the Ocean Optics broadband spectrometer. By monitoring the spectrum over a series of conditioning shots, we were able to observe a marked decrease in the intensity of the nominal set of hydrogen emission lines and a simultaneous increase in the strength of the expected Helium lines, thus lending credence to the efficacy of this alternate species test.

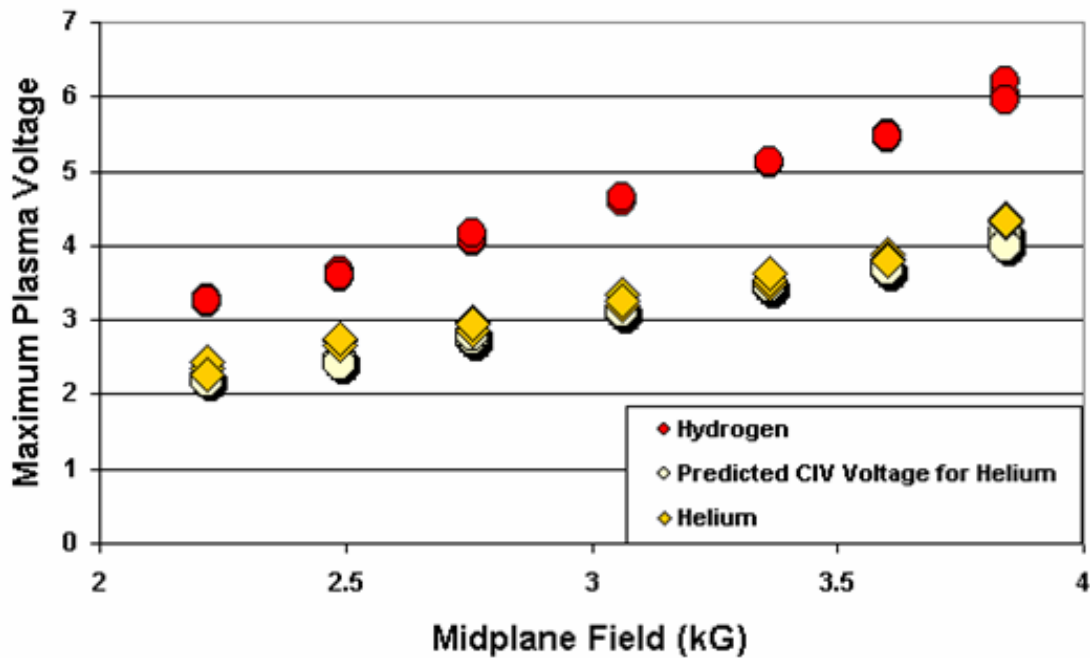


Figure 5.5: Predicted maximum plasma voltages for a helium discharge based upon velocity limited hydrogen data. If we assume that the rotational velocity, and therefore the plasma voltage of experiments undertaken with a hydrogen backfill (red dots) are CIV limited, then the data from those experiments can be utilized as a predictor (yellow dots) for a similar discharge struck in a helium environment (yellow diamonds)

An additional test of the species dependence utilizing nitrogen was unsuccessfully attempted. We were unable to confirm the presence of either a full volume breakdown, or a rotational discharge in these tests. In addition, this test was attempted after the reinsertion of the polyethylene endplates. Their propensity to transition into O-type modes and concomitant post shot pressure rise made unambiguous interpretation of the resultant data impossible.

## 5.4 Supercritical Velocities

As we have noted before, the CIV interaction which limits the discharge is strictly a plasma neutral boundary interaction. If we were therefore able to mitigate or completely remove this interaction, then this set of limiting conditions would no longer exist. This section briefly summarizes the attempts made by prior experiments to surpass the CIV limitation and comments on their success as well as their applicability to the MCX discharge.

There has been some indication that there is a threshold power input necessary to “punch through” this limitation so as to access supercritical velocities. Smaller experiments [6] have been able to surpass the CIV limit through just such an increased input power application. Above a critical level, the increased discharge current results in a higher “burning” voltage, although it is unclear if there is a commensurately higher rotation velocity. Interpretation of these results seems to suggest that upon reaching this particular current level, the full volume of the ex-

perimental vessel has now become fully ionized, thus removing the limiting neutral interaction. Such a tactic is impractical on an experiment the size of MCX due to the extensive gas reservoir which surrounds the plasma volume. While a reduction in the background neutral density is certainly possible through an externally applied limitation to the gas reservoir, simply reducing the fill pressure to attempt to spark a discharge in a low density may not be sufficient to overcome the CIV effects as plasmas at this low density have been found to be fully permeable to neutral penetration [40] and therefore may end up susceptible to volume CIV effects.

Those experiments which have succeeded in attaining supercritical velocities at reduced densities have done so by creating a discharge which is limited in spatial extent and therefore bounded by vacuum, as opposed to a neutral gas blanket. As the thermal speeds of even room temperature neutrals is such that the transit time to the bounding walls of the experimental chamber is small, the window for ionization and confinement of a discharge is extremely narrow. Success has been achieved then, not through a transitory gas puffing, but by the more robust method of plasma gun injection. As demonstrated by Abramova et al [2], the utilization of a polyethylene erosion injector is sufficient for creation of an ionized discharge which can then be driven at supercritical speeds. The discharge remains stable until such time as there is sufficient leakage to the end insulators to allow the critical velocity phenomenon to manifest.

Supercritical velocities exceeding the Alfvén ionization condition by nearly a factor of 40 have been recorded on the PSP-2 device[1]. These velocities were

obtainable due to the presence of a rapidly ionized localized gas puff which kept neutral densities at the insulator surfaces below the limit enumerated by the left branch of the Paschen curve as well as a strongly controlled electrostatic profile and radial potentials of up to 1 MV.

## Chapter 6

### Future MCX directions

The present intent of the Maryland Centrifugal Experiment is to determine the efficacy of the centrifugal confinement mechanism in order to create a fusion type system. To that end we examine the present parametric range of the MCX discharge so as to determine the scalability of the system. Having detailed the consequences of Alfvén's Critical Ionization Velocity in the previous chapter, we now look at possible methods of mitigating the recorded effects. We then examine the discharge trends in an attempt to project performance boosts for future MCX iterations.

#### 6.1 Possible solutions to the present MCX limitations

While not conclusively proven, the evidence suggests that the major limitation present in the MCX plasma system is the Critical Ionization Velocity phenomenon. This effect curtails the accessible rotational velocity throughout the discharge and as a result the sonic Mach number critical to the centrifugal effect is also restricted. Since any attempts to utilize this configuration as a confinement scheme must be able to surpass this limitation, we therefore discuss the various possible methods of surmounting this obstacle.

### 6.1.1 Consequences of the CIV on machine design

As supercritical velocities are necessary for centrifugal confinement, care must be taken in the design and implementation of a discharge scheme in order to eliminate CIV effects. The experiments conducted on the PSP-2 device [1] have demonstrated rotational velocities up to 40 times greater than the CIV and have found the open mirror configuration presently employed on MCX to be extremely efficient in minimizing the wall interaction. We therefore conclude, that wholesale changes to the MCX geometry are unnecessary and that implementation of an alternate, but topologically similar dipole configuration [40] will most likely not reduce the interaction any further.

Furthermore, it has been noted [14] that the deceleration interaction between a supercritical plasma and a neutral dominant region is strongly mitigated by the presence of an intervening subcritical plasma ‘buffer’. While the mechanics allowing for a violation of the frozen-in theorem in either the sub or supercritical regimes as is necessary for differential rotation is not well understood, it has also been observed [40] that the isorotation law has been regularly violated in rotational discharge experiments conducted at high mirror ratios.

This becomes relevant to the MCX discharge in the following manner. Wishing to minimize the interaction between the field terminating insulators and the bulk rotational discharge, the insulating assemblies should be pulled as far away from the center of the vessel as possible. However, the resultant reduction of the magnetic

insulation at the insulator surface leads to a greater cross field conductivity and an increased occurrence of O mode discharges. Ideally, we would wish to be able to move the insulators back from the primary discharge volume without incurring this secondary effect. This may be possible with the installation of additional magnetic coils located at the end flanges as displayed in Fig. 6.1.

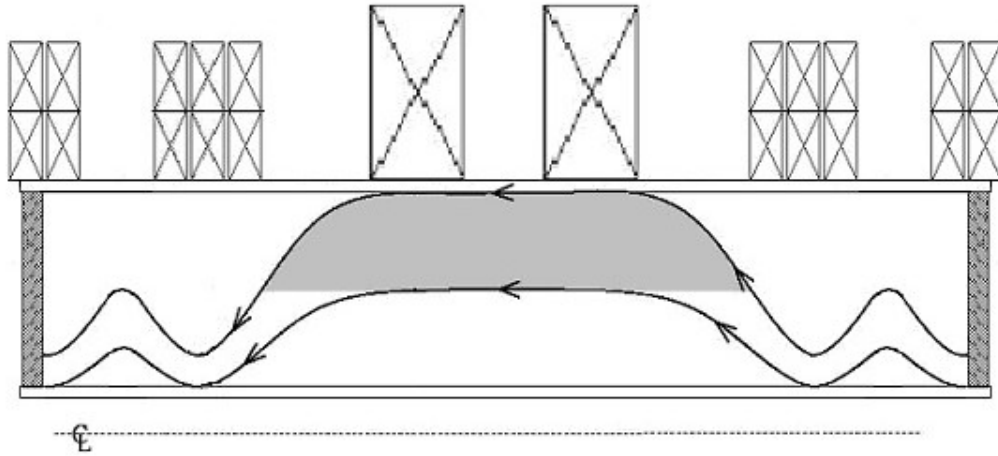


Figure 6.1: MCX with modified terminal field. Supplementing the present MCX field geometry with additional mirror coils allows the insulators to be axially distant from the discharge while maintaining a large magnetic surface insulation. This should minimize the plasma-neutral boundary interaction.

These supplemental coils will serve to increase the field strength at the insulator location, thus inhibiting the cross field breakdown. In addition there is now a secondary buffer region existent between the discharge volume and the terminal insulators. The addition of these end regions has nothing to do with the efficiency

of the confinement scheme, and exists simply to mitigate edge effects. This coil configuration, when coupled with the spatially limited discharge which will be proposed in the succeeding section, should greatly reduce the plasma insulator edge effects.

### 6.1.2 Construction of a no cost plasma injection gun

More so than adjustments to the insulators, the simplest way to circumvent the occurrence of the critical ionization velocity would be to ensure that the discharge is bounded by vacuum rather than a neutral gas blanket. It has been experimentally observed [13] that the CIV effect will not occur if the background neutral pressure at the insulating surface is lower than the value dictated by the left hand side of the Paschen Curve.

Creating this vacuum barrier can be attempted in one of two ways. A spatially localized background gas puff can be introduced into the vessel and the discharge struck within this expanding neutral cloud. The difficulty in this approach lies within the extremely short time in which the gas cloud remains isolated from the bounding insulators. As the neutral particles are unaffected by the applied electromagnetic fields, if we were to choose to maintain the same crossed field ionization mechanism as is presently implemented, it is unlikely that a full breakdown could be achieved in the requisite sonic transit time.

The second, and preferred method, of creating a localized discharge is the insertion of a preionized plasma ‘blob’. An ionized volume is created external to the

primary experimental space and driven into the background electromagnetic fields. It is then ‘caught’ within the confinement scheme and begins the nominal  $E \times B$  rotation. A modified Marshall gun is presently being built which should create just such a condition, however as there have been production difficulties in the implementation of this complex system, we present here the plans for an alternate injection source.

This design is predicated on the premise that a simple plasma injection source could be rapidly constructed from materials found within the MCX inventory and implemented without major system modifications.

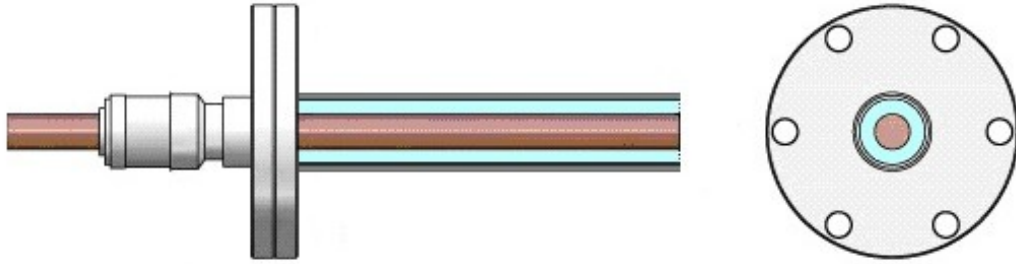


Figure 6.2: Assembly drawing for the voltage feedthrough. This diagram, modified from a standard vacuum power feedthrough design authored by the Kurt J Lesker Co. is the basis for a simple plasma gun. The central copper core is surrounded by a polyethylene cylinder and a grounded aluminum jacket.

Within the store of MCX vacuum hardware there exist several cylindrical electric feedthroughs as depicted in Fig. 6.2. A central metal pin is surrounded by a

polyethylene cylinder which is itself contained within an aluminum sheath, all of which has been mounted on a 2 3/4" flange. The central pin will be electrically connected to a legacy ignitron trigger chassis. The short kilovolt, kiloamp pulse produced by the chassis should create an arc across the polyethylene ring surrounding the central electrode. Installed at the midplane of the vessel, this breakdown event will be assisted by the magnetic field geometry which at this point is roughly parallel to the ignitor surface. The resultant discharge density should be proportional to the ablative arc current and be propelled by the pressure gradients into the confinement field. As this discharge breakdown across the electrode is assisted by the magnetic field, it may not be possible to bench test the system.

## 6.2 Scalings of MCX given present limitations

Without assuming that we are able to surmount the restriction imposed by the critical ionization velocity, the question still remains as to the alternate relevant parametric scalings. By examining the data set for values reasonably below the CIV limit we have been able to develop a set of guidelines which allow a projection of the MCX system into future iterations.

As the strongest scalings have been noted for variations in radial extent, we begin by envisioning an MCX system (MCX-II) which includes a midplane radial extent of 30 cm. As this design does not necessitate an alteration of the end regions, coils or power supplies the "shopping list" for MCX-II is limited to a new central

section for the vacuum vessel, a new set of midplane electromagnetic coils, and a high current power supply to replace the presently nonfunctional Spectromagnetics.

	MCX-I $B_{mid} = 0.24$ T $a = 0.2$ m	Parametric Scaling	MCX-II $B_{mid} = 0.5$ T $a = 0.3$ m
Plasma Voltage	4 kV	$V_P = v_{crit} * aB$ (Eqn 4-15)	13 kV
Plasma Resistance	5 $\Omega$	$R_P = 500a^3$ (Table 4-4)	15 $\Omega$
Momentum Confinement Time	400 $\mu s$	$\tau_m = 21807a^{2.5}$ (Figure 4.20)	1075 $\mu s$

Table 6.1: Projected performance parameters of MCX-II. The above table lists the results of the scaling from our present system to a future iteration. While the ability to surpass the CIV limitation is in no way assumed, if this were accomplished, the values in the final column could increase. However there is insufficient supporting data at this time.

Returning to the essentials of our performance rubric, we now examine the maximum plasma voltage, plasma resistance, and momentum confinement time which one might expect from this new system. The results of these scalings are summarized in Table-6.1. If this new set of magnets and power supply is able to generate a midplane field of 0.5 Tesla (a nominal increase from our current maximum of 0.38 T) then the maximum voltage of the discharge can be increased to nearly 13 kV before the CIV limitation is encountered. If we now re-examine the tau scaling that was noted in Section 4.5 we can see that for an initial input far below

the CIV limit (the 8 kV trace) The increase in radial extent being discussed here would result in a momentum confinement time of a full millisecond. In addition, for a similar data set (8 kV bank voltage) the plasma resistance is now greater than 10 Ohms.

The expected enhanced performance of MCX-II notwithstanding, we must acknowledge that even with these parametric scalings it would be extremely difficult to reach a projected MCX reactor point [21] if the Critical Ionization Velocity limit remains in effect.

### 6.3 Possible future physical limitations

As we increase the rotational velocity of the MCX system, it is likely that the discharge may become both supersonic and super-alfvénic. An Alfvén mach number ( $M_A = v_\phi/v_A$ ) of near or above unity suggests that extensive excursions from the vacuum magnetic field are possible thus leading to the presence of additional instabilities.

An examination of the Alfvén Mach limit begins with the Alfvén velocity, which is a measure of the speed of propagation of perturbations along the magnetic field line, and is defined as

$$v_A \equiv \frac{B}{\sqrt{\mu_0 \rho}} \quad (6.1)$$

where  $\rho = nM_i$

Thus we should be able to decrease the Alfvén Mach number by increasing the magnetic field. However, as we are unable to independently monitor the density, it must be inferred from the stored charge collected at the crowbar. This temporally limits our measurement of the plasma density, as well as subjecting it to the limits placed upon us by the failure of the crowbar ignitron at elevated bank voltages. Harking back to Section 4.2, the density which we compute from the current reversal, vacuum capacitance, and plasma voltage is

$$n \cong \frac{Q_P}{V_P C_0} \frac{B^2}{\mu_0 M_i c^2} \quad (6.2)$$

As such the Alfvén velocity reduces to

$$v_A = \frac{B}{\sqrt{\frac{Q_P B^2}{c^2 V_P C_0}}} = c \sqrt{\frac{V_P C_0}{Q_P}} = c \frac{C_0}{C_P} = \frac{c}{\epsilon_R} \quad (6.3)$$

This is recognizable as simply an alternate definition of the Alfvén velocity, given the transverse dielectric constant  $\epsilon_R$ . To ascertain if MCX displays a decrease in the Alfvén Mach number at elevated magnetic fields, we have parsed the data set in an attempt to locate a set of discharges which would allow for a "one to one" comparison across a scaling of the midplane field. The difficulty in this venture lies in both the incomplete crowbar data, due to the previously mentioned ignitron failure at large initial voltages, as well as a variability introduced by an inherent time history of the discharge subsumed within the current reversal.

The effective "stored charge" within the plasma, as recorded at the crowbar, is dependent upon the time of the crowbar, the plasma current, the voltage at the time of the crowbar, the series resistance, and the existence of an H-O transition within the discharge. Any comparison of crowbar data must match as many of these parameters as possible. Given these constraints we have located within the data a subset whereby a non-transitional H-type discharge was created for both standard and elevated midplane magnetic fields. These experiments were enacted under nearly identical conditions both before and after the replacement of the Spectromagnetics power supply. This is extremely fortuitous, as a minor variation in the applied midplane field enacted with the full Eratron system allows for the resolution of four separate data bands within Fig. 6.3.

The data presented shows that we are reasonably close to the Alfvén Mach limit. As such, any substantial increases to the rotational velocity obtained through a circumvention of the CIV, may quickly encounter this additional limitation. However the inverse scaling of the Alfvén Mach number with magnetic field demonstrates that we are not without recourse. Thus the detrimental effects caused by this alternate limit can be offset by a subsequent increase to the magnetic field.

However it must be stressed that the results from this preliminary data could be easily remanded by the implementation of an alternate and more robust measurement of the discharge density, which would allow us to decouple a measurement of the Alfvén Mach number from the plasma crowbar and attendant current reversal.

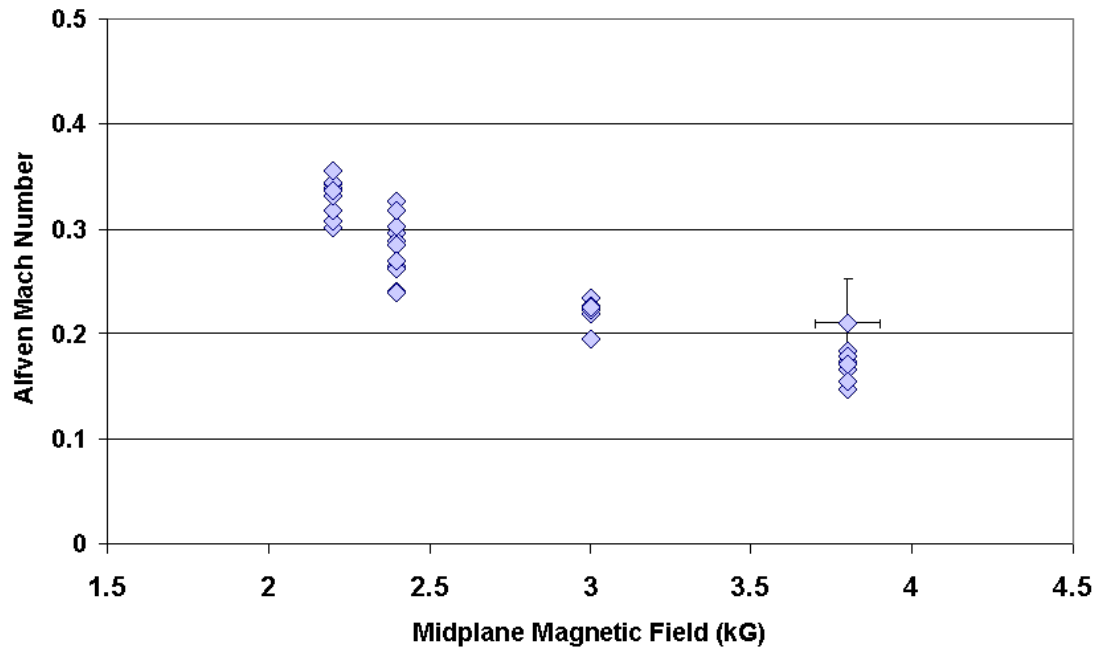


Figure 6.3: Scaling of the Alfvén Mach number with midplane magnetic field. The above data suggests that there does exist the ability to reduce the Alfvén Mach number through augmentation of the applied midplane magnetic field. However this data is extremely preliminary, and as such an independent density measure needs to be implemented before a firm conclusion can be reached.

## Chapter 7

### Conclusion

MCX creates a stable, fully ionized supersonic discharge which can be operated free from any large scale disturbances. We have demonstrated an understanding of the H-O transition process and have taken steps to eliminate its effects. As such the MCX discharge is capable of being run in an H-type mode for as long as the user wishes, provided there is sufficient input power.

However, having completed our mapping of the MCX parameter space, we are forced to concede that, at this juncture, the discharge appears to be velocity limited. In addition, the conditions of this limitation are consistent with Alfvén's theory of a Critical Ionization Velocity. This result is fully in agreement with the results of previous rotating plasma experiments [7, 31, 40, 12].

Unless a method can be found to mitigate the plasma-neutral interaction which leads to the CIV effect, the centrifugal confinement mechanism cannot be utilized as an fusion type confinement scheme. While simulation predicts that MCX will behave admirably once a sonic mach number of  $\sim 4$  has been reached, the CIV limit makes reaching this value extremely problematic.

Therefore, if the Maryland Centrifugal eXperiment is to continue as an inno-

vative confinement concept, extensive effort should be dedicated to the creation of an axially confined initial breakdown region. If such a structure can be affected, it is entirely possible that the externally applied electromagnetic forces will then be sufficient to enable a rapid supersonic rotation. This decoupled volume should then come fully under the auspice of the centrifugal confinement mechanism, perhaps allowing the volume discharge to remain isolated from the boundary interaction regions. In such a case, the conditions of the critical ionization velocity limit will no longer apply.

## Appendix A

### Centrifugally Confined Plasmas

The utilization of centrifugal forces to confine a highly magnetized plasma volume (also termed “gravitational confinement”) allows for a re-investigation of the classical open field line systems such as magnetic mirrors for fusion confinement. In the following sections, an overview of the basic tenants of the confinement scheme are detailed so as to illustrate the concepts for those not familiar with the major results.

#### A.1 Definition of Rotation Velocity

A charged particle in a strong magnetic field, in accordance with the Lorentz force law,

$$M \frac{d\mathbf{v}}{dt} = q\mathbf{v} \times \mathbf{B} \quad (\text{A.1})$$

will gyrate closely about a field line.

$$-qv_x B = M \frac{dv_y}{dt} = M \frac{d}{dt} \left( \frac{M}{qB} \frac{dv_x}{dt} \right) \quad (\text{A.2})$$

Thus resulting in cyclic particle motion as evidenced by

$$-\omega_c^2 v_x = \frac{d^2 v_x}{dt^2} \quad (\text{A.3})$$

where  $\omega_c = qB/M$  and we have assumed  $\mathbf{B} = B\hat{z}$ .

The subsequent application of a transverse electric field to the gyrating particle will result in an overall orbital drift which is perpendicular to both external fields. In the cylindrical geometry of MCX, where the magnetic field is applied axially and the electric field radially, this drift motion results in an azimuthal velocity with magnitude

$$v_\phi = \frac{\mathbf{E}_r \times \mathbf{B}_z}{B^2} = \frac{E}{B} = \frac{V}{aB} \quad (\text{A.4})$$

Where  $V$  represents the electrostatic potential drop across the ionized discharge and  $a$  is a measure of its radial extent. It is this averaged rotational drift velocity of the discharge which will be referred to when discussing the rotation speed of the plasma.

## A.2 Mirror Geometry

The energy of a magnetized rotating particle in the absence of potential fields can be written as

$$W = \frac{mv_{\parallel}^2}{2} + \frac{mv_{\perp}^2}{2} \quad (\text{A.5})$$

Where the  $\parallel$  and  $\perp$  subscripts represent directions parallel and perpendicular to the applied magnetic field. If we then roughly approximate the gyrating charged particle as a quantized current and examine the standard definition of the magnetic moment of a current loop we find that

$$\mu = IA \sim \left( q \frac{\omega_c}{2\pi} \right) (\pi r_L^2) = \frac{mv_{\perp}^2}{2B} \quad (\text{A.6})$$

Where  $r_L$ , the radius of a single gyration, also termed the Larmor radius is equal to  $v_{\perp}/\omega_c$ . Since magnetic fields can do no work,  $\mu$  is recognized as a conserved quantity. As such, an increase in the local magnetic field results in a commensurate rise in the perpendicular velocity. However, as the total particle energy must also be conserved, this increase in perpendicular velocity is offset by an opposing loss in parallel velocity. This leads to the magnetic mirror confinement scheme.

If a field could be created which had a higher flux density at the ends of the system as shown in Fig. A.2, theoretically the parallel velocity would slow enough that the particles would then be reflected back onto the main volume of the system. The condition under which the parallel velocity is small enough to allow this sort of reflection is  $v_{\parallel} \leq (R_M - 1)v_{\perp}^2$ , where  $R_M$  is the ratio of the magnetic field at mirror throat over the field located at the midplane.

Thus, there is a limitation on the maximum parallel velocity which can be confined by a magnetic mirror, giving rise to the creation of a section of velocity space termed the loss cone. Particles within this loss cone are found to exhibit a parallel velocity above this aforementioned limit and as such they are unconfined and able to exit the system on a sonic timescale. Thus the simple mirror is ineffective as a confinement device. The highly collisional nature of a fusion type discharge leads to the continual scattering of particles into this loss cone in velocity space, thus resulting in a highly significant loss of mass and energy from the confinement region

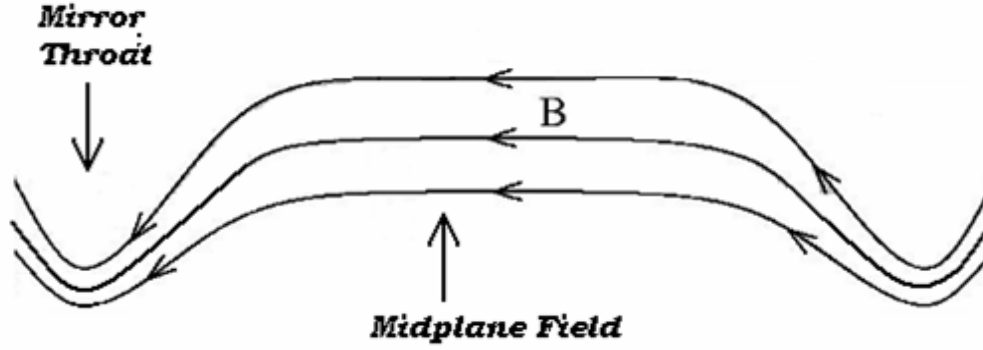


Figure A.1: This figure denotes a standard magnetic bottle configuration. Due to the conservation of magnetic moment, the transverse velocity of a particle trapped within this confinement scheme will be reduced as it enters the higher field regions. If this parallel velocity is small enough, the particle will be classically trapped within the system.

### A.2.1 Rotational closing of the loss cone

Applying a rotational motion to the mirror type system outlined in the previous section adds a centrifugal potential to the system. Assuming that field-parallel and drift motions are dominant, the Hamiltonian in the small larmor radius approximation then becomes

$$H = \frac{1}{2}Mv_{\parallel}^2 + \mu B - \frac{1}{2}MR^2\Omega^2 \quad (\text{A.7})$$

where  $R$  is the radial coordinate in an  $(R, \phi, Z)$  cylindrical coordinate system. Comparing the energies at the mirror maximum and minimum we find that the

threshold parallel velocity is now

$$v_{\parallel}^2 > \frac{2\mu B_{\min}}{M} \left( \frac{B_{\max}}{B_{\min}} - 1 \right) - \Omega^2 (R_{\max}^2 - R_{\min}^2) \quad (\text{A.8})$$

Recalling that the tangential drift velocity ( $v_{\phi} = \Omega R$ ) responsible for the plasma rotation is

$$v_{\phi(\min,\max)} = \frac{V}{a_{(\min,\max)} B_{(\min,\max)}} \quad (\text{A.9})$$

where we have assumed an equipotential along the field lines, we can then re-cast the above equation strictly in terms of the magnetic mirror ratio ( $R_M = B_{\max}/B_{\min}$ ) and the radial ratio ( $1/r_m = a_{\max}/a_{\min}$ ).

$$v_{\parallel}^2 > v_{\perp}^2 (R_M - 1) - v_{\phi}^2 \left( \frac{1}{R_M^2/r_m^2} - 1 \right) \quad (\text{A.10})$$

We note that the max and min in the radial ratio refer to maximum and minimum magnetic field, and not the respective radial distances. However the defined radial ratio has been cast in its more natural state. Field mapping of the elongated MCX system leads to the approximate relation that

$$r_m \sim \sqrt{R_M} \quad (\text{A.11})$$

Leaving us with the boundary condition as a function of the sonic mach number

$$v_{\parallel}^2 > v_{\perp}^2(R_M - 1) + M_s^2 v_{th}^2 \left( \frac{R_M - 1}{R_M} \right) \quad (\text{A.12})$$

The resultant effect on the loss cone can be seen in Fig A-2. The deepening of the effective gravitational well due to the rotation of the discharge allows retention of all but the most energetic particles.

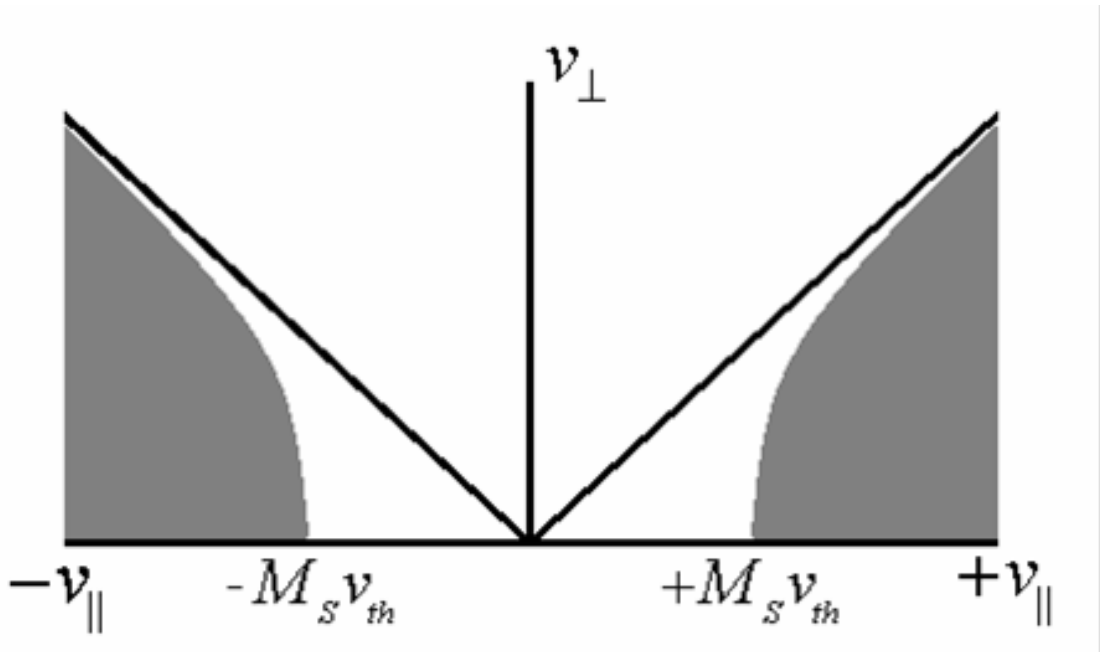


Figure A.2: The nominal mirror loss cone, the area below the diagonal lines, is reduced to the shaded region in the presence of rotation. Thus only highly energetic particles are able to exit the confinement scheme.

### A.3 Magnetohydrodynamics (MHD)

Highly collisional plasmas allow for the ability to treat the system not as a conglomerate of highly interactive individual particles, but as a charged fluid acted upon by a series of electromagnetic forces. It is within this model that we are able to fully illustrate the value of the centrifugal confinement scheme. Once we have shown that MCX operates within a mode which is consistent with the approximations made under MHD we then move on to an enumeration of the major results of centrifugal confinement theory.

#### A.3.1 Applicability of Magnetohydrodynamics

The cyclic motion of particles trapped on a field line creates a set of fundamental temporal and length metrics. Asserting the applicability of MHD requires that these values remain small when compared to plasma scale effects.

The amount of time that is required for a single gyro-orbit is the reciprocal of the particles gyrofrequency.

$$\tau_c = \frac{2\pi}{\omega_c} = 2\pi \cdot \frac{m}{|q|B} \quad (\text{A.13})$$

For MCX, which operates at a standard midplane magnetic field of between .2 and .3 Tesla this results in electron and ion gyroperiods in the range of

$$\tau_{ci} = 3.28 \times 10^{-7} \rightarrow 2.19 \times 10^{-7} \text{ s} \quad (\text{A.14})$$

$$\tau_{ce} = 1.79 \times 10^{-10} \rightarrow 1.19 \times 10^{-10} \text{ s} \quad (\text{A.15})$$

These quantities are considerably smaller than the observed discharge events which have been measured to occur on the microsecond to millisecond time scale. Likewise the radial extent of a gyration,  $r_L = v_\perp/\omega_c$  (termed the Larmor radius) serves as a yardstick for spatial structures. Noting that  $v_\perp = \sqrt{k_B T/m}$  and that typical MCX discharges possess ion temperatures ranging between 30 and 80 eV with maximum electron temperatures of roughly 10 eV, the resultant Larmor radii are

$$r_{Li} = \frac{\sqrt{k_B T_i m_i}}{qB} = 3.95 \times 10^{-3} \rightarrow 3.23 \times 10^{-3} \text{ m} \quad (\text{A.16})$$

$$r_{Le} = \frac{\sqrt{k_B T_e m_e}}{qB} = 3.77 \times 10^{-5} \text{ m} \quad (\text{A.17})$$

These quantities are also significantly smaller than their comparable MCX length scales, namely the midplane radial plasma extent of 20 centimeters. In addition the Debye length, a measure of the distance over which quasineutrality can be violated, which for a standard MCX density of  $n = 3.5 \times 10^{20} \text{ m}^{-3}$  is nominally

$$\lambda_D = \left( \frac{\epsilon_0 k_B T_e}{n e^2} \right)^{1/2} = 2.17 \times 10^{-6} \text{ m} \quad (\text{A.18})$$

Coupling this to a calculation of the estimated electron and ion collision rates [16] we find that for  $n_i \approx n_e \approx 3.5 \times 10^{20}$ ,  $T_i = 3T_e = 30 \text{ eV}$ , and  $\ln \Lambda \approx 10$  the collision

frequencies are

$$\nu_e = 2.91 \times 10^{-12} \frac{n_e}{T_e^{3/2}} \ln \Lambda = 3.22 \times 10^8 \text{ sec}^{-1} \quad (\text{A.19})$$

$$\nu_i = 4.8 \times 10^{-14} \frac{n_i}{T_i^{3/2}} \ln \Lambda = 1.02 \times 10^6 \text{ sec}^{-1} \quad (\text{A.20})$$

Which result in collisional time scales on the order of

$$\tau_i = \frac{1}{\nu_i} = 980 \text{ ns} \quad (\text{A.21})$$

$$\tau_e = \frac{1}{\nu_e} = 3 \text{ ns} \quad (\text{A.22})$$

and a mean free path of

$$\lambda_i = \frac{v_{T_i}}{\nu_i} = \left( \frac{2k_B T_i}{M \nu_i^2} \right)^{1/2} = 74 \text{ mm} \quad (\text{A.23})$$

$$\lambda_e = \frac{v_{T_e}}{\nu_e} = \left( \frac{2k_B T_e}{M \nu_e^2} \right)^{1/2} = 5.8 \text{ mm} \quad (\text{A.24})$$

Thus the plasmas created in MCX are magnetized, highly collisional, quasineutral systems which exist for times long when compared to a gyroperiod, and one can conclude that the single fluid magnetohydrodynamic (MHD) theory is applicable to the MCX discharge.

### A.3.2 Centrifugal Confinement

Having established that the MCX plasma is within the bounds set forth by magnetohydrodynamic theory, we examine the governing equations to determine the theoretical behavior of an ideal MCX discharge. The MHD equilibrium equation for

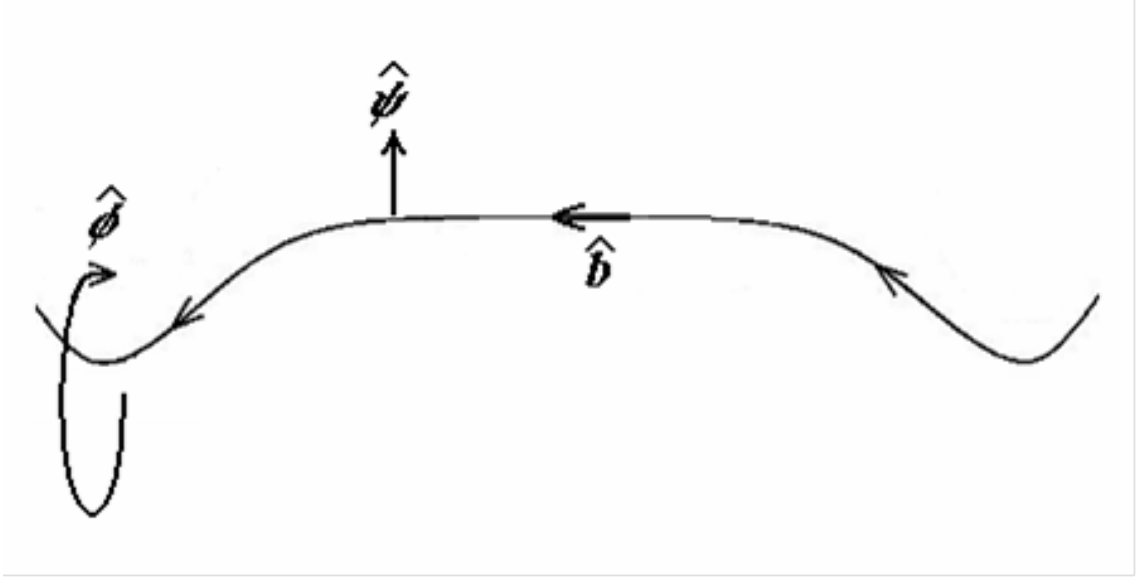


Figure A.3: The above definitions of the coordinate axis will be used to examine the MHD equilibrium state.

the MCX system is

$$nM \left( \frac{\partial \mathbf{u}}{\partial t} + \mathbf{u} \cdot \nabla \mathbf{u} \right) = -\nabla p + \mathbf{j} \times \mathbf{B} - nM (\nu_{in} \mathbf{u} - \mu_{\perp} \nabla^2 \mathbf{u}) \quad (\text{A.25})$$

Examining the components of this equation in the coordinate system outlined in Fig.A-3 we find that, in the radial direction

$$nM (\mathbf{u} \cdot \nabla \mathbf{u})_{\psi} + \nabla p_{\psi} = (\mathbf{j} \times \mathbf{B})_{\psi} - nM \nu_{in} u_{\psi} \quad (\text{A.26})$$

If we assume that there is minimal radial flow ( $u_{\psi}/u_{\phi} \ll 1$ ) allowing us to neglect the final term, and recall that  $\mathbf{u} \cdot \nabla \mathbf{u} = \nabla(R^2\Omega^2/2)$ , we can then recognize that the poloidal current balances the centrifugal force as well as the radial pressure profile, as shown by

$$j_{\phi} B = \frac{nMR^2}{2} \nabla_{\psi}(\Omega^2) + \nabla_{\psi} p \quad (\text{A.27})$$

Examining the balance in the azimuthal direction we find that

$$nM \left( \frac{\partial \mathbf{u}}{\partial t} + \mathbf{u} \cdot \nabla \mathbf{u} \right)_\phi = -\nabla_\phi p + (\mathbf{j} \times \mathbf{B})_\phi - nM \left( \nu_{in} - \frac{\rho_i^2 \nu_{ii}}{a^2} \right) u_\phi \quad (\text{A.28})$$

As we expect that a (symbol) periodic translation about this axis will not have an effect on the equilibrium dynamics of the system we can omit the full right hand side as well as the pressure term on the left hand side. Thus the remaining terms show that the radial current will balance the angular momentum lost due to neutral friction and viscous forces.

$$(\mathbf{j} \times \mathbf{B})_\phi = j_\psi B = nM \left( \nu_{in} - \frac{\rho_i^2 \nu_{ii}}{a^2} \right) u_\phi \quad (\text{A.29})$$

Performing a volume integral on both sides of this equation and recognizing that  $\nu_{in} - \rho_i^2 \nu_{ii}/a^2 = \tau_\perp^{-1}$  leads to

$$B \int_{Vol} j_\psi d^3x = I_p B = \frac{NM u_\phi}{\tau_\perp} \quad (\text{A.30})$$

Taking dot product of our initial equation with respect to the magnetic field allows us obtain the force directed along the field line.

$$\mathbf{B} \cdot nM \left( \frac{\partial \mathbf{u}}{\partial t} + \mathbf{u} \cdot \nabla \mathbf{u} \right) = -\mathbf{B} \cdot \nabla p + \mathbf{B} \cdot (\mathbf{j} \times \mathbf{B}) - nM \mathbf{B} \cdot \left( \nu_{in} \mathbf{u} - \mu_\perp \nabla^2 \mathbf{u} \right) \quad (\text{A.31})$$

Assuming equilibrium and that  $u_b/u_\phi \ll 1$ , leaves only one term on each side

$$nM \mathbf{B} \cdot (\mathbf{u} \cdot \nabla \mathbf{u}) = -\mathbf{B} \cdot \nabla p \quad (\text{A.32})$$

again noting that

$$\mathbf{u} = R\Omega \hat{\phi} \quad (\text{A.33})$$

$$\mathbf{u} \cdot \nabla \mathbf{u} = R\Omega^2 \nabla R = -\nabla \left( \frac{R^2 \Omega^2}{2} \right) \quad (\text{A.34})$$

Assuming an isothermal flux surface ( $p = nT$ ) results in

$$\frac{\mathbf{B} \cdot \nabla n}{n} = \frac{M}{2T} \mathbf{B} \cdot \nabla (R^2 \Omega^2) = \mathbf{B} \cdot \nabla \left( \frac{R^2 \Omega^2}{2c_s^2} \right) \quad (\text{A.35})$$

for a sound speed  $c_s = \sqrt{T/M}$ . From this we can remove a density profile

$$n(\psi, R) = n_0(\psi) \exp \left\{ \frac{1}{2} \frac{R^2 \Omega^2}{c_s^2} \right\} \quad (\text{A.36})$$

The ratio of pressures at different points along a field line ( $R_1$  at Mirror Throat and  $R_2$  at Midplane) is thus shown to be

$$\frac{p_2}{p_1} = \exp \left[ \frac{1}{2} \frac{(R_2^2 - R_1^2) \Omega^2}{c_s^2} \right] \quad (\text{A.37})$$

If we then define the sonic Mach number as  $M_s = \frac{v_\phi}{c_s} = \frac{R\Omega}{c_s}$ , we arrive at a scaling for the pressure ratio.

$$\frac{p_2}{p_1} = \exp \left[ \frac{M_s^2}{2} \left( 1 - \frac{R_1^2}{R_2^2} \right) \right] \quad (\text{A.38})$$

Therefore arrival at the largest pressure differential, indicating strong centrifugal confinement, would require both substantial sonic Mach number as well as an extensive system aspect ratio.

### A.3.3 Plasma Resistance Model

One of the major measureables utilized to determine discharge performance in MCX is the effective plasma resistance. This empirical measurement is taken by assuming an ohmic system and dividing the discharge voltage by the recorded axial current as outlined in section 3.7. The question then arises as to whether this

measurement is actually close to the theoretical models of the assumed discharge resistance.

Beginning from the steady state fluid equation, in order to offset viscous losses within the discharge, power must be continually resupplied into the system as shown by

$$\frac{NMu_\phi^2}{\tau} = I_P V_P \quad (\text{A.39})$$

Here  $N = n \times Vol$  and  $u_\phi$  is the standard rotation velocity. From this we are able to determine that

$$V_P = I_P \left( \frac{a^2 B^2}{n \cdot Vol \cdot M_i} \right) \tau \quad (\text{A.40})$$

Again assuming an ohmic discharge, we are able to conclude that, for a cylindrical plasma of length 1.5 meters, with an inner and outer radius  $a_i = 26$  cm and  $a_o = 6$  cm respectively, and a nominal ion density and magnetic field, the plasma resistance is

$$R_P = \left( \frac{a^2 B^2}{nM} \right) \left( \frac{1}{\pi(a_o^2 - a_i^2)L} \right) \tau \quad (\text{A.41})$$

$$= \left( \frac{0.2^2 \cdot 0.24^2}{3.5 \times 10^{20} \cdot 1.67 \times 10^{-27}} \right) \left( \frac{\tau}{0.3016} \right) \quad (\text{A.42})$$

$$= 1.3 \times 10^4 \cdot \tau \quad (\text{A.43})$$

As such, the theoretical value of the plasma resistance depends wholly on the assumptions that are made for the momentum confinement time. If we were to insert a nominal measured momentum confinement time of  $\sim 300 \mu\text{s}$ , this results in an approximate plasma resistance

$$R_{P \text{ (experimental)}} \cong 3.9 \Omega \quad (\text{A.44})$$

as is consistent with observations. If however, we assume a classically diffusive model, we arrive at

$$\tau = \frac{a^2}{D_{\perp}} \text{ and } D_{\perp} = \frac{2nk_{\text{B}}T\eta_{\perp}}{B^2} \cong 6.4 \times 10^{-1} \frac{\text{m}}{\text{s}} \quad (\text{A.45})$$

giving a theoretical plasma resistance of

$$R_P \text{ (diffusive)} \cong 800 \, \Omega \quad (\text{A.46})$$

This is roughly 200 times larger than the standard plasma resistance, thus suggesting that we are not operating a simply diffusive system.

Assuming that charge exchange is the dominant system loss mechanism leads to [43]

$$\tau = \frac{1}{n_0\sigma_{\text{cx}}v_i} \quad (\text{A.47})$$

Taking  $\sigma_{\text{cx}} = 4 \times 10^{-19} \text{ m}^2$  from the literature [27] and  $n_0 \cong 1 \times 10^{19} \text{ m}^{-3}$  from measurements of the  $\text{H}_{\alpha}$  intensity [17], for a marginally supersonic discharge we find

$$\tau = \frac{1}{4v_{\phi}\sqrt{1 + 1/M_s^2}} = 2.4 \times 10^{-6} \text{ s} \quad (\text{A.48})$$

This predicts a resistance of

$$R_P \cong 3.2 \times 10^{-2} \, \Omega \quad (\text{A.49})$$

which is about 100 times lower than our measured resistance. This result is also not surprising, as we surmise that the discharge should be impermeable to neutrals past a penetration skin depth, and therefore charge exchange, at the densities recorded by the line averaged  $\text{H}_{\alpha}$  measurement will not be active over the entire radial profile, but will be much lower in the core of the discharge.

### A.3.4 Neutral Penetration

Present on the inner and outermost flux surfaces there exists an strong interaction region between the fully ionized plasma at the core of the discharge and the surrounding neutral gas blanket. An estimation of the penetration depth of a hot neutral into the edge of an dense plasma has been shown [27] to be

$$L_n = \frac{v_n}{n_e \langle \sigma_i v_e \rangle} \quad (\text{A.50})$$

Where the average ionization rate  $\langle \sigma_i v_e \rangle$  created by 10 eV edge electrons is approximately  $10^{-14} \text{ m}^3\text{s}^{-1}$ . In addition we set an upper bound on the velocity of a hot neutral by assuming that it has roughly thermalized with our 15 eV edge discharge temperature and can therefore be approximated by  $v_n = \sqrt{2k_B T / M_n} \cong 54 \text{ km/s}$ . Thus the penetration depth of the neutral is

$$L_n = \frac{5.4 \times 10^{18}}{n_e} \quad (\text{A.51})$$

For a quasi-neutral discharge ( $n_i \cong n_e$ ), our nominal fully ionized plasma possesses a neutral penetration depth of

$$L_n = \frac{5.4 \times 10^{18}}{3.5 \times 10^{20}} = 1.54 \text{ cm} \quad (\text{A.52})$$

The above equation also allows an estimation of Lehnert's minimum density [39], a condition which sets a limit, below which the volume of the discharge becomes fully permeable to neutral penetration. In the present MCX system, a plasma width of 20 cm will become fully permeable when the density drops below.

$$n_i \cong n_e \leq \frac{5.4 \times 10^{18}}{0.1} = 5.4 \times 10^{19} \text{ m}^{-3} \quad (\text{A.53})$$

Though not regularly approached, a discharge of this density is possible at the reduced fill pressures enumerated in section 4.2.

As an alternate to the immediate electron ionization previously detailed, it is possible that upon incursion into the plasma, that the neutral could perform a charge exchange with the impact ion. In such a case, the newly created hot neutral would be able to penetrate further into the discharge. The extent to which this increases the overall neutral presence within the discharge is given by the charge exchange depth. Consistent with our previous assumptions of a thermalized neutral, a standard ion density and a charge exchange cross section of  $\sigma_{\text{cx}} \cong 4 \times 10^{-19} \text{ m}^2$ , a charge exchange length of

$$L_{\text{cx}} = \frac{v_n}{n_i \sigma_{\text{cx}} v_{T_i}} = 0.7 \text{ cm} \quad (\text{A.54})$$

is found to augment our previous ionization length, thus allowing a significant neutral penetration into the plasma of approximately 2 cm on both the inboard and outboard sides. However as this length is still much smaller than the radial extent of the discharge we can confidently assert that the interior of the discharge is fully ionized and thus consistent with the calculated neutral density found in Eqn. (4.6).

#### A.4 Energy Confinement

Without further diagnostics, it is impossible to conclusively determine the energy loss channels, and thus the energy confinement time ( $\tau_E$ ) of the discharge. However there are several assumptions that can be made which will allow us to

determine the most probable mechanisms limiting the energy confinement of MCX.

We can give a rough estimate of the energy confinement time by examining the input power of the discharge and determining the amount of time required to replace the plasma's rotational stored energy. The order of magnitude estimate performed in Section 3.2.1 (Eq 3.3) shows the kinetic energy of a nominal H-type discharge to be  $W_i \approx 850J$ , and examining the Plasma Voltage and Current traces displayed in Figure 3-1, we estimate the average input power during the quiescent H-mode ( $t = 2ms$  to  $t = 3.5ms$ ) to be approximately  $P_{in} = 5.6MW$ . As such it takes

$$\tau_E = \frac{(W_i * .68)}{P_{in}} \approx 100\mu sec \quad (A.55)$$

to replace 68% of the stored energy of the discharge(the nominal e-folding time). This of course assumes that the entirety of the input power is utilized for discharge replenishment and that there are no alternate power sinks, the existence of which would increase our estimate of the energy confinement time.

#### A.4.1 Energy Loss Mechanisms

Any of the mechanisms responsible for the loss of momentum within the discharge can also be viewed as channels by which energy within the plasma can be dissipated. We briefly mention several of the loss channels as well as the possible diagnostics which could be implemented in an attempt to determine the efficiency of the loss mechanism.

The existence of turbulence, specifically convective cells and MHD instabilities leads to elevated plasma transport. This increase in diffusion pulls energy from the hot core of the discharge to the cooler edge regions where recombination and charge exchange are more likely to occur. The implementation of magnetic probe diagnostics should increase our understanding of the behavior of the internal regions of the discharge thus allowing a quantification of these effects.

Energy losses due to recombination of the ions and electrons is evidenced by the strong Hydrogen emissions recorded throughout the duration of the discharge. However, to fully determine the energy fraction lost through this channel, we would need to extend the range of our present diagnostics into the IR as well as the UV, and record the radiation at several locations. This would allow an estimate of the full radiative emission of the discharge, and thus the energy lost.

The collision of a hot ion with a neutral can often result in a process termed "charge exchange" whereby the ion captures the electron from the neutral resulting in a colder ion and a now unconfined hot neutral. As the neutral particle is no longer affected by the magnetic field, it is able to rapidly exit the discharge leading to a net loss of energy. This also leads to a net momentum loss. As such, variations within the momentum confinement time should allow insight into the strength of this mechanism. The emission from these hot neutrals could be monitored by a radially resolved photodiode array, thus allowing neutral profile and penetration information to be extracted from the discharge.

As centrifugal confinement is marginal at the mildly supersonic rotation velocities currently present within MCX, there is still substantial particle loss along the axis of the magnetic mirrors. In addition, as the particles populating the loss cone are likely to be more energetic, they represent a disproportionate energy loss. Were MCX operated as a spatially limited discharge (through plasma jet injection) the existence of energetic particles at the bounding insulators would be sufficient to determine the extent of this loss mechanism. At present however, the insertion of intrusive diagnostics at the terminal insulators to monitor particle loss would most likely create an adverse effect on the volume discharge due to the strong plasma-neutral boundary interactions.

#### A.4.2 Field Parallel Electron Transport

Given the relative abundance of various impurity ionization states within the MCX discharge, we can estimate the electron temperature at approximately 6 eV. Thus the thermal speed of the electrons is

$$v_{th}(e) = \sqrt{\frac{kT}{m_e}} = 1.03 \times 10^6 \text{ m/sec} \quad (\text{A.56})$$

Which, given that the  $E \times B$  rotation velocity is species independent results in a sonic Mach number of

$$M_s(e) = \frac{v_\phi}{v_{th}(e)} = .08 \quad (\text{A.57})$$

As the centrifugal confinement mechanism scales strongly with the sonic mach number, it becomes evident that the electrons are unconfined by this method. Electrons will free stream along the field lines until an electrostatic potential is generated which inhibits further transport. However, if this electron recombines with an edge ion, or is absorbed by the walls or the insulators, it creates an imbalance which allows further electron transit from the discharge. Thus a current is created out of the ends of the magnetic mirror which serves as an energy loss channel.

An energized electron reaching the terminal sections of the discharge will experience a rapid deceleration resulting in the emission of Bremsstrahlung radiation. This effect could be very efficient in the transmission of energy from the discharge, and would be expected throughout the duration of the plasma's existence.

If we assume that the majority of an escaping electron's thermal energy is converted into electromagnetic radiation, then one could expect a radiative peak at

$$\lambda_{Brem} = \frac{ch}{E_i} = 247nm \quad (\text{A.58})$$

Where  $c$  and  $h$  are the speed of light and Planck's constant respectively, and the electron energy  $E_i$  is in joules. Note that this does not account for those electrons which have collisionally thermalized with the ions, thus containing a higher energy

and generating an emission which is located further into the ultraviolet portion of the spectrum.

The implementation of a broadband ultraviolet diagnostic at the terminal sections of the discharge would allow us to resolve this emission, and determine the extent to which it serves as an energy loss channel.

In addition, it also may be possible that the continuum of light emission for the transitional discharge, as displayed in Figure 3.8 is the result of just such an effect. The breakdown of the end regions during an O-Mode would provide a continuous current path for the escaping plasma electrons thus leading to the broad emission signature, one which may continue beyond the resolution limits of the current spectrometer. However, without further diagnostics, this is still firmly entrenched within realm of conjecture.

## A.5 Presence and importance of Velocity Shear

The inner and outer flux surfaces in the MCX discharge are expected to be subject to no-slip boundary conditions at the core and vessel wall respectively due to the elevated neutral density and attendant drag upon plasma flow. Coupling this estimation with a confirmed rotation of the volume discharge leads to the conclusion that the poloidal rotation of the bulk plasma is subject to a velocity stratification which will create a differential rotation between flux surface layers. This gives rise to a shearing effect within the discharge which we expect to lead to a suppression of

the interchange instabilities normally associated with open field line configurations.

In this section we note the primary theoretical results of the velocity shear stabilization of a centrifugally confined plasma and refer the reader to the collected evidence which indicates that shear, at a level sufficient to effect this stabilization, is present in the MCX system.

### A.5.1 Velocity Shear suppression of Magnetohydrodynamic instabilities

There exist four major instabilities which could have an effect upon the MCX discharge. These are subdivided into high and low magnetic beta ( $\beta = 2\mu_0 p/B^2$ ) instabilities. The flute (Rayleigh-Taylor) and Kelvin-Helmholtz instabilities could both become problems in the low  $\beta$  regime, while the Parker instability as well as the Magneto-rotational instability (MRI) could surface in the high  $\beta$  limit.

The Rayleigh-Taylor instability is derived from an interchange of magnetic flux tubes. A hot flux surface, internal to the discharge, can be exchanged with a cold flux surface on the edge of the ionized region. This releases the stored gravitational potential energy of the earlier configuration, resulting in a loss of temperature and momentum. As these flute type interchanges can be driven by both a pressure gradient in a curved magnetic field as well as a density gradient acted upon by a magnetic force it could be expected that a rotating mirror system would be especially prone to these type of instabilities. However the interchange growth rate [34] for an

effective gravitational force  $g \sim c_s^2/R_c$

$$\gamma_g = -R\Omega^2 \frac{n'}{n} - g \frac{p'}{p} \quad (\text{A.59})$$

has been shown [28] to be stabilized for a velocity shear of magnitude

$$R_c^2 \Omega'^2 \geq \gamma_g^2 \ln R_u \quad (\text{A.60})$$

where  $R_u$  is the magnetic Reynolds number and  $R_c$  is the radius of curvature of a field line. A computational test of this velocity shear stabilization was performed [33] in which a centrifugally confined plasma was shown to maintain a laminar state over many interchange growth times. As an explicit test of the velocity shear mechanism, the shear term in the governing equations was artificially turned off. Running the simulation in this state resulted in turbulence evident throughout the system. After such time as the plasma had become wholly turbulent, the velocity shear was turned back on. The result was a near complete return to the previously laminar state.

That being said, the velocity shear which stabilizes the interchange mode may give rise to the growth of a Kelvin-Helmholtz type instability, whereby the interface between two differentially rotating surfaces will undulate as a result of the contact. This instability would be driven as long as there is sufficient velocity shear, possibly to the extent of forming turbulent convective cells such as the so called ‘‘Cat’s Eye’’ vortex. However, if the generalized Rayleigh’s inflexion theorem is satisfied, namely

$$\frac{d}{dr} \left( \frac{\rho}{r} \frac{d}{dr} (r^2 \Omega) \right) \neq 0 \quad (\text{A.61})$$

then the system has been shown [30] to be ideally stabilized to Kelvin Helmholtz modes.

The magneto-rotational instability, which results in an anomalous transport of angular momentum requires an outwardly decreasing differential rotation, as well as a weak magnetic field to become a substantial factor, these requirements result in a stability condition whereby

$$\phi^2 \frac{r}{a} > \frac{v_\phi^2}{v_A^2} \quad (\text{A.62})$$

However as a strong magnetic field is essential for an effective centrifugal confinement, it is not expected that MCX will operate in a regime where the MRI can destabilize the system.

Finally, far from being a destabilizing influence, calculations have shown [34] that the resultant clumping of the Parker instability could actually enhance the centrifugal confinement effect

### A.5.2 Multi chord spectroscopic confirmation of velocity shear

While the utilization of spectroscopic measurements to confirm discharge rotation has been present on MCX nearly since its inception [24, 26], the ability to discern differential rotation within the radial profile of the discharge [25] is a recent development.

In place of the single chord measurements reported in Section 2.6.4 the spectrometer has been upgraded to a multi-component system whereby an array of 5 fibers is stacked radially. These five fibers are therefore focused on separate zones of the discharge and by deconvolving the data recovered from these fibers by utilizing

an Abel-type inversion, differential shear between the layers can be resolved. It was determined that the flow velocity shear exceeds the nominal interchange instability suppression figure by up to a factor of 9. Thus the velocity shear recorded on MCX, is nearly an order of magnitude larger than that necessary for suppression of the flute type modes. In addition, these shear measurements have all been performed in an HV type mode, thus obviating the necessity to access the elusive HR mode in order to achieve stabilization. It is assumed, that were supercritical ionization velocities possible, greater instability suppression factors could be achieved.

## Appendix B

### Experimental Vessel and main power supplies

This appendix contains a detailed description of the primary experimental chamber of the Maryland Centrifugal eXperiment. Attendant to this is also a brief description of the power supplies responsible for generation of the electric and magnetic fields upon which the discharge depends.

#### B.1 Vessel Dimensions and Description

The primary experimental chamber for the Maryland Centrifugal Experiment is a multi-piece, roughly cylindrical vessel, fabricated from 304 stainless steel. (Dimensions will be expressed in inches to ensure compatibility with the mechanical drawings of record) The assembly is comprised of three distinct subsections. The central portion, as denoted in Fig. B.1 is a fully cylindrical section which possesses of a 22 inch diameter and a 79 inch length. This central section is mated to the pair of end regions by means of a standard bolt circle with enclosed rubber O-ring ensuring a vacuum seal. These end regions are a pair of smaller, identical cylinders with a 14 inch diameter and 41 inch length which terminates in a standard 16 inch conflat flange with attendant copper gasket. When fully assembled, the vessel pos-

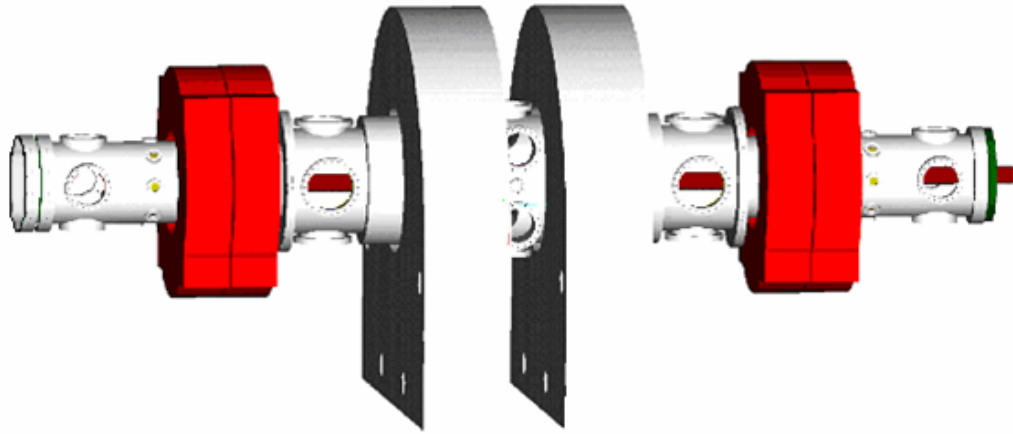


Figure B.1: The cylindrical object in the above diagram is a mechanical drawing of the MCX experimental vessel. The red disks at either end are representative of the mirror field coils, while the larger grey objects at the midplane are the MS-coils and create the roughly solenoidal field in that region.

sesses a 162 inch longitudinal length. Note that these dimensions, especially those given for the diameters of various sections, are only approximate and not intended as a precision measurement. This disclaimer is necessary due to the unfortunate circumstance that sections of the chamber are not perfectly round as a result of manufacturing irregularities.

Placed at various locations along the outer wall of the experimental chamber are sets of conflat flanges ranging in diameter from 2-3/4" to 12" to allow diagnostic access to the plasma. Finally, traversing the center of the long axis of this cylinder is a smaller stainless steel tube which is commonly referred to as the 'core'. Note that the symmetry of the system about the midplane is broken by the unilateral

penetration of the core from what is termed the “high voltage end”.

During a discharge, the core is biased to a negative voltage with respect to the grounded outer walls of the vessel by means of a capacitor bank. We are able to attain an initial bank voltage ranging from 5 to 20 kV thus creating the electric field required for both plasma ionization and bulk rotation. Lower voltages are possible, however they have been deemed insufficient for the creation of a fully ionized volume breakdown and thus do not lead to a favorable discharge parameter space.

## B.2 Capacitor charging power supply

The voltage to the core is provided by a multi-element capacitor bank with associated discharge circuit as described in Ch 2. Prior to firing, the bank is charged to the requisite voltage by a General Atomics CCS negative polarity power supply. The supply is neither a constant voltage source nor a constant current source, but a constant power source. It is capable of sourcing 8 kJ/sec into the charging circuit and associated capacitors, however it is not designed nor intended to solely sustain the plasma as is it not able to compensate for the rapid changes in operational voltage associated with a discharge event. In fact, rapid changes to the load conditions on the power supply could lead to irreparable damage to the output rectifiers.

To ensure the safety of the power supply, a standard operational procedure has been adopted. During an operational run, a safety dump switch is first raised. This action disconnects the center pole of the capacitors from earth ground allowing

them to be charged to the desired level. After this a charging switch which connects the power supply to the capacitor bank is closed. These operations as well as concurrent machine operation are all performed through a graphical interface within the Labview VI *Switch Control and Monitoring* located on the MCX control computer. As a final step the power supply remote interlock is engaged which allows the power supply to enter a high voltage state. At present, the user is then required to walk into the experimental area to physically engage the high voltage power supply. This action is required due to the grounding problems present within the building. When last attempted, the power supply could not be reliably controlled completely by remote, thus creating the need for the user interface.

Having engaged the high voltage mode, the user is then able to exit the experimental area as the charging cycle can be remotely terminated. At the completion of the cycle the power supply is taken out of high voltage mode by opening the power supply remote interlock and the charge switch is raised. This completely removes the power supply from the discharge circuit. At this point, the system is ready to initiate a discharge. Failure to follow this course of events could result in extensive damage to the power supply as well as the attendant diagnostic system leading to a possibly dangerous situation.

As an additional precaution, a resistor and diode bridge has been installed along the charging line connecting the capacitor bank to the power supply . This safety network is in place as a redundant protection for the power supply, as suggested by the manufacturer. When operated correctly, the most probable failure

mode within the charging system is the internal failure of a single capacitor, thus providing a short to ground. Should this occur, the remainder of the bank would be rapidly discharged through this short. The diode attached to the charging line is installed in an attempt to ensure that this extreme change in voltage will not damage the output rectifiers of the power supply.

### B.3 The Vacuum Magnetic Field

The magnetic field for MCX is created by 3 sets of magnetic coils external to the vessel as shown in Fig B-1. The central coil pair creates a roughly solenoidal field through the midplane region which can be varied from 1 to 3.8 kGauss, while pairs of coils at the diametric ends of the machine are responsible for the 1.8 Tesla mirror field. The mirror field can also be varied, however it is usually directed to the higher end of the range for performance reasons. We define the quotient of the end line magnetic field over the central field as the mirror ratio( $R_M$ )

Originally the Maryland Centrifugal eXperiment was designed to operate with a pair of independent power supplies for the solenoidal and mirror field sections. However, during May of 2006, the power supplies driving the midplane field failed in an irreparable manner. In order to continue to operate the MCX experiment, alterations had to be made to the magnet setup. These alterations entailed driving all of the magnet coils off of a single power supply, referred to as the Eratron. The data within this dissertation subsumes this transition however, as will be enumerated,

efforts were undertaken to maintain continuity between the old and new systems, thus allowing comparisons to be made between the data sets.

### B.3.1 Midplane and Mirror Coil Description

In the center of the magnetic topology there is an approximately solenoidal region which extends for  $\pm 30$  cm from the axial midpoint of the vessel. The electromagnets responsible for this field are an identical pair of 200 layer  $\times$  3 turns/layer freestanding coils. These coils, commonly referred to as the MS coils have individual series resistances of  $.35 \Omega$  and are at present not actively cooled. The elevated field region, is formed by identical sets of what are referred to as the O-coils. (the etymology of which is derived from their originally orange color, present appearances to the contrary notwithstanding) Each set is comprised of two coils, and each of the four coils is water cooled and possesses of a resistance of  $.043 \Omega$

As previously mentioned, all of these coils are being driven by a single power supply, and are connected as show in Fig. B.3.1. The output of the Eratron is a 7 second pulse, of which the first 6 seconds are dedicated to a ramp up of the current to the desired level, leaving a 1 second flat top in which the discharge is activated. This pulse width has been determined as an optimal balance between a pair of competing influences. While it would be beneficial to minimize the pulse width to mitigate the heating effects both within the magnets as well as within the additional resistor, we

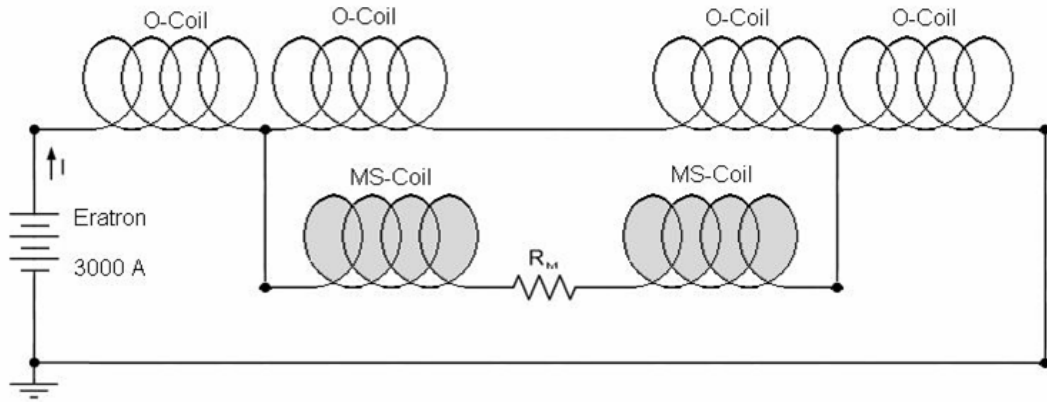


Figure B.2: The solenoidal midplane coils (MS coils) are shown in grey connected in parallel with two of the mirror coils (O-coils) and in series with an additional balancing resistor ( $R_M$ )

must also attempt to minimize the mutual effects of these highly inductive circuit elements, and thus should moderate  $dI/dt$  as much as possible. This 7 second pulse length is the result of this balancing.

### B.3.2 Implementation of an additional midplane resistor

In addition to the electromagnets, the circuit also contains a balancing resistor ( $R_m$ ) which allows the user to determine the amount of current which the MS Coils will receive. This additional resistance allows the user to tune the mirror ratio of the system by a restriction of current through the midplane field circuit branch.

Prior to the incident which claimed the Spectromagnetics power supply, there were two distinct modes in which MCX was primarily operated. In the nominal

lower field mode, values at the midplane were 2.26 kG with a mirror ratio of 7.8 and in the higher field mode, operational values were 3.5 kG on the midplane with a mirror ratio of 5. Post-incident it was within or best interest to create a system whereby these values were once again attained, or at least closely approximated. As the midplane coils generate approximately 12 Gauss/Amp this would require approximately 160 Amps for the lower field and 230 Amps for the higher field. (Note that the MS coil currents do not account for the full midplane field as a significant portion of the field in that region is generated by the 1.8 T coils at the mirror throat) We are able to achieve this by balancing the circuit with the additional resistance ( $R_m$ ). By approximating the current through the MS coils we are able to solve for the value of the additional resistance required in the circuit.

$$V = I_{MS}(2R_{MS} + R_M) = I_0 \cdot 2R_0 = (I_T - I_{MS})2R_0 \quad (\text{B.1})$$

$$R_m = 2R_0 \left[ \frac{I_T}{I_{MS}} - 1 \right] - 2R_{MS} \quad (\text{B.2})$$

Where  $I_T$  is the total current and  $R_{MS}$  and  $R_O$  are the MS coil and O coil resistances and  $I_{MS}$  and  $I_O$  are the respective currents. This rough calculation leads to additional resistance values of between 1/4 and 1 Ohm.

It should be noted that these resistors will also need to dissipate a great deal of power as the currents through them will be several hundred amps at a potential of several hundred volts. To that end we have utilized the same type of non inductive bulk ceramic resistors which comprise our current limiting series resistance in the

discharge circuit. Using a similar mounting method, we have constructed a system whereby  $R_M$  can be easily adjusted from 0 to 1 ohm in 1/4 Ohm steps. The results of a test of this system at these various resistance values can be found on the following tables.

### B.3.3 Magnetic Field Tables for varied Midplane Resistors

The values stated in the following tables are measurements taken with a Bell 9600 Gauss Meter as recorded on a standard oscilloscope. Though not explicitly included with the tables, we note that the heat load on the additional resistance is at points, extreme. Even though the additional resistance is comprised of at least several Kilowatt rated resistors, the temperature rise over the 7 second pulse is, for maximum load, as high as 50 degrees Fahrenheit. For this reason the resistor array is being actively air cooled and the interval between successive discharges has been set to no less than 5 minutes.

Eratron Control Voltage	Total Current (Amps)	Mirror Field (kG)	Midplane Field (kG)	Mirror Ratio
0.5	288	1.8	0.42	4.29
1	648	3.8	0.87	4.37
1.5	960	5.7	1.31	4.35
2	1296	7.8	1.77	4.41
2.5	1656	9.9	2.22	4.46
3	2088	12.3	2.76	4.46
3.5	2496	14.7	3.36	4.38
4	2832	16.8	3.84	4.38

Table B.1: Completely Eratron driven magnetic field with an additional resistance of  $0 \Omega$

Eratron Control Voltage	Total Current (Amps)	Mirror Field (kG)	Midplane Field (kG)	Mirror Ratio
0.5	300	1.8	0.31	5.81
1	648	3.8	0.67	5.67
1.5	960	5.8	1.04	5.58
2	1260	7.8	1.38	5.65
2.5	1680	10.0	1.78	5.62
3	2088	12.4	2.26	5.49
3.5	2448	14.8	2.68	5.52
4	2856	17.0	3.08	5.52

Table B.2: Completely Eratron driven magnetic field with an additional resistance of  $0.25 \Omega$

Eratron Control Voltage	Total Current (Amps)	Mirror Field (kG)	Midplane Field (kG)	Mirror Ratio
0.5	312	1.8	0.28	6.43
1	612	3.8	0.58	6.55
1.5	960	5.8	0.90	6.44
2	1296	7.8	1.20	6.50
2.5	1680	10	1.54	6.49
3	2064	12.5	1.94	6.44
3.5	2496	15	2.34	6.41
4	2832	17.2	2.68	6.42

Table B.3: Completely Eratron driven magnetic field with an additional resistance of  $0.5 \Omega$

Eratron Control Voltage	Total Current (Amps)	Mirror Field (kG)	Midplane Field (kG)	Mirror Ratio
0.5	300	1.8	0.24	7.50
1	624	3.8	0.52	7.38
1.5	960	5.8	0.81	7.16
2	1320	7.9	1.09	7.25
2.5	1680	10.2	1.36	7.5
3	2112	12.8	1.78	7.19
3.5	2496	15.0	2.08	7.21
4	2880	17.0	2.38	7.14

Table B.4: Completely Eratron driven magnetic field with an additional resistance of  $0.75 \Omega$

Eratron Control Voltage	Total Current (Amps)	Mirror Field (kG)	Midplane Field (kG)	Mirror Ratio
0.5	300	1.8	0.23	7.83
1	636	3.8	0.48	7.92
1.5	960	5.8	0.74	7.88
2	1320	7.9	0.98	8.03
2.5	1656	10.1	1.26	8.02
3	2064	12.6	1.58	7.97
3.5	2448	15.0	1.88	7.98
4	2832	17.2	2.16	7.96

Table B.5: Completely Eratron driven magnetic field with an additional resistance of  $1 \Omega$

### B.3.4 Representative Magnetic Field Plots and Discussion of limiting flux surfaces

The extent of the discharge within the MCX experimental vessel has primarily been estimated by examining the limiting flux surfaces of the magnetic field. Due to high electron mobility, in order to maintain an elevated electrostatic potential along a magnetic field line, that field line must terminate on an insulator. Thus the first and last good flux surfaces are defined as those immediately adjacent to the first and last field lines to terminate upon conductive surfaces. The inner first good flux surface is the one immediately flanking the last flux surface to contact the core at the mirror throat. The last good flux surface is the magnetic field line immediately inboard of the one which contacts the stainless steel vessel at any point. Note that

due to the irregularities in radial extent of the experimental vessel the location of this point is dependant upon the mirror ratio.

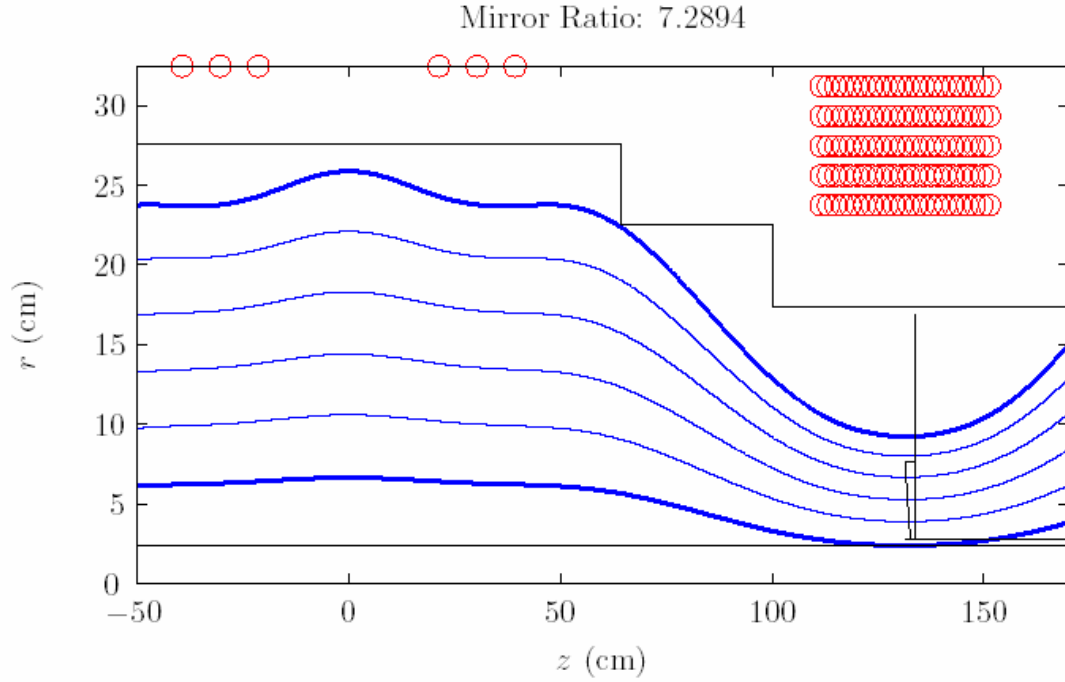


Figure B.3: The emboldened lines represent the innermost and outermost flux surfaces which do not terminate on a conductive vessel component. These magnetic field lines represent the expected axial limits to the rotational discharge.

The primary assumption made in concluding that these field lines are limiting surfaces is the supposition that the ratio of plasma pressure to magnetic field pressure, commonly referred to as  $\beta$  ( $\beta = \sum nk_B T / 2B^2 \mu_0$ ), is small. This small  $\beta$  limit means that the presence of the plasma does little to distort the magnetic field lines and as such the flux surfaces calculated ‘in vacuo’ should be similar to the flux surfaces present during active discharge.

## B.4 Chamber fill gas and pressure

While not in an active state, the chamber is maintained at a vacuum pressure of roughly  $4 \times 10^{-7}$  Torr, this minimizes the impurities present in the system. In order to be able to achieve a reliable plasma breakdown the vessel must be backfilled with molecular hydrogen to a dynamic pressure of between  $50 \mu\text{Torr}$  and  $50 \text{mTorr}$  depending upon the requirements of the shot. The term dynamic refers to our practice of continually pumping on the volume, even during a discharge event. First order approximations suggest that this does not affect the discharge as the volume can be treated as quasi-static for the duration of the discharge. The fill pressure is maintained at the requisite level by means of a precision micrometer leak valve.

A second leak valve has recently been installed and is attached to a secondary gas which is utilized as a plasma dopant for spectroscopic purposes. Preliminary tests with nitrogen indicate that an increased level of dopant will result in a stronger impurity signal and that the effect upon the plasma behavior remains perturbative as long as the dopant level does not exceed 10% by volume.

## Appendix C

Alternate calculation of the modified crowbar correction factor

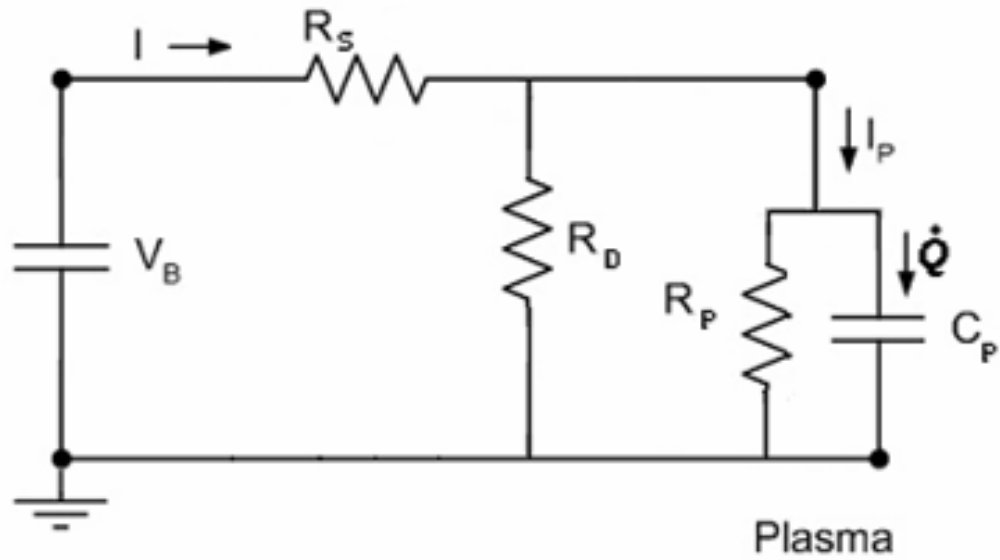


Figure C.1: Simplified diagram of the MCX discharge circuit.

Given the circuit diagram represented in Fig. B.1, the voltage on the plasma capacitor can be represented in any number of ways

$$V_P = \frac{Q}{C_P} = (I_P - \dot{Q})R_P = (I - I_P)R_D = V_B - IR_S \quad (\text{C.1})$$

Which leads us to the relations

$$I_P = \dot{Q} + \frac{Q}{R_P C_P} \quad (\text{C.2})$$

$$I = \frac{V_B}{R_S} - \frac{Q}{R_S C_P} = I_P + \frac{Q}{R_D C_P} \quad (\text{C.3})$$

Combining these arrive at an equation for  $Q(t)$

$$\dot{Q} + \frac{Q}{C_P} \left( \frac{1}{R_S} + \frac{1}{R_P} + \frac{1}{R_D} \right) = \frac{V_B}{R_S} \quad (\text{C.4})$$

Which is recognizable as

$$Q = (Q_0 - Q_1)e^{-t/\tau} + Q_1 \quad (\text{C.5})$$

Where  $\tau = C_P * (1/R_S + 1/R_P + 1/R_D)^{-1}$  and  $Q_0$  and  $Q_1$  are the pre and post charges present on the plasma capacitor after the modified crowbar is fired.

$$Q_0 = C_P V_P = C_P V_B \frac{R_P}{R_P + R_S} \quad (\text{C.6})$$

$$Q_1 = C_P V_B \frac{R_P R_D}{R_S R_P + R_P R_D + R_S R_D} \quad (\text{C.7})$$

So the difference in plasma current between our functional  $Q$  and the terminal state is

$$I_P - I_{P_1} = -\frac{Q - Q_1}{C_P \frac{R_D R_S}{R_D + R_S}} \quad (\text{C.8})$$

If we integrate this, we arrive at the charge present in the current reversal

$$\int_0^\infty I_P - I_{P_1} dt = -\frac{R_D + R_S}{C_P R_D R_S} (Q_0 - Q_1) \int_0^\infty e^{-t/\tau} dt \quad (\text{C.9})$$

$$Q_R = (Q_0 - Q_1) \frac{R_D + R_S}{R_D R_S} \frac{R_P R_D R_S}{R_S R_P + R_P R_D + R_S R_D} \quad (\text{C.10})$$

Noting that

$$Q_1 = Q_0 \frac{R_D(R_P + R_S)}{R_S R_P + R_P R_D + R_S R_D} \quad (\text{C.11})$$

This conglomeration can be simplified to

$$Q_R = Q_0 \frac{R_P^2 R_S^2 (1 + R_D/R_S)}{R_P^2 R_S^2 (1 + R_D/R_S + R_D/R_P)^2} \quad (\text{C.12})$$

Resetting the equation to determine the initial charge on the capacitor ( $Q_0$ ) as a function of the recorded reversal charge ( $Q_R$ ) we find

$$Q_0 = Q_R \left( 1 + \frac{R_D/R_P}{1 + R_D/R_S} \right) \left( 1 + R_D \left( \frac{1}{R_P} + \frac{1}{R_S} \right) \right) \quad (\text{C.13})$$

Which corresponds exactly with the correction factor derived in Chapter 3.

Special acknowledgement to Dr. Adil Hassam for motivating this derivation.

## Bibliography

- [1] G. F. Abdrashitov, A. V. Beloborodov, V. I. Volosov, V. V. Kubarev, Yu. S. Popov, and Yu. N. Yudin. Hot rotating plasma in the psp-2 experiment. *Nuclear Fusion*, 31(7):1275–1290, 1991.
- [2] K. B. Abramova, G. A. Galechayn, M. L. Lev, and A. V. Voronin. Rotating plasma in a closed magnetic trap. volume 1, pages 459–461, 1996.
- [3] H. Alfvén. Collision between a nonionized gas and a magnetized plasma. *Review of Modern Physics*, 32(4):710–713, Oct 1960.
- [4] Hannes Alfvén. *On the origin of the solar system*. Clarendon Press, Oxford, 1954.
- [5] Oscar Anderson, William R. Baker, Alexander Bratenahl, Harold P. Furth, and Wulf B. Kunkel. Hydromagnetic capacitor. *Journal of Applied Physics*, 30(2):188–196, 1959.
- [6] B. Angereth, L. Block, U. Fahleson, and K. Soop. Experiments with partly ionizing rotating plasmas. *Nuclear Fusion Supplement*, 1962.
- [7] D. A. Baker and J. E. Hammel. Rotating plasma experiments. ii. energy measurements and the velocity limiting effect. *Physics of Fluids*, 4(12):1549–1558, 1961.
- [8] D. A. Baker, J. E. Hammel, and F. L. Ribe. Rotating plasma experiments. i. hydromagnetic properties. *Physics of Fluids*, 4(12):1534–1548, 1961.
- [9] E. P. Barbian and C. E. Rasmussen. Rotating plasma and gravitational instability. *Plasma Physics*, 11:197–210, March 1969.
- [10] J. Bergstrom and T. Hellsten. Experiments on the velocity distribution of a rotating plasma. *Nuclear Instruments and Methods*, 133(2):347–353, 1976.
- [11] J. Bergström, S. Holmberg, and B. Lehnert. Free-wheeling of a rotating plasma. *Arkiv För Fysik*, 28(18), 1964.
- [12] J. Bergström, S. Holmberg, and B. Lehnert. Critical voltage of a rotating plasma. *Nuclear Fusion*, 6:231, 1966.
- [13] N. Brenning. Review of the civ phenomenon. *Space Science Reviews*, 59:209–314, February 1992.
- [14] N. Brenning and I. Axnäs. Critical ionization velocity interaction - some unsolved problems. *Astrophysics & Space Sciences*, 144:15–30, May 1988.

- [15] A. Case. Magnetic diagnostics on the maryland centrifugal experiment (mcx): Upgrades and initial results. *APS Meeting Abstracts*, pages 1064P–+, October 2005.
- [16] F. F. Chen. *Introduction to Plasma Physics and Controlled Fusion*. Plenum Press, New York, 1984.
- [17] R. Clary.  $H_\alpha$  emissions diagnostic for the maryland centrifugal experiment. *APS Meeting Abstracts*, pages 1061P–+, October 2005.
- [18] Ryan Clary. Absolute  $h_\alpha$  emission measurement system for the maryland centrifugal experiment. Master’s thesis, University of Maryland, College Park, 2006.
- [19] Alan DeSilva. *Plasma Diagnostics, Course Lecture Notes*. University of Maryland, College Park, 1996.
- [20] R. F. Ellis, A. Case, R. Elton, J. Ghosh, H. Griem, A. Hassam, R. Lunsford, S. Messer, and C. Teodorescu. Steady supersonically rotating plasmas in the maryland centrifugal experiment. *Physics of Plasmas*, 12(5):055704, 2005.
- [21] R. F. Ellis, A. B. Hassam, S. Messer, and B. R. Osborn. An experiment to test centrifugal confinement for fusion. *Physics of Plasmas*, 8(5):2057–2065, 2001.
- [22] H. K. Forsen and A. W. Trivelpiece. Rotating plasma as a source for injection into a magnetic mirror. *Physics of Fluids*, 9(5):1022–1031, 1966.
- [23] J. P. Freidberg. *Ideal Magnetohydrodynamics*. Plenum Press, New York, 1987.
- [24] J. Ghosh, R. Elton, H. Griem, C. Teodorescu, A. Case, and R. Ellis. Vacuum ultraviolet measurements on hydrogen resonance lines in the maryland centrifugal experiment. *Physics of Plasmas*, 12(3):034501, 2005.
- [25] J. Ghosh, R. C. Elton, H. R. Griem, A. Case, A. W. DeSilva, R. F. Ellis, A. Hassam, R. Lunsford, and C. Teodorescu. Radially resolved measurements of plasma rotation and flow-velocity shear in the maryland centrifugal experiment. *Physics of Plasmas*, 13(2):022503, 2006.
- [26] J. Ghosh, R. C. Elton, H. R. Griem, A. Case, R. Ellis, A. B. Hassam, S. Messer, and C. Teodorescu. Spectroscopic measurements of plasma rotation and ion and neutral atom temperatures in the maryland centrifugal experiment. *Physics of Plasmas*, 11(8):3813–3818, 2004.
- [27] R. J. Goldston and P. H. Rutherford. *Introduction to Plasma Physics*. Institute of Physics Publishing, Bristol, UK, 1995.
- [28] A. B. Hassam. Nonlinear stabilization of the rayleigh-taylor instability by external velocity shear. *Physics of Fluids B: Plasma Physics*, 4(3):485–487, 1992.

- [29] A. B. Hassam. Steady-state centrifugally confined plasmas for fusion. *Comments in Plasma Physics & Controlled Fusion*, 18(263), 1997.
- [30] A. B. Hassam. Stability of magnetohydrodynamic dean flow as applied to centrifugally confined plasmas. *Physics of Plasmas*, 6(10):3738–3743, 1999.
- [31] G. Himmel and A. Piel. The velocity limitation in a rotating plasma device of the homopolar type. *Journal of Physics D: Applied Physics*, 6(12):L108–L111, 1973.
- [32] Yi-Min Huang. *Magnetohydrodynamic Equilibrium and Stability of Centrifugally Confined Plasma*. PhD thesis, University of Maryland College Park, 2004.
- [33] Yi-Min Huang and A. B. Hassam. Velocity shear stabilization of centrifugally confined plasma. *Physical Review Letters*, 87(23):235002, December 2001.
- [34] Yi-Min Huang and A. B. Hassam. Magnetohydrodynamic stability of centrifugally confined plasmas. *Physics of Plasmas*, 11(5):2459–2465, May 2004.
- [35] Fu-Kwun Hwand. *Measurement of magnetic properties of confined compact toroid plasmas (spheromak)*. PhD thesis, University of Maryland, College Park, College Park, May 1991.
- [36] W. Knauer. Mechanism of the penning discharge at low pressures. *Journal of Applied Physics*, 33(6):2093–2099, 1962.
- [37] M. D. Kruskal and R. M. Kulsrud. Equilibrium of a magnetically confined plasma in a toroid. *Physics of Fluids*, 1(4):265–274, 1958.
- [38] B. Lehnert. Space-charge effects by nonthermal ions in a magnetized plasma. *Physics of Fluids*, 10(10):2216–2225, 1967.
- [39] B. Lehnert. Screening of a high-density plasma from neutral gas penetration. *Nuclear Fusion*, 8(173), 1968.
- [40] B. Lehnert. Rotating plasmas. *Nuclear Fusion*, 11:485–533, 1971.
- [41] B. Lehnert, J. Bergström, M. Bureš, S. Holmberg, and E. Tennfors. The minimum-power effect of a magnetized plasma. *Physica Scripta*, 9:109–118, 1974.
- [42] Shou-Zhe Li and Han S. Uhm. Influence of magnetic field on the electrical breakdown characteristics in cylindrical diode. *Physics of Plasmas*, 11(7):3443–3448, 2004.
- [43] S. Messer, R. Ellis, A. Case, D. Gupta, A. Hassam, R. Lunsford, and C. Teodorescu. Observation of momentum confinement time scalings in a rotating plasma. *Physics of Plasmas*, 12(6):062509, 2005.

- [44] Sarah Messer. *Supersonic Rotation in the Maryland Centrifugal Experiment*. PhD thesis, University of Maryland College Park, 2003.
- [45] C. E. Rasmussen, E. P. Barbian, and J. Kistemaker. Ionization and current growth in an  $e \times b$ . *Plasma Physics*, 11(3):183–196, 1969.
- [46] Arthur R. Sherwood and Wulf B. Kunkel. Formative time for breakdown in strong crossed fields. *Journal of Applied Physics*, 39(5):2343–2348, 1968.
- [47] C. Teodorescu, R. F. Ellis, A. Case, R. Clary, A. B. Hassam, R. Lunsford, and S. Messer. New high rotation mode in magnetized rotating plasmas. *Plasma Physics and Controlled Fusion*, 48:945–954, July 2006.
- [48] C. Teodorescu, R. F. Ellis, A. Case, C. Cothran, A. Hassam, R. Lunsford, and S. Messer. Experimental verification of the dielectric constant of a magnetized rotating plasma. *Physics of Plasmas*, 12(6):062106, 2005.